ELECTRON MICROSCOPY OF TITANIUM OXYNITRIDE SUPPORTED IRIDIUM BASED ELECTROCATALYSTS

Gorazd Koderman Podboršek

Doctoral Dissertation
Jožef Stefan International Postgraduate School
Ljubljana, Slovenia

Supervisor: Prof. Dr. Goran Dražić, National Institute of Chemistry and Jožef Stefan International Postgraduate School, Ljubljana, Slovenia

Evaluation Board:
Asst. Prof. Dr. Andreja Benčan Golob, Chair, Jožef Stefan Institute and Jožef Stefan International Postgraduate School, Ljubljana, Slovenia
Asst. Prof. Dr. Nejc Hodnik, Member, National Institute of Chemistry and Jožef Stefan International Postgraduate School, Ljubljana, Slovenia
Prof. Dr. Gaetano Granozzi, Member, University of Padova, Padova, Italy

MEDNARODNA PODIPLOMSKA ŠOLA JOŽEFA STEFANA
JOŽEF STEFAN INTERNATIONAL POSTGRADUATE SCHOOL

Gorazd Koderman Podboršek

ELECTRON MICROSCOPY OF TITANIUM OXYNITRIDE SUPPORTED IRIDIUM BASED ELECTROCATALYSTS

Doctoral Dissertation

ELEKTRONSKA MIKROSKOPIJA IRIDIJEVIH ELEKTROKATALIZATORJEV S PODLAGO IZ TITANOVEGA OKSINITRIDA

Doktorska disertacija

Supervisor: Prof. Dr. Goran Dražić

Ljubljana, Slovenia, October 2022

Acknowledgments

I would like to thank my mentor Prof. Dr. Goran Dražić for the opportunity to do my PhD, for the training in electron microscopy, and general guidance, Dr. Marjan Bele for general guidance, Prof. Dr Miran Gaberšček and Assoc. Prof. Dr. Nejc Hodnik for department management, and the whole Department of Materials Chemistry at the National Institute of Chemistry for a good working environment.

For their contributions as part of research teams working on mutual projects, I would like to specifically thank (in alphabetical order of last names):

- Dr. Marjan Bele (Department of Materials Chemistry, National Institute of Chemistry, Hajdrihova 19, SI-1000 Ljubljana, Slovenia) for the synthesis of TEM grid and CTiON-NCNF fabric samples, electrical conductivity measurements of CTiON-NCNF fabric samples, STEM EDXS analysis of TiON nanopowder and CTiON-NCNF fabric samples, SEM imaging of CTiON-NCNF fabric samples,

- Špela Božič (Department of Inorganic Chemistry and Technology, National Institute of Chemistry, Hajdrihova 19, SI-1000 Ljubljana, Slovenia) for CHNS measurements of TiON nanopowder and CTiON-NCNF fabric samples,

- Jena Cilenšek (Electronic Ceramics Department, Jožef Stefan Institute, Jamova 39, SI-1000 Ljubljana, Slovenia) for TGA measurements of TiON nanopowder and CTiON-NCNF fabric samples,

- Prof. Dr. Goran Dražić (Department of Materials Chemistry, National Institute of Chemistry, Hajdrihova 19, SI-1000 Ljubljana, Slovenia; Jožef Stefan International Postgraduate School, Jamova 39, SI-1000 Ljubljana, Slovenia) for the preparation of CTiON-NCNF samples with FIB-SEM and SEM imaging,

- Lea Gašparič and Prof. Dr. Anton Kokalj (Department of Physical and Organic Chemistry, Jožef Stefan Institute, Jamova 39, SI-1000 Ljubljana, Slovenia; Jožef Stefan International Postgraduate School, Jamova 39, SI-1000 Ljubljana, Slovenia) for simulations and simulation interpretation,

- Assoc. Prof. Dr. Boštjan Genorio (Department of Chemical Engineering and Technical Safety, Faculty of Chemistry and Chemical Technology, University of Ljubljana, Večna pot 113, SI-1000 Ljubljana, Slovenia) for TGA measurements of TiON nanopowder samples,

- Armin Hrnjić (Department of Materials Chemistry, National Institute of Chemistry, Hajdrihova 19, SI-1000 Ljubljana, Slovenia; University of Nova Gorica, Vipavska 13, SI-5000 Nova Gorica, Slovenia) for electrochemical treatment and electrochemical measurements of TEM grid samples,

- Dr. Primož Jovanovič (Department of Materials Chemistry, National Institute of Chemistry, Hajdrihova 19, SI-1000 Ljubljana, Slovenia) for electrochemical treatment, electrochemical measurements, and result interpretation of TEM grid samples,

- Ana Rebeka Kamšek (Department of Materials Chemistry, National Institute of Chemistry, Hajdrihova 19, SI-1000 Ljubljana, Slovenia; Faculty of Chemistry and Chemical Technology, University of Ljubljana, Večna pot 113, SI-1000 Ljubljana, Ljubljana) for writing algorithms for nanoparticle segmentation and atomic column position determination, nanoparticle

segmentation, image analysis, and result interpretation of TEM grid samples with big Ir nanoparticles,

- Rok Kaufman (Faculty of Mathematics and Physics, University of Ljubljana, Jadranska 19, SI-1000 Ljubljana, Slovenia) for sample preparation, electrical conductivity measurements, and result interpretation of CTiON-NCNF fabric samples,

- Katja Konečnik, Janja Štucin, and Asst. Dr. Špela Zupančič (Department of Pharmaceutical Technology, Faculty of Pharmacy, University of Ljubljana, Aškerčeva 7, SI-1000 Ljubljana, Slovenia) for the synthesis of CTiON-NCNF fabric samples,

- Prof. Dr. Janez Kovač (Department of Surface Engineering and Optoelectronics, Jožef Stefan Institute, Jamova 39, SI-1000 Ljubljana, Slovenia) for XPS measurements and result interpretation of TiON nanopowder, TEM grid, and CTiON-NCNF fabric samples,

- Edi Kranjc (Department of Materials Chemistry, National Institute of Chemistry, Hajdrihova 19, SI-1000 Ljubljana, Slovenia) for XRD measurements of TiON nanopowder, NH_4Br, and CTiON-NCNF fabric samples,

- Anja Lončar (Department of Materials Chemistry, National Institute of Chemistry, Hajdrihova 19, SI-1000 Ljubljana, Slovenia; University of Nova Gorica, Vipavska 13, SI-5000 Nova Gorica, Slovenia) for electrochemical treatment, electrochemical measurements, and result interpretation of TEM grid samples,

- Aleš Marsel (Department of Materials Chemistry, National Institute of Chemistry, Hajdrihova 19, SI-1000 Ljubljana, Slovenia) for electrochemical measurements and result interpretation of CTiON-NCNF fabric samples,

- Dr. Andraž Pavlišič (Department of Catalysis and Chemical Reaction Engineering, National Institute of Chemistry, Hajdrihova 19, SI-1000 Ljubljana, Slovenia) for writing a custom-made programme for nanoparticle segmentation,

- Dr. Luka Suhadolnik (Department for Nanostructured Materials, Jožef Stefan Institute, Jamova 39, SI-1000 Ljubljana, Slovenia; Department of Chemical and Pharmaceutical Sciences, University of Trieste, via L. Giorgieri 1, 34127 Trieste, Italy) for the synthesis TEM grid samples,

- Dr. Angelja Kjara Surca (Department of Materials Chemistry, National Institute of Chemistry, Hajdrihova 19, SI-1000 Ljubljana, Slovenia) for Raman measurements and result interpretation of TiON nanopowder and CTiON-NCNF fabric samples.

I would like to thank the Slovenian Research Agency (ARRS) for funding my PhD within the young researcher funding scheme and additionally partially within the research programmes P1-0112, P1-0189, P2-0084, P2-0152, P2-0393, and P2-0421 and projects J2-3041, NC-0016, N2-0106, N2-0155 N2-0248, Z1-9165, and Z2-8161. L.S. acknowledges funding from the European Union's Horizon 2020 research and innovation programme under the Marie Skłodowska-Curie grant agreement No 101025516. P.J. acknowledges the financial support from the Slovenian Research Agency under the project Z1-9165. N.H. acknowledges funding from the European Research Council (ERC) under the European Union's Horizon 2020 research (Grant agreement ID: 852208). NATO Science for Peace and Security Programme under grant G5729; and European Research Council (ERC) Starting Grant 123STABLE (Grant agreement ID: 852208) are acknowledged for funding the study. A.R.K. would like to acknowledge the Janko Jamnik Doctoral Scholarship.

Abstract

We are speeding full throttle towards a climate catastrophe and we have only until 2030 to take action to avoid the most devastating and unimaginable consequences. The lack of political and corporate will to change the status quo of "business as usual" is causing mass protests and civil disobedience globally. The rich elite is relying on science to find a "technological miracle" which will enable continued ever-growing profits while making the global economy carbon neutral. The hydrogen economy could be part of the solution. Water electrolysers convert water to hydrogen with electricity and fuel cells convert hydrogen back to water producing electricity. Hydrogen can therefore be used as an energy vector instead of fossil fuels. The research field of the sluggish oxygen evolution reaction (OER) requires innovation in order for electrocatalytic water electrolysis to become economically viable. The cost, stability, and activity of the electrocatalyst need to be improved. One way to achieve this is to use stable and electrically conductive ceramic support for the nano-sized Ir electrocatalyst, such as titanium oxinitride (TiON).

One key parameter that governs the properties of TiON is the N/O ratio. By having ways of determining the N/O ratio, newly synthesized TiON material samples can be evaluated and compared to other similar samples. Different analytical methods, such as scanning transmission electron microscope (STEM) energy dispersive x-ray spectroscopy (EDXS), scanning electron microscope (SEM) EDXS, electron energy loss spectroscopy (EELS), x-ray photoelectron spectroscopy (XPS), and thermogravimetric analysis (TGA) with CHNS elemental analysis were evaluated for N/O ratio determination.

An experimental platform, called NanoLab, was developed to gain insight into the effects of catalyst composition and structure on its stability and activity. Novel concepts such as identical location (IL) transmission electron microscopy (TEM), anodic oxidation of TEM grids, and modified floating-electrode-based electrochemical analysis were combined to enable accelerated development of electrocatalysts. NanoLab facilitates the observation of the electrocatalyst's local surface, morphology, composition, and structure which can all be followed with atomic resolution and understood in depth after each step of the synthesis procedure and electrochemical treatment. NanoLab was used to investigate the stability of the TiON-Ir support – electrocatalyst system. Together with density functional theory calculations, it was shown that Ir nanoparticles and Ir single atoms stabilize the TiON support which reduces oxidation during OER. NanoLab was also used together with in-house developed algorithms to understand structural transformations in TiON-supported Ir nanoparticles. The processed atomic resolution images revealed many degradation processes where surface roughening was found to be the predominant one. The reduced oxidation tendency of TiON-supported Ir nanoparticles was also confirmed.

Additionally, carbon TiON nanocomposite nanofibres (CTiON-NCNFs), synthesized with electrospinning and subsequent nitridation, were measured for electrical conductivity as single nanofibres and as bulk fabric. The electrical conductivity was better than similar amorphous carbon nanofibres, which makes them good candidates to be a support material for electrocatalysts and wiring material for electrochemical applications in general. Additional analytical methods were used to determine the morphology, crystal structure, chemical composition and N/O ratio from which electrical conductivity could be estimated and compared with experimental results.

Povzetek

S polno paro drvimo proti podnebni katastrofi, časa imamo le še do 2030 za ukrepanje v izogib najbolj uničujočim in nepredstavljivim posledicam. Manjko politične in korporacijske volje spremeniti trenutno stanje "običajnega poslovanja" povzroča množične proteste in civilno nepokorščino po vsem svetu. Bogata elita se zanaša na znanost, da najde "tehnološki čudež", ki bo omogočil nadaljevanje nenehno naraščajočih dobičkov in hkrati zagotovil ogljično nevtralnost svetovne ekonomije. Vodikova ekonomija bi lahko bila del nabora rešitev. Vodni elektrolizerji pretvorijo vodo v vodik z elektriko in gorivne celice pretvorijo vodik v vodo, da nastane elektrika. Vodik se tako lahko uporablja kot nosilec energije namesto fosilnih goriv. Znanstveno področje počasne reakcije evolucije kisika (REK) potrebuje inovacije, zato da elektroliza vode na osnovi elektrokatalizatorjev postane ekonomsko uresničljiva. Cena, stabilnost in aktivnost elektrokatalizatorjev morajo biti izboljšane. To je možno doseči z uporabo stabilne in električno prevodne keramične podloge za Ir elektrokatalizatorje nano velikosti, npr. s titanovim oksinitridom (TiON).

Glavni parameter, ki določa lastnosti TiON, je razmerje N/O. Z metodami za določanje razmerja N/O, ki so na razpolago, se lahko na novo sintetizirane vzorce TiON materiala ovrednoti in primerja z drugimi podobnimi vzorci. Različne analitične metode, kot so vrstična presevna elektronska mikroskopija (VTEM) z energijsko disperzijsko rentgensko spektroskopijo (EDRS), vrstična elektronska mikroskopija (VEM) EDRS, spektroskopija izgube energije elektronov (SIEE), rentgenska fotoelektronska spektroskopija (RFS) in termogravimetrična analiza (TGA) s CHNS elementno analizo, so bile ovrednotene za določanje razmerja N/O.

Eksperimentalna platforma NanoLab je bila razvita za pridobivanje razumevanja učinkov sestave in strukture katalizatorjev na njihovo stabilnost in aktivnost. Uporaba izvirnih metod, kot so presevna elektronska mikroskopija (TEM) identične lokacije, anodna oksidacija TEM mrežic in elektrokemijska analiza na osnovi predelane ploveče elektrode, so bile združene za omogočanje pospešenega razvoja elektrokatalizatorjev. NanoLab olajša opazovanje lokalne površine, morfologije, sestave in strukture elektrokatalizatorja in omogoča sledenje z atomsko ločljivostjo in poglobljeno razumevanje v vsakem koraku sinteze in elektrokemijske obdelave. NanoLab je bil uporabljen za raziskovanje stabilnosti TiON-Ir podloga – elektrokatalizator sistema. Skupaj z izračuni teorije gostotnega funkcionala je bilo pokazano, da Ir nanodelci in Ir posamezni atomi stabilizirajo TiON podlogo, kar zmanjša oksidacijo med REK. NanoLab je bil uporabljen tudi skupaj z interno razvitimi algoritmi za razumevanje strukturne pretvorbe Ir nanodelcev na TiON podlogi. Obdelane slike z atomsko ločljivostjo so razkrile veliko degradacijskih procesov, naraščanje hrapavosti površine je bilo ugotovljeno kot prevladujoče. Zmanjšano nagnjenje k oksidaciji Ir nanodelcev na TiON podlogi je bilo tudi potrjeno.

Dodatno je bila posameznim ogljikovim TiON nanokompozitnim nanovlaknom in tkaninam, sintetiziranim z elektropredenjem in nitridacijo, izmerjena električna prevodnost. Električna prevodnost je bila boljša kot pri podobnih amorfnih ogljikovih vlaknih, kar jih naredi dobre kandidate za podlogo za elektrokatalizatorje. Dodatne analitske metode so bile uporabljene za določitev morfologije, kristalne strukture, kemijske sestave in razmerja N/O, iz katerih je bila lahko ocenjena električna prevodnost in primerjana z eksperimentalnimi rezultati.

Contents

List of Figures xv

List of Tables xvii

Abbreviations xix

1 Introduction 1
1.1 Water electrolysis ... 1
1.1.1 Electrocatalysts for PEMWE ... 3
1.2 Titanium dioxide ... 4
1.3 Titanium nitride ... 4
1.4 Titanium oxynitride ... 5
1.4.1 Structure ... 5
1.4.2 Use ... 8
1.4.3 Synthesis methods ... 8
1.5 Electron microscopy ... 11
1.5.1 Transmission electron microscopy ... 12
1.5.2 Scanning electron microscopy ... 13
1.5.3 Scanning transmission electron microscopy ... 14
1.5.4 Electron energy loss spectroscopy ... 14
1.5.5 Energy dispersive x-ray spectroscopy ... 15
1.5.6 Identical location electron microscopy ... 15
1.6 NanoLab concept – a method for analysis at the nanoscale ... 15
1.7 TiON nanofibres ... 16

2 Aims and Hypothesis 19

3 Materials and Methods 21
3.1 Synthesis of TiON nanopowders for N/O ratio determination ... 21
3.2 Synthesis of TiON nanotubular structures and TiON-Ir catalyst – support systems for identical location analyses ... 21
3.2.1 Synthesis of TiON nanotubular structures as a support for small Ir nanoparticles ... 21
3.2.2 Addition of small Ir nanoparticles ... 21
3.2.3 Synthesis of TiON nanotubular structures as a support for big Ir nanoparticles ... 22
3.2.4 Addition of big Ir nanoparticles ... 22
3.3 Synthesis of carbon TiON nanocomposite nanofibres for electrical conductivity measurements ... 22
3.4 Sample preparation of CTiON-NCNFs ... 22
3.4.1 Resistivity of single CTiON-NCNF1s ... 22
3.4.2 Bulk resistivity of nanofibre fabric ... 23
3.4.3 STEM, EELS and STEM EDXS analysis ... 23
3.5 Electrochemical characterization and degradation ... 23
3.5.1 TEM grids ... 23
3.5.2 Nanofibres ... 25
3.6 Scanning transmission electron microscopy, electron energy loss spectroscopy, and energy dispersive x-ray spectroscopy ... 25

3.7 Scanning electron microscopy and energy dispersive x-ray spectroscopy 25
3.8 X-ray photoelectron spectroscopy 25
3.9 Raman spectroscopy 26
3.9.1 Nanopowders 26
3.9.2 Nanofibres 26
3.10 X-ray diffraction 26
3.11 Thermogravimetric analysis 26
3.12 CHNS elemental analysis 26
3.13 Optical microscopy 26
3.14 Density functional theory simulations 26
3.15 Programs used 28
3.15.1 Image processing algorithms 28

4 Results and Discussion **29**
4.1 Determination of N/O ratio in TiON 29
4.2 IL-TEM of TiON and TiON-Ir 32
4.2.1 NanoLab concept 32
4.2.2 Single Ir atoms 38
4.2.3 Big Ir nanoparticles 43
4.3 Microstructure and electrical conductivity of CTiON-NCNFs 48
4.3.1 Micro- and Nanostructure of CTiON-NCNFs 48
4.3.2 Crystal structure and chemical composition of CTiON-NCNFs 50
4.3.3 Electrical Conductivity and Electrochemical Measurements 53
4.3.4 Estimation of electrical conductivity of TiON nanofibres 56

5 Conclusions **59**

Appendix A **61**
A.1 NanoLab ..... **Napaka! Zaznamek ni definiran.**
A.1.1 Optical Microscope Analysis 61
A.1.2 Additional SEM and TEM analysis of the TEM grid floating electrode and detailed analysis of Ir nanoparticles 62
A.1.3 XPS analysis 64
A.1.4 Table of elemental composition of samples 65
A.1.5 XRD analysis of white powder formed during reduction of Ir salts 66
A.1.6 IL-EELS mapping 67
A.2 Single Ir atoms 68
A.2.1 Estimation of TiO_2 layer thickness 69
A.2.2 Density functional theory simulations 71
A.3 Big Ir nanoparticles 71

Appendix B **75**
B.1 CHNS and TGA elemental analysis 76
B.2 Raman spectroscopy of CTiON-NCNF1s 77
B.3 Modelling of STEM EDXS spectra of TiON/C–CNF2s 78
B.4 N/O ratio determination with EELS 79

References **85**

Bibliography **95**
Publications Related to the Thesis 95
Journal Articles 95

Biography **97**

List of Figures

Figure 1.1: Scheme of an electrochemical cell....2
Figure 1.2: Scheme of a PEM electrochemical cell 3
Figure 1.3: Structure of rocksalt TiON....6
Figure 1.4: Structure of anosovite TiON....7
Figure 1.5: Graph of thickness vs cell voltage with different categories of TiO_2 films.... 10
Figure 1.6: Typical electrospinning set-up 11
Figure 1.7: Scheme of a TEM.... 13
Figure 1.8: Scheme of the electron-matter interaction volume in SEM 14
Figure 3.1: Schematic presentation of modified floating electrode setup 24
Figure 4.1: XRD spectra of TiON nanopowder samples calcined 29
Figure 4.2: Proposed oxidation mechanism of TiN/TiON nanoparticles.... 30
Figure 4.3: Graphs of N/O ratios 30
Figure 4.4: Raman spectra of TiON nanopowder samples.... 31
Figure 4.5: The three most important techniques in the NanoLab concept 32
Figure 4.6: Synthesis, electrochemical degradation, and characterization of the TEM grid TiON-Ir electrocatalyst sample 33
Figure 4.7: IL-SEM images at every characterization step 34
Figure 4.8: IL-HAADF-STEM images at every characterization step.... 35
Figure 4.9: Electrochemical characterization of TiON-Ir based TEM grid 37
Figure 4.10: IL-HAADF-STEM images of the TiON-Ir sample.... 38
Figure 4.11: Graphs of the N/O ratio vs. thickness 39
Figure 4.12: Graphs of the N/O ratio vs. thickness 40
Figure 4.13: IL-HAADF-STEM images.... 41
Figure 4.14: Snapshots of the Ir NPs on the TiON(111) surface of Ti-vac_O type 42
Figure 4.15: Graphs of (Ir induced N preference) as a function of Ir SA concentration 43
Figure 4.16: STEM-HAADF images of the TiON-Ir sample.... 43
Figure 4.17: Evaluation of different activation protocols 44
Figure 4.18: IL-STEM images of (a-c) a smaller (nanoparticle no. 2) and (d-f) a larger (nanoparticle no. 5) Ir nanoparticle 45
Figure 4.19: Images of the atomic columns with different numbers of nearest neighbours 46
Figure 4.20: Graphs of the share of columns.... 47
Figure 4.21: SEM images of CTiON-NCNF1 fabric 48
Figure 4.22: Size distribution charts of CTiON-NCNFs 49
Figure 4.23: Crossections and images of CTiON-NCNFs.... 49
Figure 4.24: SAED pattern and diffractogram of CTiON-NCNF1 50
Figure 4.25: STEM EDXS analysis of TiON nanofibres 51
Figure 4.26: EELS mapping of a CTiON-NCNF1.... 52
Figure 4.27: EELS mapping of a cross-section of a CTiON-NCNF1 53
Figure 4.28: SEM image of a single CTiON-NCNF1.... 54
Figure 4.29: An example of an I-V curve of single CTiON-NCNF1 55
Figure 4.30: Graphs of electrochemical characterization of CTiON-NCNF2 fabric 56

Figure A.1: Optical microscope images of the TEM grid.... 61
Figure A.2: SEM images of the TEM grid.... 62
Figure A.3: BF-STEM images of the TiON-Ir TEM grid 63
Figure A.4: SEM images of the TEM grid.... 63
Figure A.5: Graphs of distributions of the TiON-Ir sample.... 64
Figure A.6: XRD spectrum of NH_4Br by-product.... 66

Figure A.7: IL-EELS mapping images of TEM grid sample 67
Figure A.8: IL-EELS measurement locations for the TiON sample 68
Figure A.9: IL-EELS measurement locations for the TiON-Ir sample 68
Figure A.10: STEM-HAADF images of TiON-Ir sample 69
Figure A.11: Scheme of the change of the TiON support 69
Figure A.12: TiON bulk cubic unit cells 71
Figure A.13: Graph of particle size distribution of Ir nanoparticles 71
Figure A.14: IL-STEM images of Ir nanoparticles 72
Figure A.15: Images of the atomic columns 73
Figure B.1: SEM image of (a) CTiON-NCNF1s and (b) CTiON-NCNF2s 75
Figure B.2: STEM-HAADF image of TiON nanoparticles of CTiON-NCNF1 75
Figure B.3: Optical images of the CTiON-NCNF2 fabric sample 76
Figure B.4: SEM images of contacts between CTiON-NCNF2s 76
Figure B.5: SEM image of CTiON-NCNF2 fabric 76
Figure B.6: TGA graph of the CTiON-NCNF1 fabric 77
Figure B.7: Raman spectra of CTiON-NCNF1s 78
Figure B.8: A simulated STEM EDXS spectrum 78
Figure B.9: Representative EELS spectrum of a CTiON-NCNF1 79
Figure B.10: Representative EELS spectrum of a CTiON-NCNF1 80
Figure B.11: STEM-HAADF images of CTiON-NCNF1s 80
Figure B.12: EELS spectrum of the carbon matrix of the CTiON-NCNF1 80
Figure B.13: STEM–HAADF images of the two-phase nanocomposite CTiON-NCNF1 81
Figure B.14: STEM-HAADF image of a nanocomposite CTiON-NCNF1 81
Figure B.15: SEM image of CTiON-NCNF2s at high magnification 82
Figure B.16: SEM EDXS analysis of CTiON-NCNF1 and CTiON-NCNF2 fabric 82

List of Tables

Table 4.1: Analysis depths and analysis spot sizes of different analytical methods..... 31
Table 4.2: N/O ratio at every characterization step from EELS, EDXS, and XPS 35
Table 4.3: Composition of samples CTiON-NCNF1 and CTiON-NCNF2 51
Table 4.4: Table of dimensions and electrical properties of single CTiON-NCNF1s..... 54

Table A.1: Table showing changes in particle size, circularity, and nearest neighbour distance for the TiON-Ir sample64
Table A.2: XPS surface composition..... 65
Table A.3: Table of elemental composition of the sample 65
Table B.1: STEM EDXS quantification results..... 78
Table B.2: Table of widths and starting points of the signals and backgrounds..... 79

Abbreviations

AWE	. . . alkaline water electrolysis
BF	. . . bright field
CE	. . . counter electrode
CHNS	. . . carbon hydrogen nitrogen sulphur
CVD	. . . chemical vapour deposition
EDXS	. . . energy dispersive x-ray spectroscopy
EELS	. . . electron energy loss spectroscopy
HAADF	. . . high angle annular dark field
HRTEM	. . . high resolution transmission electron microscopy
IL	. . . identical location
MEA	. . . membrane electrode assembly
NP	. . . nanoparticle
OER	. . . oxygen evolution reaction
ORR	. . . oxygen reduction reaction
PEM	. . . proton exchange membrane
PEMFC	proton exchange membrane fuel cell
PEMWE	. . . proton exchange membrane water electrolysis/electrolyser
RE	. . . reference electrode
SA	. . . single atom
SAED	. . . selected area electron diffraction
SEM	. . . scanning electron microscope
SEM EDXS	. . . scanning electron microscope – energy dispersive x-ray spectroscopy
STEM	. . . scanning transmission electron microscope
STEM EDXS	. . . scanning transmission electron microscope – energy dispersive x-ray spectroscopy
TGA	. . . thermogravimetric analysis
TiON	. . . titanium oxynitride
WE	. . . working electrode
XPS	. . . x-ray photoelectron spectroscopy
XRD	. . . x-ray diffraction

Chapter 1

Introduction

We are currently facing a problem of unprecedented dimensions, the climate crisis. Scientists have been warning about the consequences of fossil fuel use for more than 100 years [1], [2]. The Intergovernmental Panel on Climate Change is predicting that we have only 8 years left to act to have a chance to avoid unforeseeable climate catastrophes on a global scale by the end of the century [3]. All the technologies to achieve this are already available but the lack of political and corporate will is forcing us to find a "technological miracle" that is going to enable us to continue business as usual – eternal economic growth and infinite profits on a finite planet. Hydrogen economy could be part of the solution. To promote this technology to a profitable level, electrocatalysts in water electrolysers (and fuel cells), especially for the oxygen evolution reaction (OER), need to have improved activity and stability and the cost needs to be reduced [4]. The amount of precious metals available on earth is limited, which is why its use in electrocatalysts needs to be minimized and efficiency maximized. The benchmark catalysts used for this purpose are composed of precious metal nanoparticles embedded in the carbon-based support for the hydrogen evolution reaction (HER) and precious metal oxides for the OER [4]. By putting the precious metal nanoparticles on a suitable support, the active surface area can be increased and the amount of precious metals can be reduced. Nanoparticles should be well attached to the support and the whole system should have reasonable electrical conductivity enabling electrochemical reactions. Another important parameter is long-term stability of the support. Carbon based supports are quite unstable at oxidizing potentials, it can be oxidized and disintegrate, resulting in a reduction of efficiency [4], [5]. One of the possibilities of alternative support is titanium oxynitride (TiON).

TiON is a general term for a group of compounds with the chemical formula TiO_xN_y. It includes a spectrum of compounds with different N/O ratios with hybrid properties of titanium dioxide and titanium nitride [6], [7]. It is popular in research due to its remarkable optical and electronic properties, mechanical behaviour and chemical stability. TiON can also be called a designer material because of its versatility and finely tuneable properties, which can be tuned by changing the N/O ratio. In that way, we can get a combination of properties of metallic oxides (photocatalytic activity, corrosion resistance, optical properties) and nitrides (colour, hardness, wear resistance, durability, high electrical conductivity) [6], [7]. TiON is relatively new regarding its use as a support for electrocatalysts, therefore the mechanisms in corrosion resistance are not yet well understood, nor are other properties like the effect of chemical composition on electrical properties and electrocatalyst attachment efficiency, which are all things that will be researched during this doctorate.

1.1 Water Electrolysis

Hydrogen is the most efficient energy carrier and can be obtained, among many production methods, by an eco-friendly and high purity way with water electrolysis. Renewable energy sources can be used for this method and oxygen is the only by-product without any carbon emissions. Today, only 4 % of hydrogen is being produced in this way globally, mostly because of economic reasons [4]. The equation for the electrochemical reaction of water electrolysis can be expressed in its simplest form as:

$$2H_2O \rightarrow 2H_2 + O_2 \quad (1.1)$$

In water electrolysis, water decomposes to hydrogen and oxygen when an electric current passes through it. The most basic setup needed for this electrochemical reaction to run are two electrodes (anode and cathode) and an electrolyte (Figure 1.1). The full reaction produces two moles of hydrogen and one mole of oxygen per mole of water. By choosing the right electrolytes and electrodes, unwanted side reactions can be avoided. A separating membrane in the electrolyte between the two electrodes, which is permeable to ions, ensures the separation of the formed hydrogen and oxygen gas so that an explosive mixture of these two gases can be avoided [8]. The process requires a lot of energy in the form of electricity (240 kJ/mol) and hydrogen evolution rate is low and is therefore not economically competitive. In order to reduce the energy consumption and increase the efficiency, research has been done to improve water electrolysis technologies and find low cost electrocatalysts. New water electrolysis technologies can be classified based on the electrolyte used, operating conditions, and ionic agents (OH^-, H^+, O^{2-}). Examples of different water electrolysis technologies are: Alkaline water electrolysis (AWE), solid oxide electrolysis, microbial electrolysis cells, and proton exchange membrane (PEM) water electrolysis (PEMWE) [4].

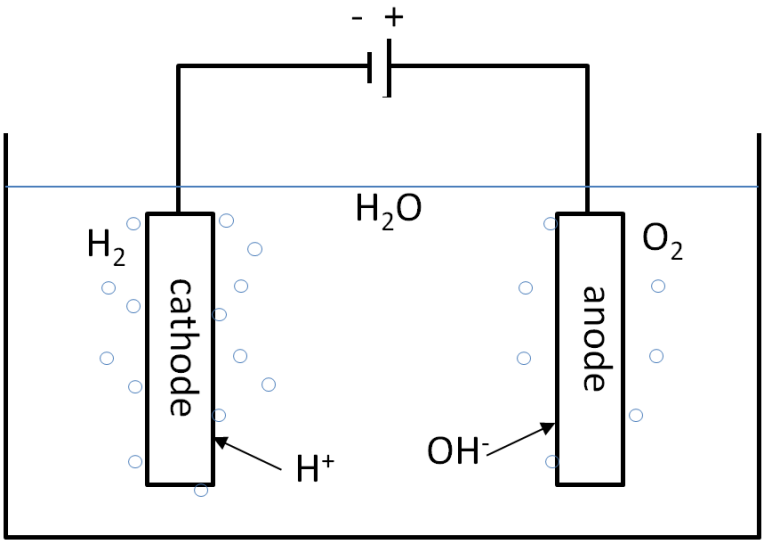

Figure 1.1: Scheme of an electrochemical cell.

The first PEMWE was developed in 1966 as an attempt to overcome the drawbacks of AWE. PEMWEs were built based on technologies from PEM fuel cells, where a solid polysulfonated membrane is used as an electrolyte (proton conductor) between the two electrodes (Figure 1.2). The PEM has many advantages such as lower gas permeability, lower thickness, high proton conductivity and high-pressure operability. Other advantages are compact design, high efficiency, high current density, small footprint, fast response, and operation at lower temperatures (20 °C – 80 °C). The state-of-the-art electrocatalysts for PEMWE are high activity noble metals such as Pt/Pd for the hydrogen evolution reaction (HER) and IrO_2/RuO_2 for the oxygen revolution reaction (OER). The high price of noble metals makes PEMWE more expensive than AWE. That is why the main focus of research is to reduce the production cost of PEMWEs. Additionally, OER is much slower than HER so more research is focused on increasing OER efficiency while reducing noble metal use and increasing stability [4].

In PEMWEs, water is split into protons, electrons, and oxygen gas on the anode:

$$H_2O_{(l)} \rightarrow 2H^+_{(aq)} + \frac{1}{2}O_{2\,(g)} + 2e^- \quad (1.2)$$

Then, the protons travel through the proton conducting membrane to the cathode. The electrons travel through an external power circuit. The electrons and protons combine at the cathode to form hydrogen gas [4]:

$$2H^{+}_{(aq)} + 2e^{-} \rightarrow H_{2\,(g)} \tag{1.3}$$

PEMWEs consist of membrane electrode assemblies (MEAs), gas diffusion layers (which are current collectors), and separator plates. MEAs are the most important part of PEMWEs. An MEA consists of a membrane, an ionomer solution, and an anode and cathode electrocatalyst layers. The membrane holds the MEA together, the most commonly used membranes are perfluorosulfonic acid polymer membranes, especially Nafion®. This type of membrane has high strength, efficiency, oxidative stability, and proton conductivity. They operate at high current densities and are also durable and dimensionally stable with temperature change. The other important part are the electrocatalyst layers (anode and cathode) which are usually mixed with the ionomer solution and directly coated on the membrane to form the MEA [4].

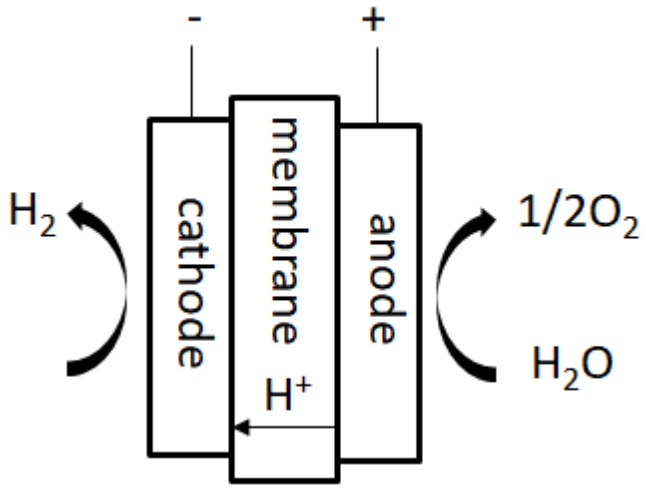

Figure 1.2: Scheme of a PEM electrochemical cell.

1.1.1 Electrocatalysts for PEMWE

Typically, electrocatalysts used in PEMWEs are made from noble metals which are expensive but very efficient. At the cathode for HER, Pt/Pd-based electrocatalysts are used and at the anode for OER, RuO_2/IrO_2-based catalysts are used. To reduce costs and improve efficiency and stability at the same time, research focus is moving towards noble metal non-noble metal alloys and noble metal non-noble metal mixed oxides or even fully non-noble metal compounds. To decrease the noble metal use even further, the electrocatalysts are being put on electrically conductive support materials to increase the electrocatalyst surface area with less electrocatalyst used while maintaining good electrical conductivity. Most popular support materials are carbon-based for HER and metallic oxides for OER but research focus is also going in the direction of alternatives to these supports [4].

1.1.1.1 Electrocatalysts for OER

IrO_2 is generally recognised as the state-of-the-art electrocatalyst for the OER in PEMWE. RuO_2 has a higher activity compared to IrO_2, but is more prone to corrosion which limits its use. In the past, research was focused on the use of Ru and Ir electrocatalysts and their alloys. The aim was to improve efficiency, stability and reduction of costs and some researchers began trying to find alternatives for the OER. One of the early ideas was to mix IrO_2 or RuO_2 with other cheaper oxides, which are more durable and can be easily manufactured, to form a solid solution. For this, many different types of oxides were used such as SnO_2, Ta_2O_5, Nb_2O_5, Sb_2O_5 and even mixtures of these oxides. One problem that arose from these types of coatings on metallic

electrodes (for example Ti) was low electron conductivity which could cause electrode passivation. Other modes of destruction of such mixed oxide coated electrodes are dissolution of the active component, penetration of the electrolyte through the mixed oxide layer, and dissolution and anodic oxidation of the metallic electrode base. Mixtures of three oxides (for example SnO_2–IrO_2–Ta_2O_5) showed superior properties compared to mixtures of two oxides. The presence of tantalum oxide (even at low molar fractions), for example, expanded the surface area, improved electronic conductivity, increased charge storage capacitance, and promoted surface enrichment of Ir. But due to metallic electrode base, such catalysts could not be used in MEAs due to the impermeability of the solid catalyst plate [9].

A good electrocatalyst for PEMWEs needs to have a high surface area which enhances performance and ionic conductivity. Electrocatalysts which are produced in a “free standing” form can also be more easily applied to the electrolyte membrane. Because of this, research was focused on ultrafine catalyst nanoparticles where membrane-electrode contact was enhanced [9]. An ideal catalyst layer then provides high catalyst utilization, high electron conductivity, durability, and high mass transport. Some synthesis methods are very suitable to produce ultrafine catalyst nanoparticles such as polyol method [10], solvothermal method [11], and the Adams fusion method [12]. The modified polyol method is believed to form a solid solution between IrO_2 and the other oxide (for example SnO_2) which improves electrical conductivity compared to other synthesis methods where separated oxide phases are formed. Non-noble oxides (such as TiO_2, SnO_2, Ta_2O_5, Nb_2O_5, Sb_2O_5) do not contribute actively to the OER, but can play important roles in other ways such as suppressed adsorption of hydroxyl species (in the case of SnO_2) which releases more active reaction sites of IrO_2 [9].

The non-noble oxides function as a diluent for the noble metal oxide and increase stability against corrosion. They work as a support material for the active electrocatalyst. Other compounds can be used for this purpose, such as carbides [9] and, due to their higher electrical conductivity, nitrides and oxynitrides.

1.2 Titanium Dioxide

TiO_2 is a well-known insulator and oxide semiconductor with many applications in important research areas such as solar energy harvesting and photocatalysis [6]. TiO_2 exists in three main crystalline forms, rutile, brookite and anatase, different phases manifest different properties. TiO_2 films have several potential applications in microelectronics, such as antireflection coatings, optical filters, integrated optical chemical sensors, and optical waveguides etc. due to their high transmittance in the high refractive index, visible spectral range, and their thermal and chemical stability. Other fields of potential use are photocatalysts for wastewater treatment and solar-energy conversion, storage capacitors in DRAMs, insulators in MOS devices, deep ultraviolet lithography, electrochromic displays, gas sensors, and other optical coatings [7], [13].

1.3 Titanium Nitride

TiN is an attractive material for various applications such as mechanics, optics, and microelectronics due to its superior properties. For example, TiN films are one of the most studied systems, finding widespread use in a number of applications due to their hardness, diffusion barrier properties (thermodynamically very stable), low electrical resistivity (high conductivity), high thermal and chemical stability, extreme wear resistance, and attractive colours. They are used in plasmonic applications, cutting tools, MEMS, solar reflectors, wear-resistance coating, anti-reflective coating, metallization for large-scale integrated circuits, as electrode materials and decorative coating (the colour of stoichiometric TiN films is similar to that of gold) etc. TiN coloured films are also attractive to consumers and are therefore used in ornament industries. These films can be prepared by various chemical and physical deposition techniques. TiN films are not only important for the colour but also for electrical properties at interfaces between two layers. Research on TiN films indicates that mechanical properties, electrical properties and colours of the TiN film mostly depend on oxygen content in the film and film thickness [6], [7], [14]–[17].

1.4 Titanium Oxynitride

The term TiON is used to describe a group of compounds of general composition TiON which are intermediate phases found midway between titanium dioxide (TiO_2) and titanium nitride (TiN). According to already published articles the term is not used to refer to a certain number of stable compounds with a fixed ratio of O and N but rather the whole continuum of possible ratios between O and N. The term is even used if there are more phases present in the system (for example a phase of cubic TiN doped with O and a separate crystal phase of anatase TiO_2). TiON has recently become a popular material to synthesize, research, and use because it is a hybrid between TiN and TiO_2, also its properties are somewhere between the properties of TiN and TiO_2 [6], [7], [18].

More and more high-tech materials are needed for new emerging advanced applications where the properties of the materials need to be versatile and finely tuneable. This is a problem that scientists need to face when working with pure nitrides or oxides (for example TiN or TiO_2). In the past, there was a considerable interest in the study of TiON materials, due to their remarkable optical and electronic properties, mechanical behaviour and chemical stability. TiON exhibits the combination of properties of metallic oxides (colour, optical properties) and nitrides (hardness, wear resistance). So far, TiON has been extensively investigated due to its physico-chemical properties, such as hardness, durability, corrosion resistance, photocatalytic activity, etc., which make this material suitable for a large variety of applications including thin film technology, optical coatings or photocatalytic applications in the visible range. Recently, interest in TiON has increased due to the pronounced dependence of their properties on the N/O ratio. The ratio of N and O in TiON can be tuned which is also changing the properties of TiON in a continuous manner. In terms of, for example, conductivity, this means a continuum from insulating properties of the ionic oxide TiO_2 to metallic properties of the pure covalent nitride compound TiN which is an even better electrical conductor than titanium. The final properties of TiON are related to the chemical composition and homogeneity, as well as the crystallographic structure [6], [7].

Jung et al. have done research on TiON thin films, which were deposited by a DC magnetron sputtering method, and the change of their properties as a function of oxygen flow rate. It was shown with x-ray photoelectron spectroscopy (XPS) and high resolution transmission electron microscopy (HRTEM) analysis that the chemical energy states and microstructures of TiON films are influenced by the amount of oxygen flow rate. As the oxygen content increased, the peak positions of titanium shifted. The major part of every sample was amorphous TiON and a small part was the TiN(111) crystal phase which was confirmed by both the HRTEM image and microdiffraction pattern. As a result, the fully crystallized TiN microstructure transformed to TiON with small amounts of the TiN crystal phase still present as the oxygen flow rate increased. Also, the microdiffraction pattern of TiON made it apparent that the lattice parameter increased compared with TiN film grown without oxygen flow. The structural distortion was probably caused by oxygen. It was thought that oxygen exists interstitially inside of the TiN lattice. This means that the electrical properties can be expected to vary with the amount of TiN crystal phase inside of TiON films. It has been shown that the resistivity of TiON thin films increased up to 10^{10} Ωcm as the oxygen flow rates increased [19].

1.4.1 Structure

There has not been much research devoted to the chemical composition and structural analysis of TiON. Investigations show that such compounds exhibit a quite complex structure as a function of the N/O ratio. As a result, efforts to determine and understand their structure have led to a wide range of interpretations, and this still remains an open question. In previous works, some structural and chemical characterizations were carried out on chemical vapour deposition (CVD) layers. Guillot et al. obtained samples of thin films with different N/O ratios by varying the growth temperature. These samples were quantified with Rutherford backscattering spectroscopy (RBS) and it was shown that the oxygen content decreases with growth deposition temperature. Using X-ray diffraction (XRD), an isomorphic structure of TiN and TiO (face-centred cubic structure, Figure 1.4) was determined to be present in the samples with peak positions located between the theoretical values of the two phases. It was shown that the lattice parameter increases as a function of the growth temperature. The lattice parameter increase

can be linked to the oxygen content and to substitution of nitrogen atoms by oxygen atoms which leads to a Ti(N,O) phase. The nitrogen atomic radius is bigger than that of oxygen, so an increase in oxygen content induces a decrease in the lattice parameter. This lattice parameter variation could also be attributed to the residual stress in the layer, but XRD measurements showed that the real residual stress contribution to the lattice parameter variation is negligible. That is why it is very probable that the lattice parameter change happens because of atom substitution. The oxygen quantities are too large to be explained only by the presence of the Ti(N,O) phase. The presence of another amorphous titanium oxide such as TiO_2 could explain the excess amount of oxygen [20]–[22].

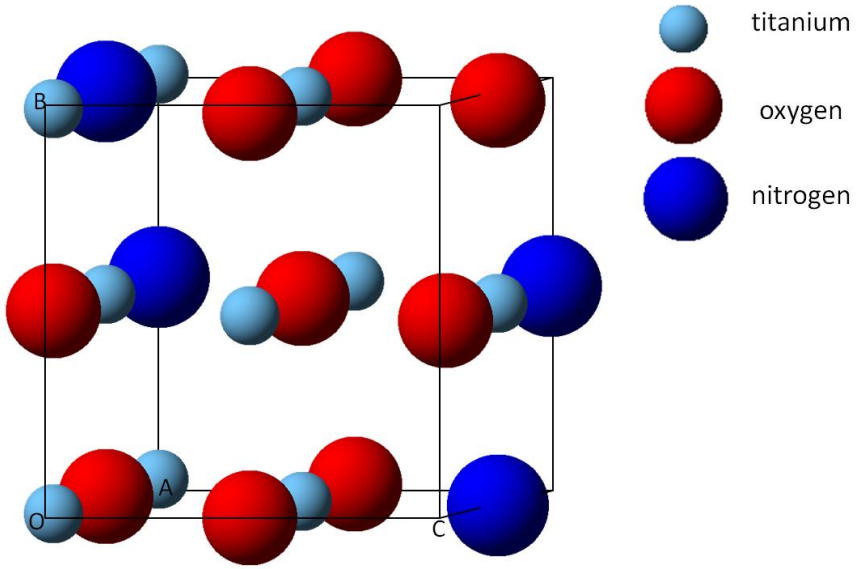

Figure 1.3: Structure of rocksalt TiON. Ti cations have occupancy 0.75 and N and O anions share the same locations with occupancy 0.5 (arbitrary TiON composition).

Research like the one above and similar investigations into TiON have uncovered titanium compounds with the face-centred cubic cell structure and empirical formula TiON (the sum of x and y is many times approximately 1, but can also vary widely) [23]. However, in most cases, the compound maintains the rock salt structure and compensates for the nonstoichiometry through vacancies on the titanium sites [23]. These TiON phases can be considered as a solid solution of cubic titanium(II) oxide, TiO and the cubic titanium(III) nitride, TiN, where the lattice parameter of a given TiON compound can be found by Vegard's Law somewhere between the value of 4.172 Å for TiO and 4.244 Å for TiN [23].

In contrast to the close-packed cubic TiON materials ($d \approx 5.8$ g/cm^3), Hyett et al. discovered TiON based on nitrogen substitution into the less dense ($d \approx 4.3$ g/cm^3) orthorhombic α-Ti_3O_5 structure (anosovite) (Figure 1.4). This oxynitride is isostructural to the high-temperature phase of Ti_3O_5, a preference for this *Cmcm* structure at room temperature is similar to that observed by cationic doping of Ti_3O_5. The structural analysis of $Ti_{2.85(2)}O_4N$ shows that the nitrogen present substitutes oxygen on the 4c crystallographic site. Before this study the only binary titanium oxides known to incorporate nitrogen to form oxynitrides were the rock-salt structured TiO, and in nitrogen-doped TiO_2 (only low levels of nitrogen). They synthesized it using combinatorial chemical vapour deposition with a triple source of precursors: $TiCl_4$ (metal source), NH_3 (nitrogen source), and ethyl acetate (oxygen source). The relative ratio of oxygen source to nitrogen source was varied between the samples to produce films of $Ti_{3-\delta}O_4N$ with differing compositions. The range of titanium ion vacancy was between 0.06 and 0.27. Synchrotron XRD, XPS and UV-vis spectroscopy were used to investigate the new compound. The material crystallizes in the space group *Cmcm*, where the ordered nitrogen ions stabilize the structure into an orthorhombic analogue of the monoclinic anosovite, Ti_3O_5. The lattice parameters were determined to be a=3.8040(1) Å, b=9.6486(6) Å, and c=9.8688(5) Å for $Ti_{2.85(2)}O_4N$ and they

change depending on composition. TiON structures have been investigated in detail by conventional techniques for many years and no indication of this or any other complex (nonrock salt-type) structure was found [23].

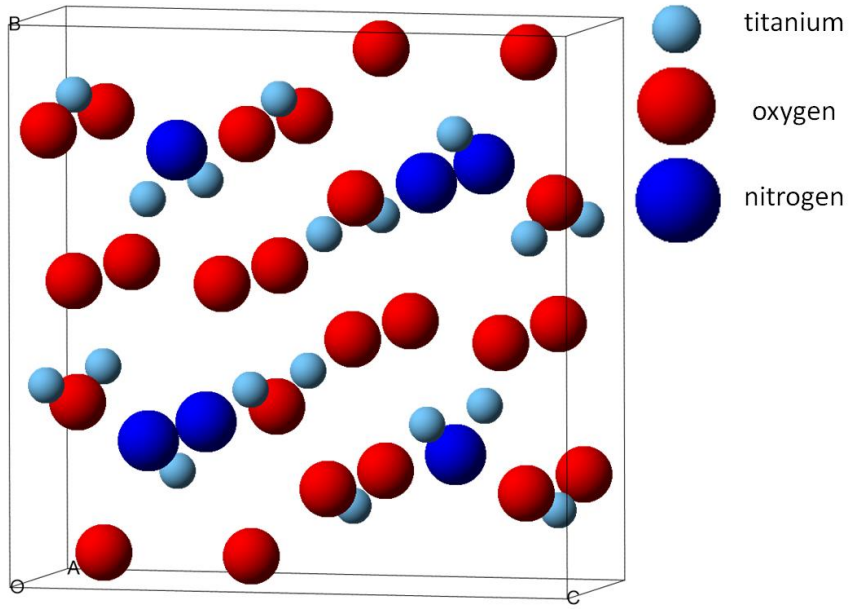

Figure 1.4: Structure of anosovite TiON.

Another type of TiON has been extensively reported: the doping of TiO_2 with nitrogen. Research on these materials has been conducted principally to change the band gap of TiO_2 and alter its hydrophilic and photocatalytic properties. The extent of doping in these materials is extremely small, typically less than 0.5 at. % of nitrogen, and is by some considered as nitrogen-doped materials rather than as true TiON [23]. In the past, TiO_2 has been the subject of many studies because of its potential applications in important research fields such as photocatalysis, photovoltaic and UV protection. TiO_2 is chemically stable, absorbs strongly in the ultraviolet region, and is highly photocatalytically active which causes quick degradation of harmful organic compounds. TiO_2 performance still needs to be improved in order to be used in these applications. To achieve this, the performance of TiO_2 could be improved by reducing its band gap which would shift its absorption in the visible region and, consequently, more solar energy could be absorbed. By doping TiO_2 with different elements such as carbon, nitrogen, or sulphur, the bang gap can be reduced. Another way to achieve a band gap reduction would be to synthesize sub-stoichiometric crystalline phases of TiO_2. The TiO_2 electronic structure is now well researched but the structure and optical properties of sub-stoichiometric species still need to be better understood [24].

Simon et al. synthesized a nitrogen containing sub oxide TiO_2 phase which had a crystallographic FCC structure as identified by XRD [24]. The presence of nitrogen in the structure was proven with XPS. The XRD showed that the main crystalline phase was FCC TiO and XPS at the Ti core level showed 3 components attributed to Ti^{2+}, Ti^{3+}, and Ti^{4+}. The presence of Ti^{2+} state corresponds to TiO from XRD. The percentage of the other components was calculated to be bigger than that of the Ti^{2+} state, which indicated that the true Ti oxidation state and the accurate structure of this compound are more complex than previously thought. Also the previous study of the same group on this oxide phase showed that optical properties can be tuned with thermal treatment in air. As they increased the annealing temperature, the absorption threshold value shifted gradually toward higher energies. This showed that an entire family of TiON products with an adjustable gap can be produced [24]. Because XPS and XRD measurements were not enough to fully characterize the Ti(O,N) system, they also used electron energy loss spectroscopy (EELS) and x-ray absorption spectroscopy techniques to propose a detailed description of the complex structure and chemistry of these nanoparticles. The elemental map obtained from the EELS measurements has shown that there is a homogeneous

solid solution of TiO and TiN in the nanoparticles. These two species are the cause of Ti^{2+} and Ti^{3+} signals in XPS. When annealing (thermal treatment in air), oxidation occurs on the nanoparticles surface, which leads to an increased Ti^{4+} signal in XPS. In these TiON nanoparticles, the x-ray absorption near-edge structure signal shows that Ti^{3+} states are coming from the Ti(O,N) solid solution which may be non-stoichiometric, and from the disorder in the particles, of the disordered TiO_2 phase. The system has a high oxidation degree compared to what would be expected for TiO or for TiN. This is because of defect states resulting from non-stoichiometry of the Ti(O,N) solid solution, nitrogen in the lattice, and titanium atoms in a disordered TiO_2 phase. The extended x-ray absorption fine structure signal confirmed the FCC structure of a solid solution of TiO and TiN with titanium vacancies with a long range order and another short range disordered anatase phase [24], [25].

1.4.2 Use

The majority of applications for TiON at present are in the form of TiON thin films. TiON thin films attract much attention owing to their remarkable optical and electronic properties, which depend significantly on the N/O ratio. Nitrogen-rich TiON has been widely used in many applications, such as anti-reflective coating, decorative coatings, biomaterials, excellent diffusion barriers and resistors, while oxygen-rich TiON has been applied in thin film resistors and as insulating layers in metal–insulator–metal capacitive structures in order to avoid oxide interface layer formation. Many other useful applications of TiON films, such as solar selective absorbers (visible light), transparent IR window electrodes, water splitting systems, photoelectrochemical catalysts, oxygen reduction reaction (ORR) catalysts and wear-resistant coatings have been demonstrated [14], [26]–[28]. Nitrogen-rich TiON shares interesting properties with TiN, which make it attractive for various domains of applications like optics, micro-electronics and mechanics with the advantage of being more corrosion-resistant and chemically stable than TiN. Particularly, the N/O-ratio-dependent properties of TiON make it the focus of many recent studies in biomaterials, solar panels, protective and decorative coating and thin film resistors [17].

TiON films are also important for their properties at the interface between two layers. These TiON films provide a retarding diffusion barrier between a metal and silicon. The TiON film blocks the fast diffusion path of oxygen. By controlling the amount of oxygen inside the TiON film, different requirements from different industries can be fulfilled [15]. TiON can also be used in the form of nanoparticles. TiON nanoparticles are particularly stable because they are insoluble in acidic media, as confirmed by leaching tests conducted using inductively coupled plasma atomic emission spectroscopy. The presence of N atoms in these nanoparticles is necessary for maximizing the ORR activity of TiON catalysts of various particle sizes (∼20 nm – 200 nm) [29]. Furthermore, TiON was proposed for the use as a novel electrode material because of its high thermal and chemical stability and high electrical conductivity [16].

1.4.3 Synthesis methods

Various different synthesis methods have been developed in order to synthesize TiON with a wide range of oxygen and nitrogen concentrations. Among these processes, some physical and chemical vacuum deposition methods have been shown to be feasible ways to achieve tuneable chemical compositions and a variety of physicochemical properties. The different possible synthesis techniques are: reactive (pulsed) magnetron sputtering, radio-frequency pulsed laser deposition, arc ion plating method, electron cyclotron resonance, reactive gas pulsing technique, ion (beam) assisted deposition, dual ion beam sputtering, hollow cathode ionic plating, hollow cathode reactive direct current sputtering system, CVD, electron beam evaporation, plasma vapour deposition, physical vapour deposition, the solvothermal method, the hydrothermal method, direct thermal nitridation of TiO_2 or TiO in ammonia gas at elevated temperatures, oxidizing TiN, and the sol-gel method. Sol-gel method, among other methods, is more widespread and convenient to produce transition metal oxynitrides [7], [17], [20], [26], [30].

TiON can be synthesized in many ways as can be seen above and some of them are based on TiN or TiO_2 as a starting material. Preparation of TiON through nitridation of TiO_2 or oxidation of TiN is not straightforward. On the one hand, nitrogen implantation in TiO_2 leads to noticeable reconstruction of the surface due to strong reduction and only a small amount (2 % − 3 %) of

implanted nitrogen can be reached, and on the other hand, the oxidation of the TiN quickly leads to the formation of TiO_2 [6]. In the case of oxidizing TiN at low temperatures (250 K), molecular oxygen adsorbs chemically on the surface which enables O atoms to bind to Ti surface atoms. The oxidation does not make progress into the bulk and it is probably limited to the first layer. When the temperature is 450 K, the adsorption/dissociation of molecular oxygen on the surface is exothermic, but the necessary N–O surface exchange is a very endothermic step that can only happen at high temperatures. Further N–O substitution involving inner TiN layers is always endothermic as long as the cubic structure is preserved. A hypothetical rocksalt structure for TiON is highly unlikely and oxidation of TiN probably involves a loss of the initial structure at the same time. Oxidation at 450 K involves formation of both N_2 and NO at the beginning of the reaction. The formation of N_2 decreases with time. Instead of N_2, a signal of NO starts to form which indicates that the main channel of the reaction is $TiN+mO_2 \rightarrow TiN_{1-x}O_x+NO$. Both N recombination and NO formation processes are exothermic, the former may only take place at very low oxygen coverage [31]. In the case of nitridizing TiO_2, the band gap does not get narrower, instead, N doping induces localized N 2p states inside of the band gap just above the valence band. N is present as N(III), which enables the formation of oxygen vacancies at higher temperatures. The increased amount of O vacancies causes a reconstruction of the rutile (110) surface. This thermal instability may degrade the surface structure of the material during applications, which can seriously affect its properties [32].

1.4.3.1 Anodic oxidation

Titanium metal can be anodically oxidized to form nanostructured oxide layers on titanium. Different procedures and parameters used allow changes in the characteristics of the oxide layer such as morphology, structure, composition, and thickness. With anodic oxidation, the surface-related properties of titanium and its alloys can be fine-tuned which widens the application possibilities. Anodic oxidation is generally applied to valve metals (for example Al, Hf, Nb, Ta, Ti, W, Zr), which are metals that form oxides with ionic conduction and almost perfect electrical insulation. Anodic oxidation of titanium is still an actively researched scientific field and new morphologies, functionalities and compositions are being found [33].

Titanium gets naturally passivated with a few nanometres thick film which can be increased up to hundreds of micrometres with oxidation methods. Nowadays, the anodizing process can be controlled very well which enables the development of engineered oxidized titanium surfaces. By imposing a current flow between titanium and a counterelectrode in a solution, titanium gets polarized and oxidized to Ti^{4+} ions. Combined with oxygen ions, an oxide layer is formed on the metal surface. The oxide film can grow from both ends but growth from the metal surface is predominant due to easier transport of oxygen ions compared to titanium ions [33].

The formed oxide layers can be divided into three categories based on their properties and synthesis conditions (Figure 1.5):

- Thin compact films which show interference colours
- Nanotubular films
- Films form high voltage anodization

For nanotubular films to form, the electrolyte usually contains fluoride ions. High voltage anodization can be called plasma electrolytic oxidation or micro-arc oxidation or anodic spark deposition [33].

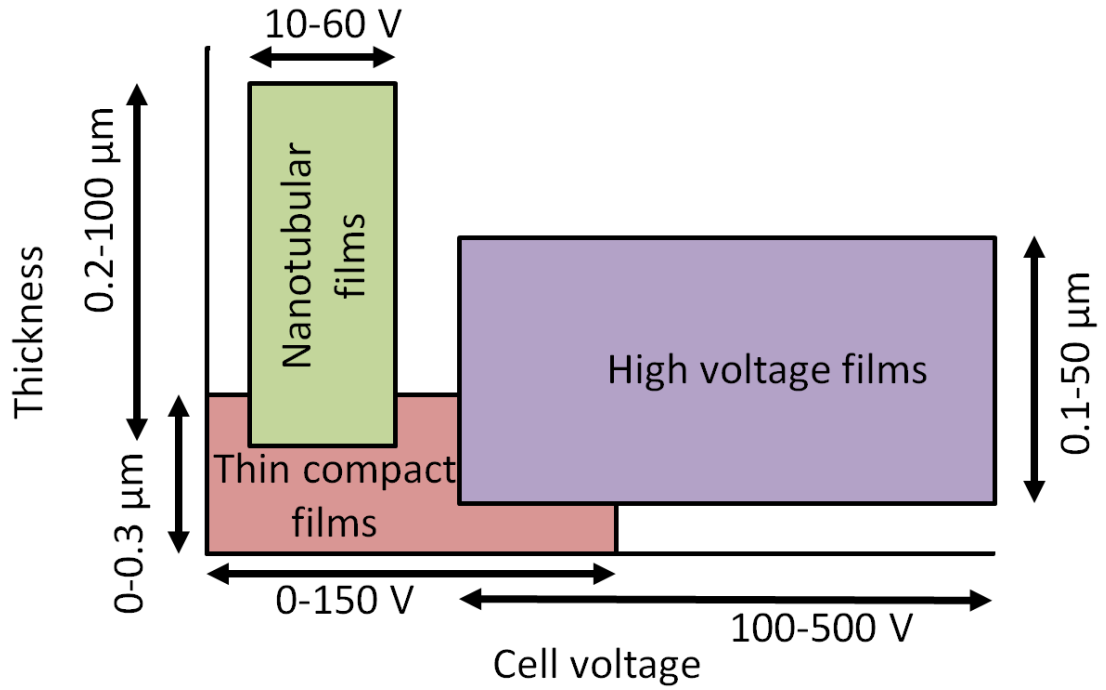

Figure 1.5: Graph of thickness vs cell voltage with different categories of TiO_2 films.

Due to an increasingly higher desire for functional materials, surface nanostructuring with an increased surface-to-volume ratio of titanium oxides is becoming very popular in research. The first disordered nanoporous titanium oxides were obtained with anodic oxidation in diluted HF. Since then, many parameters of nanotube morphology, such as length, diameter, smoothness, and wall thickness, have been achieved. In this way, the surface area can be increased 100x or more compared to thin compact films. The formation of nanotubular films is possible because the compactly grown oxide layer gets locally dissolved due to the presence of fluoride ions. The TiO_2 layer is chemically attacked and dissolved by the fluoride ions and Ti^{4+} ions form TiF_6^{2-} ions with fluoride ions which are water-soluble. The fluoride concentration needs to be carefully controlled in order to not dissolve the oxide layer entirely. Additionally, by controlling the voltage and length of anodization time, the diameter and length of nanotubes can be controlled. The length of nanotubes can be up to a few micrometers or even more than 100 micrometers, if polar organic electrolytes are used. The formed nanotubes are usually amorphous and can be annealed in oxygen to crystallize or in ammonia to form TiON nanotubes [33].

1.4.3.2 Electrospinning

There are many methods for nanofibre fabrication and electrospinning is probably the most versatile among them. Electrospinning enables the production of metal, ceramic, polymer and composite nanofibres directly or with additional processing steps. The advantage of electrospinning compared to other methods is the ability to form various fibre assemblies which allows modifications specific to the desired application. The nanofibres can be produced in the form of nonwoven, aligned or patterned mesh, as three-dimensional structures, or as convoluted nanofibres [34].

Nanofibres and nanowires have, due to a very small diameter, a very high surface-to-volume ratio and may therefore drastically improve current technology and be even used in new applications. Nanofibres can be used in many different fields such as tissue scaffolding, filtration, protective clothing, nanoelectronics, and nanocatalysis. Compared to other nanofibre fabrication methods, electrospinning is more versatile, flexible and easier to use. Typically, an electrospinning setup can consist of only a syringe, a flat tip needle, a conducting collector, and a high voltage power supply (Figure 1.6) [34].

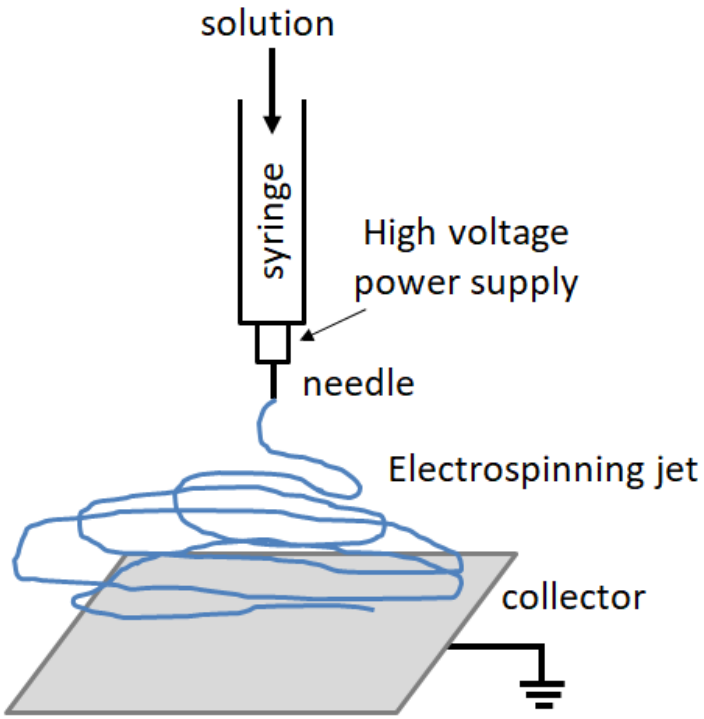

Figure 1.6: Typical electrospinning set-up.

The nanofibres form based on the uniaxial stretching of a viscoelastic solution. Electrostatic forces between the needle and the collector stretch the solution as it solidifies. The formation of the nanofibre can be continuous as long as there is enough solution to feed the electrospinning jet. Typically, a solution is fed through a spinneret (needle) where a high voltage is applied, usually over 5 kV. At critical voltage, the repulsive force within the solution is larger than the surface tension and a jet erupts from the spinneret. The jet is stable near the tip and becomes unstable farther away which causes further stretching of the solution jet due to electrostatic forces and solvent evaporation. Usually, a grounded target (collector) is used to collect the produced nanofibres. Many parameters can be adjusted to obtain the desired diameter of the nanofibres and other properties. Parameters that were widely studied are solution viscosity, concentration, applied voltage, conductivity, humidity, and distance between tip and collector. Different nanofibre assemblies can be obtained by manipulating the electric field or by using dynamic collection devices [34].

1.5 Electron Microscopy

Electron microscopes (EMs) use a beam of accelerated electrons as the illumination source. The beam of electrons is focused using electromagnetic lenses which are analogous to the glass lenses found in optical microscopes. The resolution of optical microscopes is limited by the wavelength of visible light and since electrons can have much shorter wavelengths than visible light, the resolution of EMs is much better compared to optical microscopes. EMs can be used to investigate various types of inorganic and organic samples on the nano-scale such as metals, crystals, microorganisms, and cells. There are many types of EM such as scanning electron microscopy (SEM), transmission electron microscopy (TEM), scanning transmission electron microscopy (STEM), reflection electron microscopy (REM) [35], [36] etc.

1.5.1 Transmission electron microscopy

In TEM, the accelerated electrons shaped into a parallel beam with electromagnetic lenses are transmitted through the analysed sample. The electrons interact with the material in the sample in many different ways which can give us different types of information. The transmitted electrons are typically detected by semiconductor-based detectors (cameras) or a fluorescent screen which is located below the sample. In order to obtain information about the sample with TEM, the electron beam needs to be able to pass through the sample. Therefore, the sample must be very thin (up to 100 nm) and the accelerating voltage must be high enough so that most of the electrons do not get absorbed by the material. Materials made from lighter elements (such as organic materials) absorb fewer electrons and can therefore be thicker, and materials made from heavier elements (such as inorganic materials) absorb more electrons and therefore need to be thinner. Due to the very high acceleration voltages of electrons (typically up to 300 kV), their wavelength is much smaller than that of visible light and together with lens aberration correction, the TEM enables imaging of columns of atoms or even single atoms (SAs). The TEM has a wide range of applications in the fields of materials science, nanotechnology, cancer research, virology and others and is considered as a major analytical method [37].

The TEM consists of a vacuum chamber with an electron gun at the top, electromagnetic lenses, apertures, a sample holder, and detectors at the bottom (Figure 1.7). In order for the electrons to move freely through the chamber, the vacuum needs to be ultra-high (10^{-4} Pa –10^{-6} Pa). This is achieved with a combination of rotary vane pumps, diffusion pumps and ion pumps or their equivalents. The electron gun is a cathode which is a source of electrons, typically made from a W filament in the case of thermionic sources or a sharp W needle or a LaB_6 single crystal in the case of field-emission sources. It is connected to a high voltage source which causes the emission and acceleration of electrons. Next is a series of independent electromagnetic lenses which together with apertures shape the electron beam to achieve the desired output image. In between, there is the specimen chamber with the specimen holder. Typically, the sample is put on a standardized TEM grid which is put on the specimen holder and inserted into the specimen chamber. For electron detection and imaging, special detectors such as charge-coupled device cameras or direct electron detectors and fluorescent screens are used at the bottom of the microscope. Besides imaging, electron diffraction is also possible with a few changes of the configuration of the electromagnetic lenses [37].

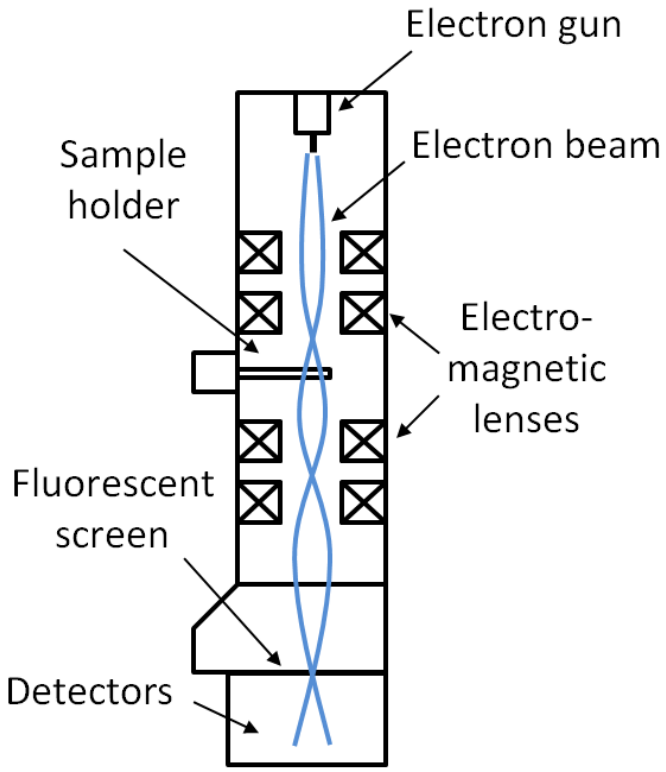

Figure 1.7: Scheme of a TEM.

1.5.2 Scanning electron microscopy

In SEM, the electron beam is focused into a point and scanned over the surface of the sample to form an image. The electrons interact with the atoms in layers near the surface of the sample and produce signals which are then detected to produce the image and give information about the size, shape, and composition. Similarly to TEM, the electrons are accelerated from the electron gun through the vacuum chamber and shaped by electromagnetic lenses and apertures. Then they interact with the sample and different signals are detected above the sample. Instead of transmitting through the sample, the electrons are backscattered or form secondary electrons, auger electrons, x-rays, or light. The acceleration voltage is lower compared to TEMs (1 kV – 30 kV) and it dictates the size of the interaction volume of the electrons with the sample (Figure 1.8). A smaller interaction volume means better resolution and a bigger interaction volume gives information from layers deeper under the surface of the sample. With different configurations and add-ons, the SEM can be used to observe specimens in variable pressures and temperatures [38].

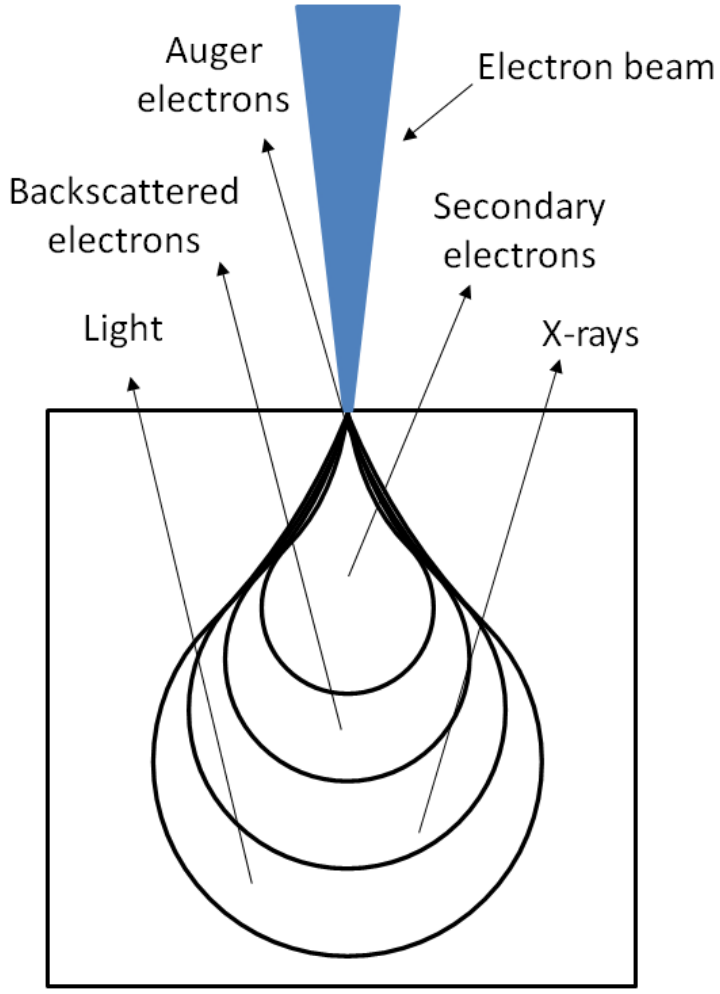

Figure 1.8: Scheme of the electron-matter interaction volume in SEM and the types of generated signals.

1.5.3 Scanning transmission electron microscopy

STEM is a sort of a combination of SEM and TEM modes and can be found as an operational mode in TEMs as well as SEMs. In STEM, the electron beam is focused into a point and scanned across the sample. Like in TEM, the sample needs to be transparent for electrons but because the beam is focused into a point and scanned over an area of the sample, additional signals can be detected and spatially reconstructed as opposed to TEM where the beam is parallel and hits a large area of the sample at the same time. The additional signals are scattered primary beam electrons which enable Z-contrast imaging, x-rays, and electron energy loss events. Elemental analysis of the samples on the nanoscale is possible with additional detectors which enable analytical methods such as EELS and energy dispersive x-ray spectroscopy (EDXS) [37].

1.5.4 Electron energy loss spectroscopy

The electrons in STEM have a very narrow distribution of energies (in the range of 0.5 eV – 1 eV at for example 200 keV) and when they pass through the sample some of them interact with the material and lose some energy characteristic to the type of interaction. Some of the interactions include plasmon and phonon excitations, Cherenkov radiation, and inner shell ionizations. Inner shell ionizations are characteristic to the element in which they happen and can therefore be used for qualitative and quantitative elemental analysis of the sample. What is more, the energy needed for the inner shell ionization also depends on the immediate environment of the ionized

atom and can therefore tell us something about the oxidation state of the element and types of chemical bonds. The obtained spectra from EELS can have an energy resolution better than 1 eV. Besides the elemental analysis, EELS can also be used to measure the thickness of the sample based on the ratio of electrons with no energy loss and all other electrons [37].

1.5.5 Energy dispersive x-ray spectroscopy

When the accelerated electrons in STEM transmit through the sample, some of them interact with the material and produce secondary emissions due to inner shell ionizations. One of these emissions are x-rays characteristic to each element which enables a qualitative and quantitative elemental analysis of the sample. Because the sample is very thin, the interaction volume is very small and thus a high spatial resolution is achievable (~1 nm). Compared to EELS, the energy resolution of EDXS is worse (more than 100 eV) and is less appropriate for analysis of lighter elements (for example C, N, O) [37].

1.5.6 Identical location electron microscopy

Identical location (IL) EM is a quasi in-situ method that enables a localized analysis of structural and compositional changes of the sample (on the nanoscale) in the IL before and after a change in the sample (synthesis step, degradation, change of conditions etc.) and brings new insights to mechanisms of change where in-situ measurements are limited or difficult to perform (for example reactions in liquid environments such as catalytic WE). Its advantage to ex-situ EM analysis is that the structural and compositional changes do not need to be statistically evaluated on a large number of changes but can be followed on individual particles in detail (even on the atomic level) to better understand the underlying mechanisms [39]. It was first developed by Mayrhofer et al. in 2008 [40] for the analysis of structural changes in Pt/C catalysts in PEM fuel cells (PEMFCs) and developed further since to be used in other types of FCs, batteries, WE, electrochemical synthesis, and heterogeneous catalysis [39].

1.6 NanoLab Concept – A Method for Analysis at the Nanoscale

NanoLab is a unique experimental platform that allows a detailed understanding of how the catalyst structure and composition dictate stability and activity, and how the local structural changes control catalyst performance during the electrochemical reaction. This is an important step towards expedited development of electrocatalysts because it enables observation of events on the nanoscale before and after electrochemical biasing as well as before and after catalyst synthesis. This NanoLab platform allows for tracking, observation, and detailed understanding of how electrocatalyst's local surface, structure, morphology, and composition change at the atomic level.

Since electrochemical methods are typically not coupled with spectroscopic and IL-EM methods used to evaluate changes in electrocatalysts, it is a challenge to interpret the produced electrochemical results and isolate how nanoparticles changed during electrochemical testing. A good approach to overcome this is to couple IL-TEM with electrochemical analysis. A wet impregnation method is mostly used to immobilize the electrocatalyst on the TEM grid for the IL-TEM technique. The electrocatalyst is then characterized with a floating electrode setup where the TEM grid is placed on the surface of the electrolyte solution and acts as a working electrode [41]. This setup is very effective at removing gas bubbles which form during the electrocatalytic reaction and enables reliable and fast electrochemical characterization. What is more, the floating electrode setup allows us to follow the structural and compositional changes of an electrocatalyst at an IL before and after electrochemical treatments at different magnifications.

Electrocatalysts on floating electrodes prepared by the wet impregnation method have the disadvantages of not being completely stable since they are not strongly attached to the TEM grid substrate, the dispersion of the catalyst film is not homogeneous throughout the entire TEM grid, it is more challenging to analyse the catalyst – support systems and the catalyst cannot be characterized after each synthesis step [42]. Anodic oxidation of the TEM grid to form a nanotubular support can eliminate all these disadvantages. If used, the anodically oxidized TEM grid acts as a high-surface-area support for the electrocatalyst that is strongly attached to the

TEM grid. Anodic oxidation of many different transition metals can be done [43]–[47] which has been demonstrated for differently shaped metals but not TEM grids [48]–[51]. The support needs to be electrically conductive which can be achieved by nitridating the formed TiO_2 on the TEM grid to obtain TiON.

Iridium nanoparticles are often dispersed on a high surface area support [52], [53], [62], [54]–[61]. However, many of the interactions between the catalyst and support are not yet well understood and they can potentially influence the electrochemical performance. In the case of TiON in conjunction with iridium catalyst, many of these interactions were already studied. Highly dispersed iridium nanoparticles [63] on nanotubular [64] or nanoribbon-like supports [65] and strong metal-support interactions (SMSI) [66], [67] have been already documented. Still, more insights on the suitability of TiON as an OER support are needed. One of the fundamental questions that needs to be resolved is how can TiON resist oxidation during OER conditions. Can the electrocatalyst play a role in this? By analysing the structural and compositional changes of the support as well as of the electrocatalyst itself, we can find answers to these questions.

The correct interpretation of the data obtained with IL-EM is crucial for understanding degradation mechanisms of electrocatalyst – support systems. To understand how a nanoparticle changes during the experiment, the images before and after an electrochemical treatment need to be compared. Following structural changes at the atomic level can be time-consuming and, to some degree, also subjective. Therefore, developing computer algorithms to analyse IL-EM images would be very advantageous [68]. Such algorithms were already used for ORR catalysts [69], but not for OER catalysts, to the best of our knowledge.

1.7 TiON Nanofibres

For applications such as supports for electrocatalysts in electrolysers, fast charge transfer and a large surface area are very desirable properties. Nanowires and nanofibres, which are 1D nanomaterials, offer some structural advantages. They have a low aspect ratio (dmin/dmax) and therefore fewer phase boundaries which enables a much higher electrical conductivity compared to other types of nanomaterials. These 1D nanomaterials have also a relatively very high surface area on which the electrocatalyst nanoparticles can be supported and keep a good electrical connection. Nanofibres are used in various applications such as photovoltaics, biosensors, tissue engineering, supercapacitors, hydrogen storage, fuel cells, water filters and more [70].

When considering nanofibres and nanowires for electrocatalytic applications, one of the most important properties is how good they conduct electricity. Many different methods can be used to measure the electrical conductivity of nanowires and nanofibres. According to the type of electrical measurement, the methods can be categorized into four categories: Impedance [71], Hall effect [72], two-probe electrical conductivity [73], and four-probe electrical conductivity [73], [74]. Electrical conductivity measurements can also be categorized by sample size: Single nanofibre/nanowire [75], [76], array of nanofibres/nanowires) [77], or bulk measurement [74].

Different types of nanofibres/nanowires with compositions related to TiON have been fabricated and their electrical conductivity was determined, such as TiO_2-based (TiO_2 [78], TiO_2N_x [71]), polymer-TiO_2 hybrid (PMMA/TiO_2 [79]), TiN-based (TiN [80], TiN/Cu [81]), and C hybrids (TiO_2/TiON/C [74], TiC/C [82]).

Other TiON nanomaterials with different structures and morphologies have been synthesized with their electrical properties determined, such as nanoparticles [83], [84], thin films [85]–[87], nanorods [88], [89], and nanostructures [90].

Specifically 1D TiON nanomaterials have also been researched with their electrical conductivity and other electrical properties measured [72], [76], [91]. Dong, J. et al. produced mesoporous TiON nanowires to be used as an anode in sodium electrochemical hybrid capacitors. The mesoporous TiON nanowires were produced by nitridating hydrogen titanate nanowires and the conductivity measurement was 3000 kS/m measured on a single nanowire via a two-probe conductivity measurement [76]. Chen, T. T. et al. fabricated TiON sheets which are flexible and porous and consist of TiON nanofibres. They were synthesized via a two-step process (nitridation after hydrothermal reaction) and used as an electrochemical electrode with the potential to be also used in supercapacitors. The bulk conductivity of the TiON sheets was from 1.66 kS/m to 31.45 kS/m measured using the Hall-effect measurement [72]. Noh, Y. et al.

fabricated 1D TiON nanowires to be used in electroreduction of oxygen and capacitive charge storage. The TiON nanowires were synthesized in two steps, electrospinning and nitridation and the electrical properties of the bulk sample were measured with impedance spectroscopy which showed that the electrical conductivity of TiON nanowire is increased due to the carbon species present [91].
.

Chapter 2

Aims and Hypothesis

The purpose of the dissertation is to evaluate the feasibility of TiON as a support for iridium (Ir)-based electrocatalysts for water electrolysis, finding methods to characterize the properties of TiON (N/O ratio, electrical conductivity) and determine the electrochemical stability of TiON support and TiON-Ir support-catalyst system based on electron microscopy imaging of the IL.

Currently, electrocatalysts for water electrolysis use high amounts of precious metals and/or are not very stable in the long run. Carbon-supported electrocatalysts are not very promising regarding long-term stability, as they degrade into gaseous CO_2. Our main goal is to explore if TiON is a better alternative to carbon supports regarding the stability and regarding the reduction of the precious metal use. These goals will be reached with thorough characterization of TiON and TiON-Ir with different methods before and after electrochemical degradation and with the explanation of the processes during degradation using IL-STEM on the atomic scale.

1. By developing specific synthesis procedures we can produce TiON with different chemical compositions, electrical and electrochemical properties, and morphologies which can be used for different applications and analyses. Nanoparticles can be used for classical catalyst systems and bulk characterization techniques, nanotubes from anodic oxidation for IL experiments and nanofibres for self-standing catalytic textiles and single nanofibre electric conductivity measurements. The determination N/O ratio of TiON can help us to evaluate this nanomaterial and compare different TiON nanomaterials to each other. By determining the N/O ratio of the synthesized samples, the synthesis procedures can be tweaked to obtain the desired N/O ratio and properties of TiON.

2. TiON is viable as a nanomaterial for the use as a support for Ir-based electrocatalysts for water electrolysis to reduce precious metal use and increase long-term stability. By dispersing Ir nanoparticles on TiON support we reduce the amount of Ir needed and also because of the synergistic effect between Ir and TiON the same amount of Ir is more electrocatalytically active. Contrary to carbon-based supports, which react with oxygen to form gaseous carbon dioxide, TiON reacts with oxygen to form titanium dioxide, which is a stable solid compound.

3. Using IL electron microscopy and analysis techniques is a great way to see what is happening to the TiON support and Ir electrocatalyst on the atomic scale and can tell us more about electrochemical stability. By studying the samples before and after electrochemical degradation we can explain the degradation mechanisms of TiON and Ir and by understanding the degradation mechanisms we can improve the catalyst – support system.

Chapter 3

Materials and Methods

3.1 Synthesis of TiON Nanopowders for N/O Ratio Determination

A series of TiON nanopowder samples was synthesized from TiN nanopowder (>99.2 %, 20 nm, US Research Nanomaterials, Houston, TX, USA) to obtain TiON nanopowder samples with different N/O ratios. For each sample, 50 mg of TiN was thermally treated in air. The temperature was increased with a rate of 7 °C min^{-1} to 120 °C for 1 h, then with a rate of 5 °C min^{-1} to 300 °C, kept at 300 °C for x h, and cooled with a cooling rate of 5 °C min^{-1} to room temperature. In total, 7 samples were prepared in this way with x being 1 h, 2 h, 3 h, 6 h, 12 h, 24 h, and 48 h. Additionally, the original TiN nanopowder was also used as an untreated sample (0 h).

3.2 Synthesis of TiON Nanotubular Structures and TiON-Ir Catalyst – Support Systems for Identical Location Analyses

3.2.1 Synthesis of TiON nanotubular structures as a support for small Ir nanoparticles

The Ti TEM grid (3.05 mm diameter, 400 mesh, Structure Probe Inc., West Chester, PA, USA) was in the first step subjected to anodic oxidation at constant potential in a two-electrode electrochemical cell which consisted of a stainless steel counter electrode and an anodization electrolyte. The anodization electrolyte solution consisted of 0.3 wt. % NH4F (99.99 %, Merck KgaA, Darmstadt, Germany) and 2 vol. % deionized water in ethylene glycol (99.5 %, Carlo Erba Reagents, Emmendingen, Germany). The anodizing time was 30 min and the anodizing voltage was 40 V. The anodization of the small titanium TEM grid was possible due to the development of a special anodization apparatus. The grid was inserted into the apparatus, sealed, and connected to an electrical contact. The procedure produced an amorphous TiO_2 nanotube film on the TEM grid itself. The TEM grid was then washed with deionized water and dried in a nitrogen atmosphere. The anodized TEM grid was annealed at 450 °C in air for 1 h to heighten the mechanical stability of the TiO_2 nanotubular film. A second annealing was performed afterward in an ammonia atmosphere at 700 °C for 2 h (the heating and cooling rate was 5 °C min^{-1}). This step converted the crystalline TiO_2 nanotubular arrays into the TiON substrate. The flow of pure ammonia gas was 50 cm^3 min^{-1} at a pressure of 1 atmosphere. One sample of TiON support was prepared in this way.

3.2.2 Addition of small Ir nanoparticles

After the synthesis of the TiON substrate, the iridium nanoparticles were deposited on top by the following procedure. First, 15 mg of $IrBr_3 \bullet xH_2O$ (Sigma-Aldrich, St. Louis, MO, USA) were dissolved in 1.5 mL of deionised water at 50 °C. Then, the solution was applied on the TiON substrate with the dip coating method with a withdrawal speed of 1 cm s^{-1} and subsequent drying at 50 °C. The sample was afterward thermally treated in a 5 % H_2/Ar gas mixture. The temperature was increased with a rate of 2 °C min^{-1} to 400 °C, kept at 400 °C for 1 h, and cooled

with a cooling rate of 3 °C min^{-1} to room temperature. One sample of TiON-Ir catalyst – support system was prepared in this way.

3.2.3 Synthesis of TiON nanotubular structures as a support for big Ir nanoparticles

The procedure was the same as in 3.2.1 except the temperature in ammonia atmosphere was 730 °C.

3.2.4 Addition of big Ir nanoparticles

In the next step, Ir nanoparticles were deposited on the TiON support by using the dip coating method. The TEM grid was dipped halfway in the water solution of $IrBr_3 \bullet xH_2O$ with a concentration 20 mg ml^{-1}. The withdrawal rate was 1 cm s^{-1} and the TEM grid was subsequently dried at 50 °C. The sample was then thermally treated at 700 °C for 15 min in a 5 % H_2/Ar atmosphere. The heating and cooling rate was very fast, 100 °C min^{-1}. One sample of TiON-Ir catalyst – support system was prepared in this way.

3.3 Synthesis of Carbon TiON Nanocomposite Nanofibres for Electrical Conductivity Measurements

To prepare carbon TiON nanocomposite nanofibre (CTiON-NCNF) fabrics for the microstructure analysis, composition, and in situ four-probe conductivity measurements, a procedure was chosen that produces CTiON-NCNFs with a wider diameter distribution. In this way, single CTiON-NCNFs suitable for the measurements could be chosen more easily. A polymer solution was prepared from 1.7 g TIP, 0.8 g PVP, 4.2 g ethanol, and 3.3 g acetic acid. First, PVP was dissolved in ethanol and then TIP and acetic acid were added. To feed the polymer solution to the needle, a syringe pump (model R-99E, RazelTM, Linari Engineering, Pisa, Italy) was used, with a flow rate of 763 μL h^{-1}. At the needle, a voltage of 10.0 kV was achieved with a voltage generator (model HVG-P60-R-EU, Linari Engineering, Pisa, Italy). A voltage of +10.0 kV was applied to the needle that was positioned 15 cm away from the nozzle. Electrospinning was performed at 21 % relative humidity and 23 °C. The sample name CTiON-NCNF1 will be used where this type of CTiON-NCNFs was used (1st sample).

For capacitance and sheet resistivity measurements, a procedure was chosen that produces CTiON-NCNFs with a narrower diameter distribution. This was done to compare the sheet resistivity results and the theoretical model. A polymer solution was prepared from 1.0 g titanium (IV) isopropoxide (TIP, 97 %, Merck KgaA, Darmstadt, Germany), 0.6 g Polyvinylpyrrolidone F90 (PVP, BASF, Ludwigshafen, Germany), 6.4 g ethanol absolute (ethanol, Merck KgaA, Darmstadt, Germany), and 2.0 g glacial acetic acid (acetic acid, Merck KgaA, Darmstadt, Germany). First, PVP was dissolved in ethanol and then TIP and acetic acid were added. The nanofibres were synthesized with the electrospinning method using a Spinbox system (BioInicia, Valencia, Spain). The syringe with the polymer solution was connected to the pump, which generated a flow rate of 800 μL h^{-1}. A high voltage of +14.5 kV was applied to the needle which was positioned 15 cm away from the nozzle. Electrospinning was performed at 50 % relative humidity and 26 °C. The sample name CTiON-NCNF2 will be used where this type of CTiON-NCNFs was used (2nd sample).

To make the electrospun nanofibres electrically conductive, a thermal treatment in an ammonia atmosphere was done. The heating rate was at first 2 °C min^{-1} up to 250 °C and was kept at 250 °C for 1 h, then heated again at a heating rate of 5 °C min^{-1} to 700 °C and was kept at 700 °C for 2 h, and then cooled with a cooling rate of 5 °C min^{-1} to room temperature. The flow of ammonia gas was 50 cm^3 min^{-1}.

3.4 Sample Preparation of CTiON-NCNFs

3.4.1 Resistivity of single CTiON-NCNF1s

A small piece of the CTiON-NCNF1 fabric was put into MiliQ water and broken up with tweezers and vigorous mixing into tinier pieces. The suspension was mixed with a few 100 mL of MiliQ

water. The suspension was left to settle down. The excess water was decanted. This removed smaller pieces of nanofibres and other impurities. With a pipette, 2 µL of the suspension was drawn and put on the Protochips Electrical E-chip (finger configuration—fusion select, Protochips inc., Morrisville, NC, USA) with the drop coating method as close to the electrical contacts as possible and the drop was left to dry. The platinum contacts connecting the CTiON-NCNF1 with the chip electrical contacts were made in the Helios Nanolab 650i Dual-beam focused ion beam (FIB) SEM (FIB-SEM) system (Thermo Fisher Scientific, Waltham, MA, USA). The E-chip with the connected CTiON-NCNF1 was put on Protochips Fusion select holder (Protochips inc., Morrisville, NC, USA), inserted into a TEM, and connected to Protochips Aduro™ power supply (Protochips inc., Morrisville, NC, USA) for in situ four-probe electrical measurements.

3.4.2 Bulk resistivity of nanofibre fabric

The van der Pauw method [92], [93] was used to measure sheet resistivity of CTiON-NCNF2 fabric samples. Sheet resistivity of solid samples of any shape can be accurately measured with this method. The samples were cut into a 10 mm × 10 mm × 30 µm square and attached with a conductive silver paste to a square printed circuit board with pins soldered to copper in all four corners. This setup enables a good electrical connection between the measuring equipment and the fragile sample. A multichannel potentiostat BioLogic VMP3 (Biologic, Seyssinet-Pariset, France) was used for the measurements.

3.4.3 STEM, EELS and STEM EDXS analysis

The sample needed to be prepared in two ways. To analyse individual CTiON-NCNF1s, a small piece of the fabricated CTiON-NCNF1 fabric was rubbed onto a TEM grid (lacey carbon on copper, mesh 300, Structure Probe Inc., West Chester, PA, USA) with a toothpick. Compressed air was used to blow away excess material. To make a FIB lamella of the cross-sections of CTiON-NCNF1s, 2 µL of the suspension (prepared in the same way as for electrical measurements of single CTiON-NCNF1s) were drop-coated on a piece of silicon wafer and dried. The prepared sample was further treated in the FIB-SEM. A location on the CTiON-NCNF1s fabric was chosen where a couple dozen of CTiON-NCNF1s were parallel to each other. The CTiON-NCNF1s were covered with a thick layer of platinum and Ga ion sputtering was used to cut out a lamella. The lamella was attached to a lift-out TEM grid (Omniprobe, 3 post, copper, Structure Probe Inc., West Chester, PA, USA) and Ga ion sputtering was used for additional thinning.

3.5 Electrochemical Characterization and Degradation

3.5.1 TEM grids

A modified floating electrode (MFE) apparatus was used for electrochemical experiments [94] on TEM grids. The two-compartment cell (H – cell) was separated by a Nafion membrane (Nafion 117, FuelCellStore, College Station, TX, USA) (Figure 3.1). The MFE apparatus consists of a gas diffusion layer (GDL, 280 µm thickness) with 40 % Teflon weight wet proofing (Toray Carbon Paper 090, FuelCellStore, College Station, TX, USA), a two-piece Teflon housing which is assembled with Tekka Peek screws (Tekka Peek, Nufringen, Germany), a metallic spring which is inserted between two metallic cones, and the TiON-Ir TEM grid which is used as the working electrode. The GDL serves as a separator between the electrolyte and the metallic cones and spring, which are used as electric contacts. A Pt mesh (50 mm × 50 mm, GoodFellow, Cambridgeshire, England) and a reversible hydrogen electrode (HydroFlex®, Gaskatel, Kassel, Deutschland) were used as counter and reference electrodes, respectively. To prevent Pt deposition on the TEM grid, the counter electrode was placed in a separate compartment. As an electrolyte, a freshly prepared 0.1 M perchloric acid ($HClO_4$, 70 % Rotipuran Supra, Carl Roth GmbH + Co. KG, Karlsruhe, Germany) was used. The acid was diluted with MilliQ water. The system was purged with inert Ar gas through a tube that was inserted in the holes of the MFE Teflon housing. The TEM grid was imaged with STEM before it was electrochemically treated. Different TEM grid samples underwent different electrochemical treatments.

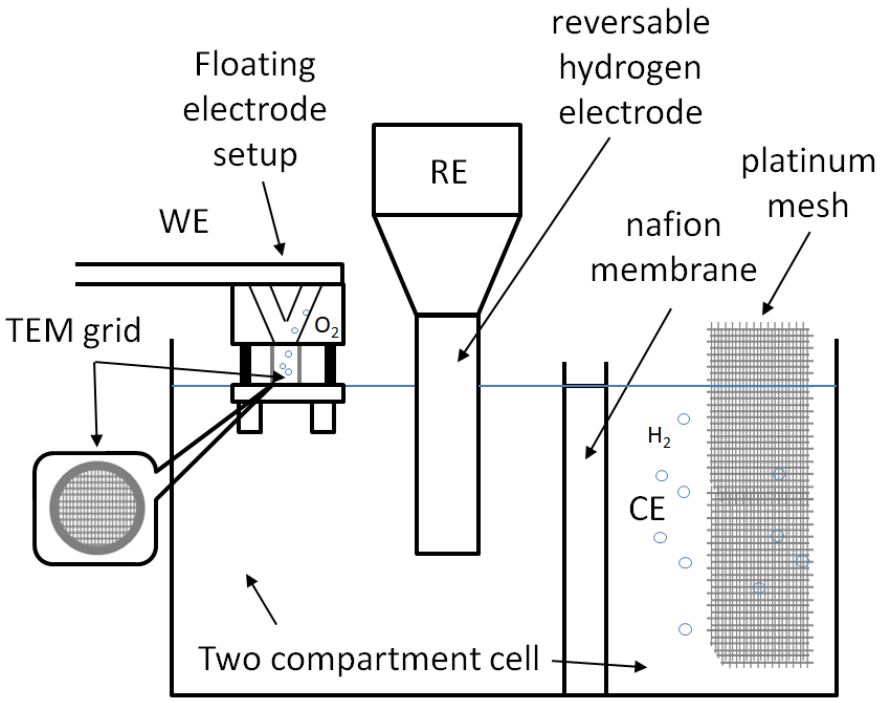

Figure 3.1: Schematic presentation of modified floating electrode setup. working electrode (WE), reference electrode (RE), and counter electrode (CE).

3.5.1.1 TiON TEM grid

At first, the TiON sample was assessed with a voltammetric pretreatment (300 mV/s, 0.05 V – 1.45 V) to confirm proper electrochemical contacting. Then, the TiON sample underwent potentiostatic degradation at 1.6 V for 30 minutes. After that, the electrocatalytic performance was determined by linear sweep voltammetry (LSV) measurement (20 mVs^{-1}). No Faradaic response under OER-relevant potentials was observed for the TiON sample which was expected based on past research (data not shown) [95].

3.5.1.2 TiON-Ir TEM grid with small Ir nanoparticles

The TiON-Ir sample underwent two different electrochemical protocols. The same as with the TiON sample, proper electrochemical contacting was assessed in the beginning with a voltammetric pretreatment (300 mV/s, 0.05 V – 1.45 V). Electrocatalytic performance was determined after that by LSV measurement (20 mVs^{-1}, Figure 4.9b). To avoid the accumulation of evolved oxygen bubbles on the Ir-based analogue, the same protocol was slightly modified. The catalyst surface could be blocked by bubbles and lead to misleading results [96]. The protocol was 20 × 5 min potentiostatic intervals at 1.55 V which were interrupted with 2 min steps at 0.78 V (this square-wave degradation protocol is going to be referred to from here on as SW-DP). After that, a more rigorous electrochemical protocol was employed. A voltammetric perturbation with a widened potential window was selected (150 cycles, from 0.05 V to 1.6 V). This cyclovoltammetric degradation protocol is going to be referred to as CV-DP from here on [97]–[99].

3.5.1.3 TiON-Ir TEM grid with big Ir nanoparticles

The electrochemical protocol for the TiON-Ir sample with big Ir nanoparticles consisted of a potentiostatic hold at 1.6 V for 30 min in the first step. Catalyst activity was measured with 3 consecutive cycles with a scan rate of 10 mV/s between 1.2 V and 1.6 V before and after the potentiostatic hold. Next, STEM was used for structural characterization. In the next step, 3

cycles of a dynamic degradation protocol were used. Each of the 3 cycles consisted of intervals at 0 mA cm^{-2} (45 s) and 5 mA cm^{-2} (30 s) which were repeated 60×. The system was purged with Ar after each cycle at open current potential (OCP) for 10 min. After that, 20 cyclic voltammograms with a scan rate of 300 mV/s between 0.05 V and 1.45 V were recorded to follow the structural changes of Ir. Catalyst activity was measured before and after the dynamic degradation protocol in the same way as for the potentiostatic hold. Ohmic drop compensation of 85 % was applied during all experiments. Structural characterization with STEM was performed again as the final step.

3.5.2 Nanofibres

The sample with dimensions 10 mm × 10 mm × 30 µm was put onto a gas diffusion layer (GDL, Spectracarb 2050A-1050, FuelCellStore, College Station, TX, USA) which served as a structural support and on top of that a Nafion 117 membrane (FuelCellStore, College Station, TX, USA) was put which ensured a good proton flow and prevented cell leakage. 4 M $HClO_4$ (Suprapur, Carl Roth GmbH + Co. KG, Karlsruhe, Germany) was used as the electrolyte. Pt mesh was used as the counter electrode. Cyclic voltammetry (CV) was measured at a scan rate of 10 mV/s from −0.15 V to 0.9 V. Electrochemical impedance spectroscopy (EIS) was performed from 1 MHz to 0.1 mHz with a PARSTAT 2273 potentiostat (Advanced Measurement Technology inc., Oak Ridge, TN, USA). A Biologic SP-300 potentiostat (Biologic, Seyssinet-Pariset, France) was used to obtain the charge–discharge curves at constant currents (4 Ag^{-1}, 10 Ag^{-1}, 20 Ag^{-1}, 40 Ag^{-1}, 60 Ag^{-1}) from 0.05 V – 0.9 V. The areal mass loading was 1 mg/cm^2 and the area exposed to the electrolyte was calculated to be 0.07 cm^2.

3.6 Scanning Transmission Electron Microscopy, Electron Energy Loss Spectroscopy, and Energy Dispersive X-Ray Spectroscopy

STEM imaging was performed in a probe Cs-corrected TEM Jeol ARM 200 CF (JEOL Ltd., Tokyo, Japan), equipped with a GATAN Quantum ER dual-EELS system (Gatan Inc., Pleasanton, CA, USA) and a silicon drift detector (SDD) JEOL Centurio energy-dispersive X-ray (EDX) spectrometer (JEOL Ltd., Tokyo, Japan). An operational voltage of 80 kV was employed. The images were taken in STEM mode (bright field (BF) and high angle annular dark field (HAADF)), probe size 6 C, 8 cm effective camera length, imaging angles were 68 mrad – 175 mrad. EELS analysis was done at probe size 6 C, 3 cm effective camera length, EDXS analysis was done at probe size 2 C, 8 cm effective camera length.

3.7 Scanning Electron Microscopy and Energy Dispersive X-Ray Spectroscopy

SEM and SEM EDXS were carried out using a field emission SEM (FE-SEM) Zeiss Supra TM 35 VP (Carl Zeiss AG, Oberkochen, Germany), equipped with an EDX spectrometer silicon drift detector (SDD) EDX Ultim Max 100 (Oxford Instruments, Oxford, UK). CTiON-NCNF2 and CTiON-NCNF1 samples were analysed. TEM grid samples were put on a STEM holder and nanofibre and nanopowder samples were put on carbon tape. The operational voltage for SEM was set to 1 kV–5 kV, working distance was 4 nm – 5 mm, aperture size was 30 µm, and the detector was a secondary electron detector and a back-scattered electrons detector. The operational voltage for SEM EDXS was 7 kV, working distance was 8.5 mm, and aperture size was 60 µm.

3.8 X-ray Photoelectron Spectroscopy

The XPS analyses were carried out on the PHI-TFA XPS spectrometer (Physical Electronics Inc, Chanhassen, MN, USA). The analysed area was 0.4 mm in diameter. Analysis depth by the XPS method is about 3 nm – 5 nm. Monochromatic Al X-ray beam of energy of 1486.6 eV was used for excitation. The accuracy of binding energies was about ± 0.3 eV. Quantification of surface composition was performed from XPS peak intensities taking into account relative sensitivity

factors provided by instrument manufacturer [100]. For TEM grids, surface composition and chemical status was analysed. Two measurements on every sample were performed. For TiON nanopowders, the surface of samples was analysed.

3.9 Raman Spectroscopy

Raman spectra were obtained using a confocal WITec alpha 300 spectrometer (WITec GmbH, Ulm, Germany). The spectra were recorded with a green 532 nm laser excitation wavelength.

3.9.1 Nanopowders

The nanopowders were deposited on a silicon wafer substrate and focused with a 20× objective. The spectra were recorded using an integration time of 1 s and 100 consecutive scans. Three to four spectra were measured at various positions on each of the powdered samples and the most representative were selected.

3.9.2 Nanofibres

Number of scans was 100 with an integration time of 1 s. The spectra were recorded on two different sites. At each site, four spectra were measured subsequently using the increasing laser powers of 0.3 mW, 0.6 mW, 1.4 mW, and 3.4 mW.

3.10 X-Ray Diffraction

X-ray diffractograms of the samples (TiON nanopowders, CTiON-NCNF2, and NH_4Br) were recorded with a PANalytical X'Pert PRO MPD X-ray powder diffractometer (PANalytical B.V., Almelo, the Netherlands). The radiation wavelength used was Cu Kα1 = 1.5406 Å in the α1 configuration with a Johansson monochromator on the primary side.

3.11 Thermogravimetric Analysis

Thermogravimetric analysis (TGA) of the samples (TiON nanopowders and CTiON-NCNF1 fabric) was performed in NETZSCH, model STA 409 C Simultaneous Thermal Analyser (NETZSCH-Gerätebau GmbH, Selb, Germany). Analysis was performed in an oxygen atmosphere in a Pt crucible. The heating rate was 10 °C/min and maximum temperature was 1100 °C.

3.12 CHNS Elemental Analysis

CHNS elemental analysis of the samples (TiON nanopowders and CTiON-NCNF1 fabric) was carried out with a PerkinElmer® 2400 Series II CHNS/O Elemental Analyzer (PerkinElmer inc., Waltham, MA, USA).

3.13 Optical Microscopy

Optical microscopy was done using an Optika Microscope SZM-B (Optika S.r.l., Ponteranica, Italy).

3.14 Density Functional Theory Simulations

The PWscf code from Quantum ESPRESSO [101] was used to perform the calculations using the GGA+U method [102], [103] with the exchange-correlation functional (ECF) of Perdew–Burke–Ernzerhof (PBE) [104]. Kohn–Sham orbitals were expanded in a plane-wave basis set with a kinetic energy cut-off of 50 Ry (575 Ry for the charge density). Projector-augmented-wave (PAW) potentials [105] were used which were obtained from pslibrary [106]–[108]. For Ti ions,

the *U* parameter was calculated from a TiON bulk structure self-consistently. The hp.x code that utilizes the density-functional-perturbation-theory (DFPT) scheme [109] was used. The TiON bulk model was taken from literature [66]; the crystal structure is a rock-salt type with Ti cations with 25 % of Ti-vacancies and two interpenetrating fcc latices of N/O anions. There is 1 Ti-vacancy in the unit cell and seven atoms (3Ti, 2N, 2O). Therefore, the stoichiometry of this TiON bulk model is $Ti_{1.5}ON$ (or $Ti_3O_2N_2$). The TiON bulk cubic unit cell can be seen as a TiN(001) layer and a TiO(001) layer. The Ti-vacancy can therefore be located in either of the two layers (Figure A.12). The two "ordered" structures, based on the unit cell with a Ti-vacancy in either the TiN(001) or the TiO(001) layer, are labelled as Ti-vac_N and Ti-vac_O, respectively. The Ti-vac_N and Ti-vac_O structures have an almost identical calculated lattice parameter (4.17 Å) and a very similar self-consistent value of the effective *U* parameter, 3.9 eV and 4.0 eV, respectively. Brillouin zone integrations (BZI) were performed with the Methfessel-Paxton smearing (MPS) [110] of 0.01 Ry and a 4×4×4 k-mesh which was uniformly shifted for the cubic unit cell of the TiON bulk. For other calculations, k-grids had comparable quality, except for Ir nanoparticles on TiON support calculations. These were performed with only the Γ k-point.

Experiments from previous research [66] revealed that the majority surface of the TiON substrate is (111), that is why we modelled the (111) surface with symmetric non-polar slabs which consisted of five Ti-layers terminated by an N/O layer on both sides of the slab. A minority of the calculations were performed using slabs containing 100 % of the N and O ions in the surface N/O layer and a majority of calculations were performed using stoichiometric slabs containing 50 % of N and O ions in the surface N/O layer.

To calculate the adhesion energy of Ir nanoparticles (NPs) on TiON support, the following equation was used:

$$E_{\text{adh}} = E_{\text{Ir}_n/\text{TiON}} - E_{\text{TiON}} - E_{\text{Ir}_n} \tag{3.1}$$

where $E_{\text{Ir}_n/\text{TiON}}$, E_{TiON}, and E_{Ir_n} are total (potential) energies of the relaxed Ir_n/TiON(111) system, relaxed bare TiON(111) slab, and relaxed standalone Ir_n nanoparticle, respectively.

The following strategy was utilized to determine if Ir NPs diminish the driving force to replace N atoms with O atoms. First, the adhesion energy of an Ir NP on a "pristine" TiON(111) surface ($E_{\text{adh}}^{\text{N}}$) was calculated. After that, on the surface below the NP, 2*n* N atoms were stoichiometrically replaced by 3*n* O atoms and the adhesion energy ($E_{\text{adh}}^{\text{O}}$) was calculated again. The Ir-induced N preference was finally calculated as:

$$\Delta = E_{\text{adh}}^{\text{N}} - E_{\text{adh}}^{\text{O}} \tag{3.2}$$

According to this definition, positive values of Δ indicate that Ir NPs destabilize the "pristine" TiON structure for replacement of N atoms by O atoms and vice-versa for negative values of Δ.

For Ir SAs, similar to Ir NPs, the Ir-induced N preference was calculated. The adhesion (or binding) energy for an Ir atom which is in a Ti-vacancy is calculated in the same way as in Eq. (3.1), i.e.:

$$E_{\text{b}} = E_{\text{TiON-Ir}} - E_{\text{TiON}} - E_{\text{Ir}} \tag{3.3}$$

where the energy terms mean something similar as in Eq. (3.1), except that here a single Ir atom is considered, and TiON can also be considered as a bulk structure. The Ir-induced N preference was calculated as a difference between the pristine E_{b}^{N} and the O-replaced E_{b}^{O}. For E_{b}^{O}, one N atom was exchanged with one O atom (the replacement of N with O was done in a 1:1 ratio). The Ir-induced N preference was finally calculated as:

$$\Delta_{1:1} = E_{\text{b}}^{\text{N}} - E_{\text{b}}^{\text{O}} \tag{3.4}$$

where the subscript 1:1 indicates that a single N atom was exchanged with one O atom. The $\Delta_{1:1}$ value measures the Ir-induced N preference of an Ir SA per replaced single N atom.

3.15 Programmes Used

Fiji (ImageJ) [111] programme (version 1.53o, Wayne Rasband and contributors, National Institutes of Health, USA) was used to determine the dimensions of the CTiON-NCNF2s and CTiON-NCNF1s. A custom-made programme was used to determine the nanoparticle size distribution (as equivalent radii) of CTiON-NCNF1s. To generate the XRD diffractogram, CrystalDiffract®, a powder diffraction programme for Mac and Windows (version 9.1.4(633), David Palmer, CrystalMaker Software Ltd., Oxford, England, www.crystalmaker.com, access date 23 June 2022) was used. The DTSA-II programme [112] (version Kelvin 2018-06-01, Nicholas W. M. Ritchie, Microanalysis Group, National Institute of Standards and Technology, Gaithersburg, MD, USA) was used to simulate the EDXS spectrum. The Jeol AnalysisStation® programme (version 3, 8, 0, 34, JEOL Ltd., Tokyo, Japan) was used to quantify the at. % from STEM EDXS spectra. The Gatan Digital Micrograph programme (version 2.32.888.0, Gatan inc., Pleasanton, CA, USA) was used to calculate the at. % of elements obtained from EELS.

3.15.1 Image processing algorithms

Segmentation of Ir nanoparticles on images (for TiON-Ir samples with small and big Ir nanoparticles) was done using a custom-made algorithm which is based on adaptive thresholding. Manual correction was used to correct discrepancies from the ground. All code was written in Python (version 3.8.5, Python Software Foundation, Beaverton, OR, USA) programming language using open-source libraries. The information about their area, circularity, and nearest neighbour distance was collected with Fiji (imageJ). Statistics were done in Excel (Microsoft Office Professional Plus 2010, version 14.0.7268.5000, Microsoft, Redmond, WA, USA).

To analyse atomically resolved IL-STEM images, in-house image processing algorithms written in Python were used. To determine positions of atomic columns, their initial approximations were determined by using a pre-processing step on the images and calculating centers of mass from intensity distributions of all columns. After that, the positions were refined by fitting 2D asymmetric Gaussian distributions (2DAGD) onto intensity values around the approximate positions. Centers of the fitted 2DAGD were used as the new positions. To assess atomic-scale surface roughness of nanoparticles, nearest neighbour analysis was used. The neighbouring columns of each atomic column were determined depending on how close they were to the column. Different colors were used to mark atomic columns based on how many nearest neighbours they had.

Chapter 4

Results and Discussion

4.1 Determination of N/O Ratio in TiON

The properties of TiON are highly dependent on its composition. TiON with more O has properties more similar to TiO_2, and TiON with more N has more properties similar to TiN. That is why the determination of the N/O ratio in TiON is important for the evaluation of newly synthesized TiON materials and relative comparison of similar TiON samples. There are many analytical methods that can be used for the determination of elemental composition (and N/O ratio from that) such as SEM EDXS, STEM EDXS, XPS, TGA + CHNS, and EELS. To evaluate the appropriateness of each of these analytical methods for N/O ratio determination, a series of TiON nanopowder samples with decreasing N/O ratios was prepared (see Experimental 3.1). As can be seen from XRD spectra of these samples (Figure 4.1a), the peak of the crystalline TiN/TiON is decreasing with increasing calcination time (at 300 °C), and after 12 h, peaks of anatase TiO_2 start appearing.

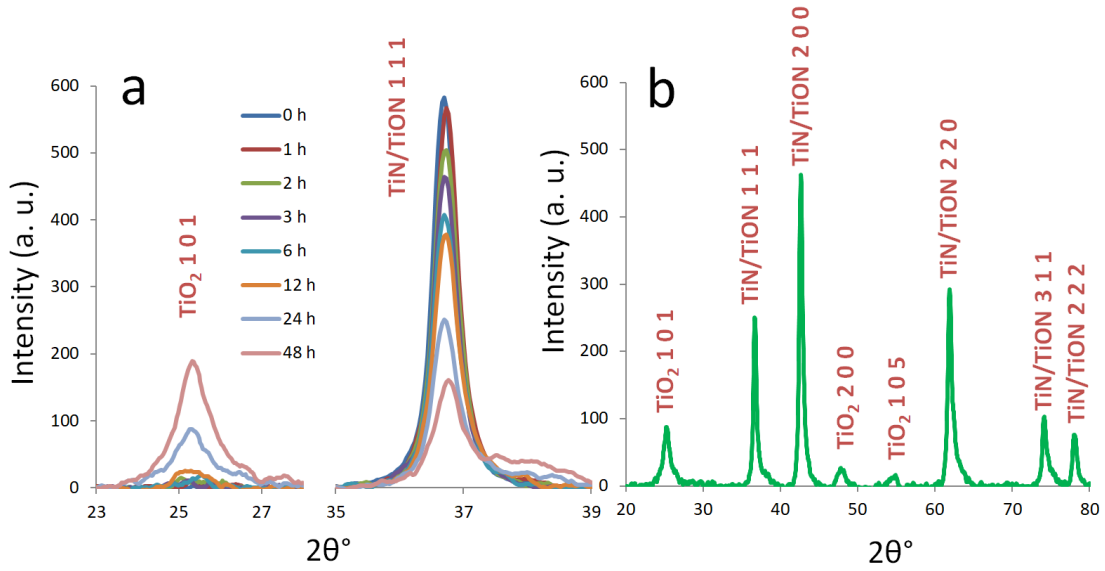

Figure 4.1: XRD spectra of TiON nanopowder samples calcined at 300 °C for different amounts of time. (a) anatase TiO_2 (1 0 1) and TiN/TiON (1 1 1) peaks for all samples from 0 h to 48 h, (b) extended XRD spectrum of the 24 h sample.

According to XRD results, a simple oxidation mechanism during the heating at 300 °C of the TiN/TiON nanoparticles can be proposed (Figure 4.2). Calcination causes formation of amorphous TiO_2 on the surface of the nanoparticles which decreases the crystalline TiN/TiON peak, and after 12 h, anatase TiO_2 forms on the surface from the amorphous TiO_2 while the amorphous TiO_2 progresses further into the core of the nanoparticle.

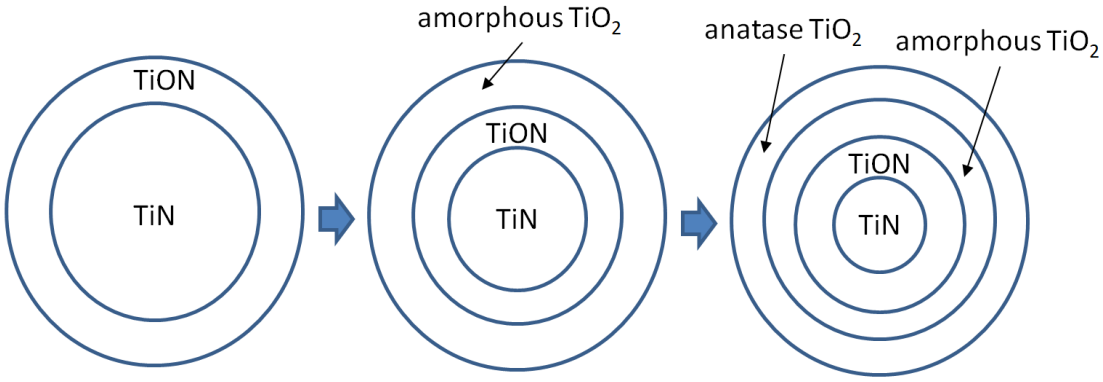

Figure 4.2: Proposed oxidation mechanism of TiN/TiON nanoparticles.

The N/O ratios, obtained from different analytical methods, can be seen in Figure 4.3a. It is clear that different analytical methods give different N/O ratios for the same sample. On the contrary, the trend along the series of samples is similar for all analytical methods where the N/O ratio is decreasing with increasing calcination time. This is also in agreement with XRD results. The reason for different N/O ratios from different analysis methods is probably mostly due to different analysis depths (Table 4.1). For example, XPS has a very shallow analysis depth (3 nm – 5 nm) and can therefore probe only the topmost layers of the 20 nm-sized TiON nanoparticles which get oxidized more than the core. This gives a lower N/O ratio. On the other hand, the analysis depth of SEM EDXS is in the range of micrometers and is far deeper than the diameter of the TiON nanoparticles; therefore the N/O ratio includes the N from the core and is thus higher.

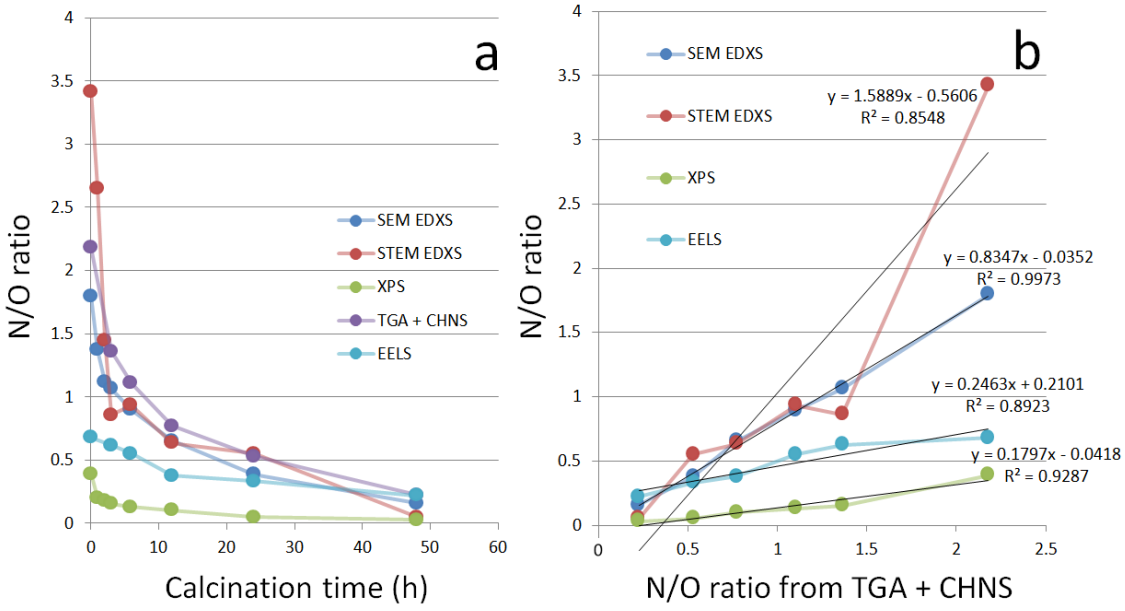

Figure 4.3: Graphs of N/O ratios (a) for all samples from 0 h to 48 h obtained from SEM EDXS, STEM EDXS, XPS, TGA + CHNS, and EELS and (b) correlation between TGA + CHNS N/O ratios and N/O ratios obtained from SEM EDXS, STEM EDXS, XPS, and EELS. Black lines are linear regression lines.

From all these analytical methods, TGA + CHNS method can be considered to give the most accurate results of the N/O ratio of a sample because it is a bulk method (details of this analytical method can be found in Appendix B.1 with CTiON-NCNF fabric as a sample). Additionally, both

TGA and CHNS are gravimetric methods and are therefore absolute analytical methods. Other analytical methods can be compared to TGA + CHNS to see if the obtained N/O ratios have a high correlation to the bulk N/O ratios (Figure 4.3b). N/O ratios from SEM EDXS and XPS analytical methods are highly correlated to the bulk N/O ratios because of their big areas (Table 4.1) which gives a good representative value comparable to bulk values. STEM EDXS and EELS, on the other hand, have lower correlation to TGA + CHNS because the analysis area is much smaller. This suggests that the TiON material is inhomogeneous. The small analysis area can be compensated with more measurements in many locations (details for N/O ratio determination from EELS analysis can be found in Appendix B.4 with CTiON-NCNFs as a sample, the average of 20 measurements were used for the TiON nanopowder samples). STEM EDXS and EELS have one advantage over the other methods, they can be used to determine local changes in the N/O ratio on the nanoscale in the IL (which is going to be discussed in more detail below, Section 4.2).

Table 4.1: Analysis depths and analysis spot sizes of different analytical methods.

Analytical method	Analysis depth	Analysis area
SEM EDXS	10^2 nm – 10^4 nm	5 nm^2 - 10^6 nm^2
STEM EDXS	5 nm – 10^2 nm	<0.1 nm^2 – 10^4 nm^2
EELS	5 nm – 30 nm	<0.1 nm^2 – 10^2 nm^2
XPS	3 nm – 5 nm	~ 4×10^5 nm^2
TGA + CHNS	bulk	bulk

Raman spectroscopy can also be used to follow changes in the amounts of TiN/TiON and TiO_2 in samples (Figure 4.4). The peaks at 199 cm^{-1}, 307 cm^{-1}, and 534 cm^{-1} correspond to TiN peaks found in literature [113]. With increasing calcination time, the peak at 199 cm^{-1} is steadily increasing. This is mostly due to the very sharp and intensive peak from anatase TiO_2 at 142 cm^{-1} [114] contributing to the peak at 199 cm^{-1}. The changes in peaks can only be described qualitatively for these samples.

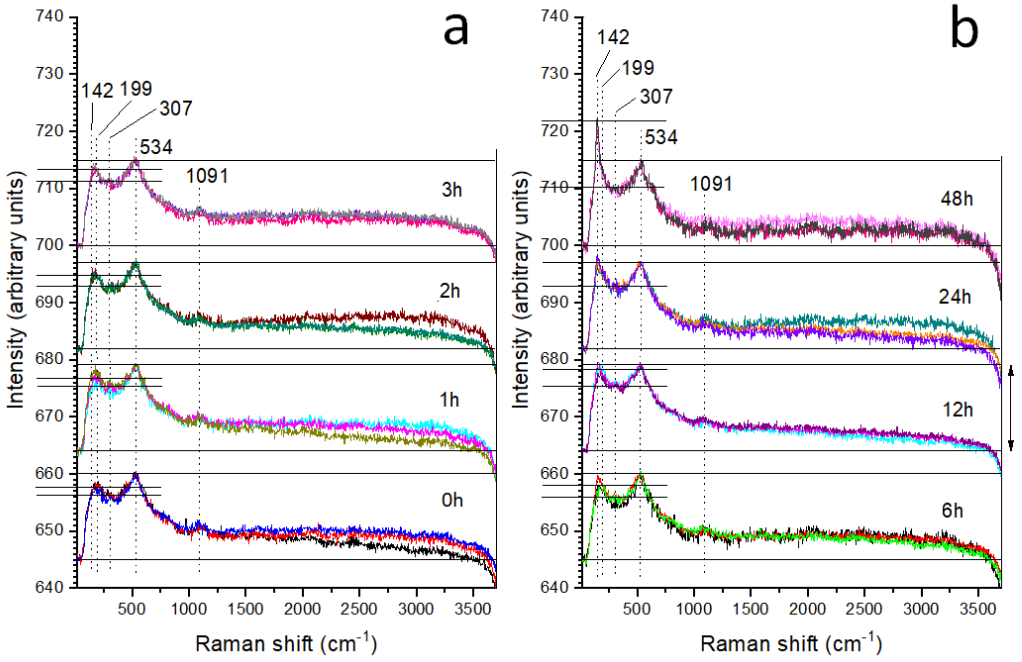

Figure 4.4: Raman spectra of TiON nanopowder samples (a) from 0 h to 3 h and (b) from 6 h to 48 h. The spectra were normalized to the 534 cm^{-1} peak.

4.2 IL-TEM of TiON and TiON-Ir

4.2.1 NanoLab concept

The idea of the NanoLab concept is based on the use of a Ti TEM grid as a substrate for catalyst – support system synthesis and structural characterization with atomic resolution at the nanoscale-level. The three most important techniques in the NanoLab concept are: IL-TEM technique as the main structural and morphological characterization method, electrochemical characterization of the TEM grid-based MFE, and anodic oxidation of the TEM grid as the main synthesis method (Figure 4.5). Other analytical methods can also be used which are complementary to the three main techniques such as IL-SEM, and XPS.

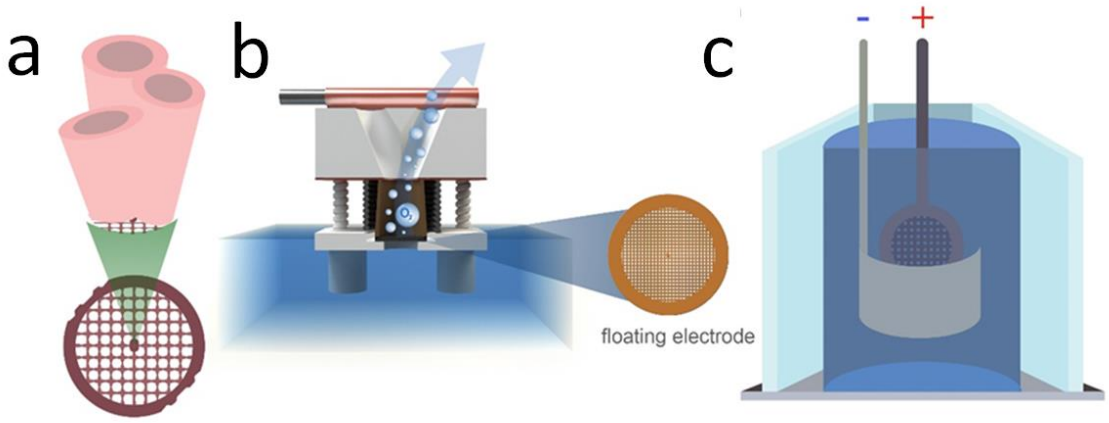

Figure 4.5: The three most important techniques in the NanoLab concept: (a) IL-TEM technique, (b) MFE setup for electrochemical characterization, and (c) anodic oxidation of TEM grid.

In order for the samples to be analysed with the IL-TEM technique and electrochemical characterization, the samples need to fulfil certain criteria. During the lengthy electrochemical testing, the TEM grid needs to remain mechanically stable and electrically conductive. For the electrocatalyst to be studied in each synthesis and characterization step, the electrocatalyst layer needs to be firmly attached to the TEM grid. In order to be transparent for the electron beam, the thickness of the electrocatalytic film also has to be in the order of a few 10 nm. The sample also needs to be stable in high vacuum and under electron beam illumination. IL-TEM analysis before and after electrochemical treatment is possible when all these requirements are met. This enables identification of local compositional and structural changes of an electrocatalyst at an IL.

To achieve these requirements, Ti TEM grids were anodically oxidized and nitridated which produced a TiON support with a high surface area. The TiON support was strongly attached to the Ti TEM grid and on it, the synthesis of a TiON-Ir OER electrocatalyst was easily executed and subsequent electrochemical treatment could be performed. IL-TEM and IL-SEM and, additionally, XPS, and electrochemical analyses were done at every experimental step. The experimental steps included synthesis and electrochemical treatment processes. This enabled a thorough description of the preparation of the electrocatalyst and the electrocatalyst itself. Additionally, optical microscopy was used which showed how the TEM grid sample was changing visually with each experimental step (Figure A.1, see Appendix A.1.1 for details). Figure 4.6 shows all the experimental steps during the development of the TiON-Ir electrocatalyst with the use of NanoLab method.

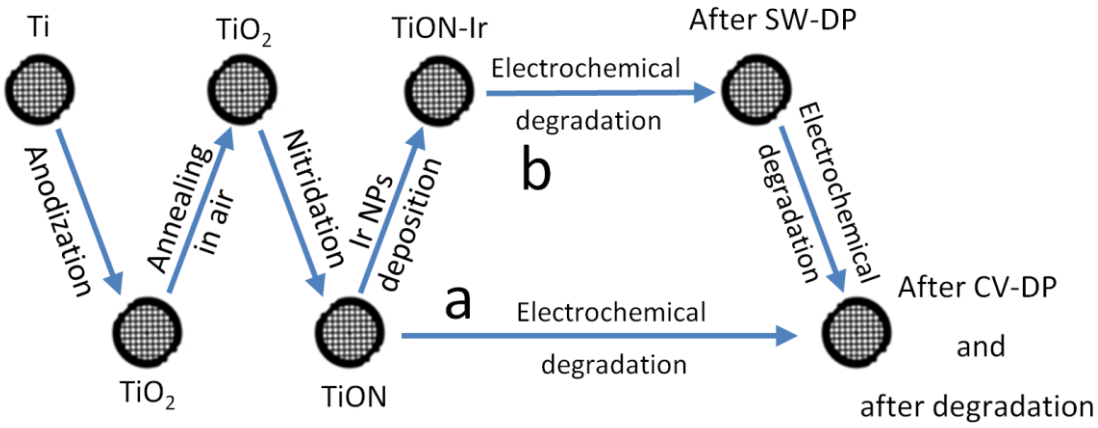

Figure 4.6: Synthesis, electrochemical degradation, and characterization of the TEM grid TiON-Ir electrocatalyst sample. Experimental route of the (a) TiON sample and (b) TiON-Ir sample. Each TEM grid represents a characterization step.

The Ti TEM grid was anodized with a custom-made anodic oxidation apparatus [115]. A high-surface area TiO_2, which is immobilized directly on the Ti TEM grid, can be made with this apparatus. The anodic oxidation method brings many advantages such as simplicity of the process, minimization of grid breakage, and the possibility to grow the film directly on the TEM grid. To grow a high-quality film with these benefits, optimal anodization conditions need to be found. Anodization voltage, electrolyte composition, and anodization time are the most important parameters. Different TEM grid mesh sizes and shapes can be anodized which limits the formed amorphous TiO_2 nanotubular film thickness and the surface area of the support. After anodization, annealing at 450 °C in air turns the amorphous oxide into anatase. To convert the anatase film into electrically conductive TiON, the sample is nitridated at 700 °C in NH_3 atmosphere. The TEM grid can become fragile if the sample is over-oxidized or over-nitridated. This can complicate sample manipulation between experimental steps.

Electrochemical analysis with the MFE setup is the next part of the NanoLab method (the TEM grid is the WE) [116]. In the MFE setup, the TEM-grid-supported electrocatalyst floats on the surface of the electrolyte solution. Bubbles can be efficiently managed in the case of OER (a reaction where gas is evolving), the electrochemical signal can be well-resolved and catalyst lifetime can be adequately predicted. If the bubbles are not removed, the electrocatalyst under the bubbles does not react further during electrochemical treatment and structural changes could be misinterpreted. In this MFE setup, the top of the WE is purged with Ar gas and specific electrochemical protocols are used for effective bubble management.

4.2.1.1 Morphology, composition and structure of the floating electrode

Figure 4.7a-f shows IL-SEM images at every step of the experiment (Figure 4.6c). A nanotubular TiO_2 structure is formed during anodic oxidation and the next experimental steps bring almost no noticeable change at this magnification. This means that changes to the sample did not occur at these scales. The Ti TEM grid was also imaged at low magnification before and after anodization (Figure A.4) where a slight decrease in the TEM grid hole size can be seen due to the formation of TiO_2.

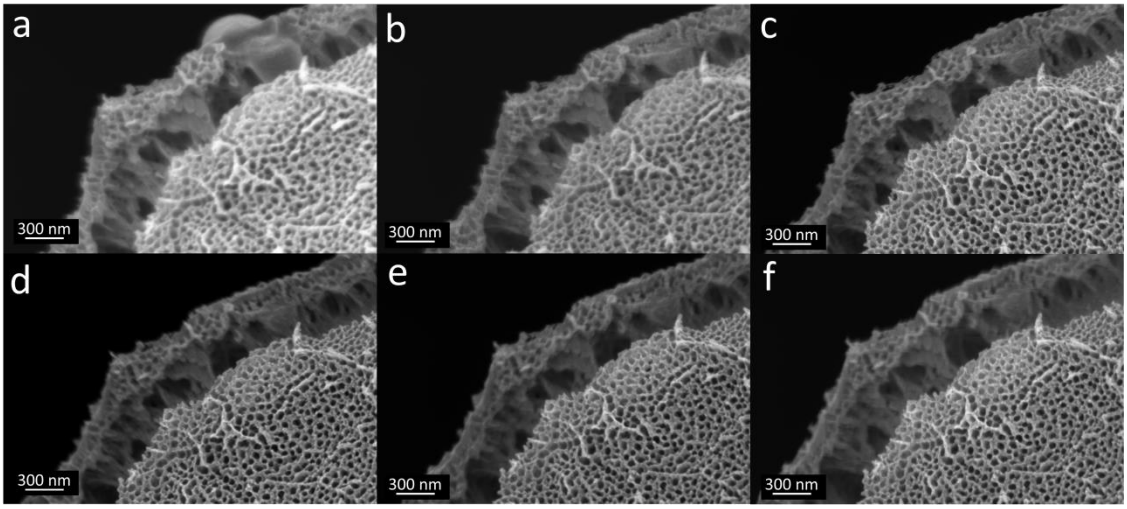

Figure 4.7: IL-SEM images at every characterization step: (a) anodization, (b) annealing in air, (c) nitridation, (d) reduction of Ir salts, (e) SW-DP, (f) CV-DP.

IL-STEM analysis was used to investigate the samples at higher magnifications. IL-STEM enables precise monitoring of even the slightest changes due to the experimental step taken **(**Figure 4.8a-l**)**. The annealing in air synthesis step shows a clear structural change of TiO_2 from amorphous to anatase phase (Figure 4.8, the change from a to b and g to h) [66]. During nitridation (formation of TiON), the polycrystalline anatase TiO_2 is restructured and the surface area increases (Figure 4.8b,c). Next, deposition of Ir NPs (1.53 nm^2 ± 1.43 nm^2) is achieved with the reduction of $IrBr_3$ salts in an Ar/H_2 atmosphere (Figure 4.8c,d,i,j). The edges of the TiON support also become less sharp due to the formation of an NH_4Br by-product as explained below (Figure 4.8c,d).

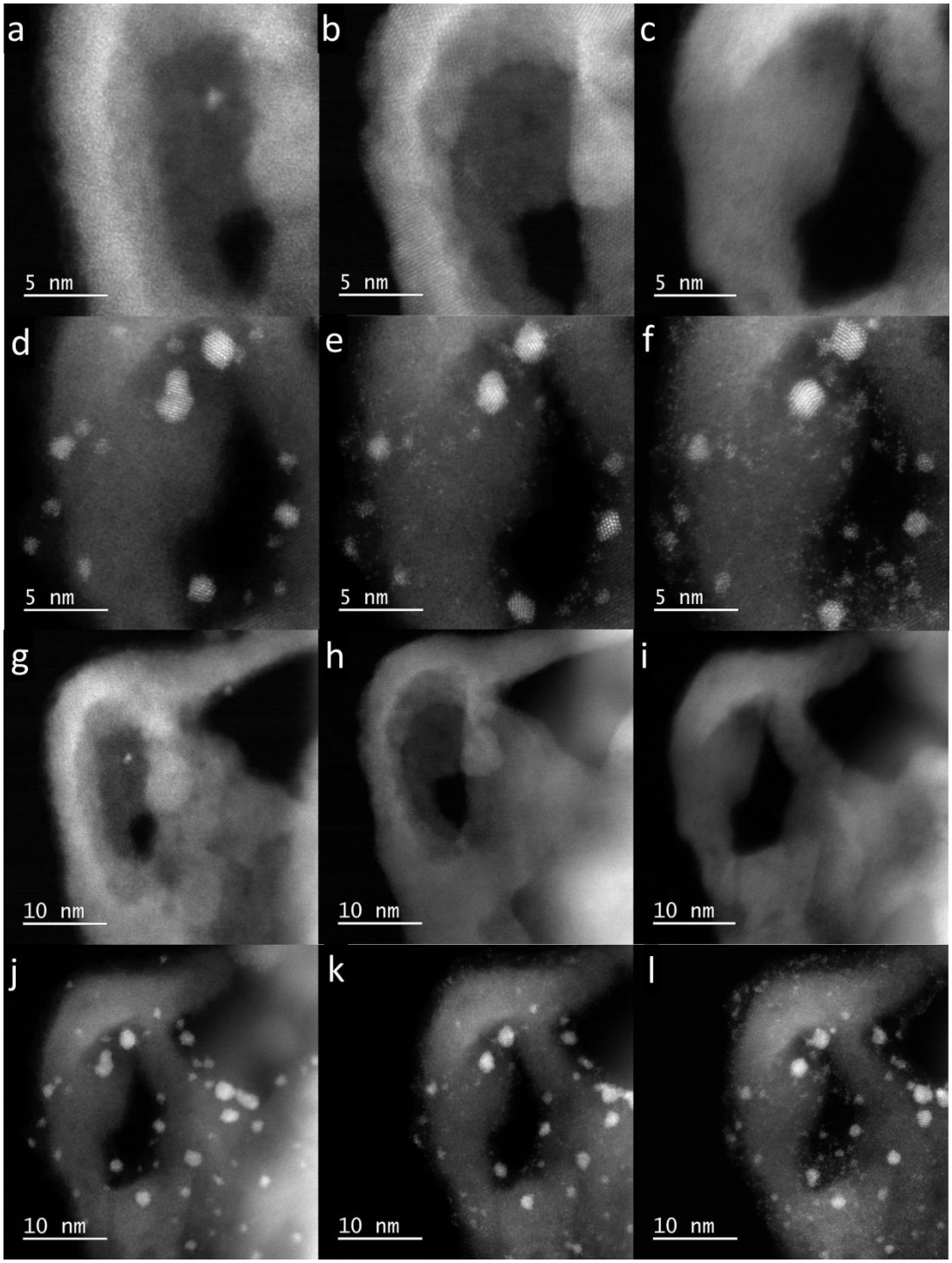

Figure 4.8: IL-HAADF-STEM images at every characterization step: (a,g) anodization, (b,h) annealing in air, (c,i) nitridation, (d,j) reduction of Ir salts, (e,k) SW-DP, and (f,l) CV-DP.

Table 4.2: N/O ratio at every characterization step from EELS, EDXS, and XPS analysis.

	N/O			
Sample stage	EELS	EDXS (location 1)	EDXS (location 2)	XPS
anodization				0.03
Annealing				0.02
Nitridation	0.67 ± 0.06	10.7	13.4	0.44
Ir NPs deposition	0.53 ± 0.07	3.5	3.5	0.30
SW-DP	0.46 ± 0.09	2.5	2.2	0.19
CV-DP	0.42 ± 0.07	1.8	1.6	0.21

The surface composition of the TEM grid sample was also analysed after each experimental step. The focus was on the N/O ratio and oxygen and nitrogen distribution determined by EELS, IL-EDXS, XPS, and EELS mapping. Table A.3 and Table A.2 show the elemental composition of the TEM grid sample. Different characterization techniques have different analysis depths which can cause differences in the obtained N/O ratio (Table 4.2**)**. For EELS, the analysis depth is 5 nm – 30 nm and for EDXS, the analysis depth is approximately 20 nm. For XPS, the analysis spot size is approximately 0.4 mm in diameter and the analysis depth is 3 nm – 5 nm. IL-EDXS results are also affected by the scattered x-rays from the Ti TEM grid core. Focusing on XPS results before nitridation, the TEM grid sample before and after annealing in air is closer to TiO_3 stoichiometry rather than TiO_2 stoichiometry (Table A.3). The excess of O is most likely due to surface contamination. The surface composition after nitridation was determined to be 23 at. % of N, 51 at. % of O, and 26 at. % of Ti (approximately $Ti_1N_1O_2$). Nitrogen replaced approximately one half of oxygen atoms in the TiO_2 structure based on the N/O ratio of 0.44. In the next synthesis step, which is Ir NPs deposition through reduction of $IrBr_3$ salts in an Ar/H_2 atmosphere, a slight decrease in the N/O ratio can be observed (Table 4.2). During reduction, NH_4Br forms as a by-product where TiON is the source of nitrogen. The by-product was determined from the synthesis of a similar sample in powder form and was analysed with XRD (Figure A.6). XPS shows approximately 1.6 at. % (0.7 at. % from IL-EDXS) of Ir after Ir NPs deposition. Of those 1.6 at. %, 40 % are in the Ir(4+) state and 60 % in the Ir(0) metallic state (Table A.2, see Appendix A.1.3).

IL-EELS mapping analysis showed a random distribution of O and N rich regions after nitridation (Figure A.7a). After Ir NPs deposition (Figure A.7e), N rich regions are concentrated in thicker regions and the O rich regions are moved to the grain boundaries of the support and its edges (thickness can be estimated from Figure A.7c,g,k,o – brighter regions are thicker). Presumably, the evolution of the NH_4Br by-product is causing this change. N/O ratio results from IL-EDXS are in agreement with XPS and EELS data (the N/O ratio is decreasing with every experimental step) even though light elements are less reliably quantified with EDXS (Table 4.2).

4.2.1.2 Electrochemical characterization of the MFE setup

Initial electrochemical experiments were used to confirm adequate electric contacting of the MFE setup and the presence of typical Ir electrochemical features and OER response. Cyclovoltammetry was used to show that characteristic Ir features were present (Figure 4.9d). LSV measurement (20 mVs^{-1}) was used to determine OER performance so that the TiON-Ir sample could be compared to other OER state-of-the-art electrocatalysts in the literature. Ir surface charge is directly related to the number of active sites [117]–[119], which is why the OER polarization curve was normalized to Ir surface charge. In this way, the capacitive current from TiON support is also eliminated [120]. A previous report on TiON-based analogues with similar Ir particle size distribution [67] is in agreement with the normalized specific OER activity (extrapolated at 1.55 V vs RHE, Figure 4.9b) of this TiON-Ir TEM grid sample. A Tafel slope of around 65 mV dec^{-1} was determined (Figure 4.9a), which was expected. Typical Ir-based catalysts (bulk IrO_2, rutile IrO_2, and electrochemically grown IrO_2) [59], [121]–[123] and also TiON-supported Ir analogues [64], [65], [67] have similar values. This means that this TiON-Ir TEM grid sample is not significantly different with regards to OER compared to other Ir-based catalysts.

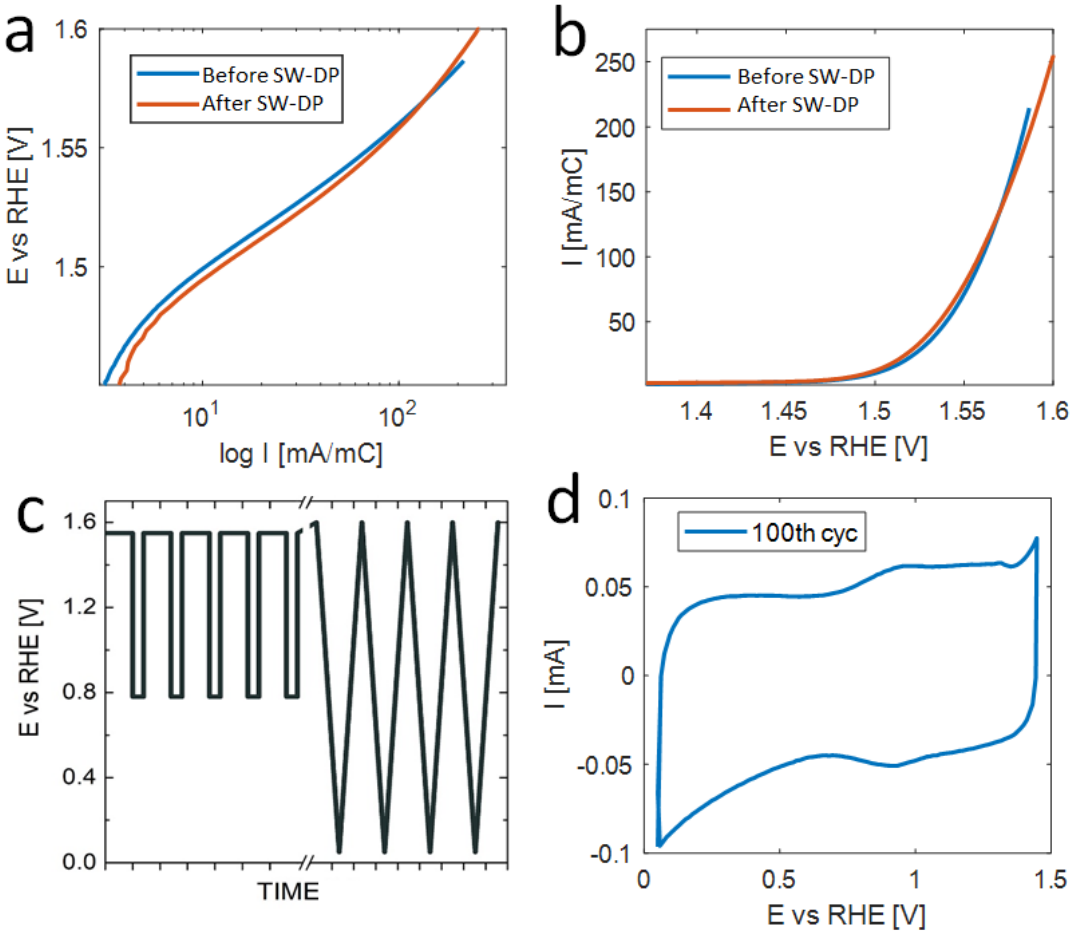

Figure 4.9: Electrochemical characterization of TiON-Ir TEM grid. (a) Tafel plots of OER polarization curves (constructed from b), (b) surface Ir charge normalized OER polarization curves measured before and after SW-DP electrochemical biasing, (c) potential – time diagram used for SW-DP and CV-DP electrochemical biasing (an example section of both protocols), and (d) cyclovoltammogram with characteristic Ir features.

4.2.1.3 IL-TEM characterization of the floating electrode after electrochemistry

The next step was to evaluate the applicability of combining IL-TEM analysis and electrochemical experiments. The goal here was to use a short electrochemical protocol to quickly trigger structural changes in Ir nanoparticles and the TiON support which could be well resolved with TEM analytical techniques to demonstrate the usability of the NanoLab method. SW-DP was used as the first electrochemical treatment of the TiON-Ir TEM grid sample. Changes in structure on the nano-scale with atomic resolution were followed on pre-selected locations before and after SW-DP. IL inspection of Ir NPs showed several examples of degradation processes due to electrochemical treatment (Figure 4.10). Dissolution, Ostwald ripening, coalescence, detachment, migration, rotation, and formation of Ir SAs are mechanisms induced by SW-DP that can be found in a single high magnification IL-STEM image pair. The OER performance is not significantly altered by these mechanisms during the duration of the experiment **(**Figure 4.9a,b**)**. Statistical analysis from IL-STEM images is in agreement with the negligible change in electrochemical activity. It can be concluded from the statistical analysis that average particle size, average circularity, average nearest neighbour distance, and particle size distribution stay almost the same and that less than 1 % of Ir particles are lost during SW-DP (Table A.1, Figure A.5). XPS analysis also shows only a slight decrease of at. % of Ir (from 1.6 at. % to 1.5 at. %) but Ir composition evidently changes after SW-DP, in contrast to statistical indicators of structural

changes. The composition goes from 40 % in the Ir(4+) state and 60 % in the Ir(0) metallic state before SW-DP to 70 % in the Ir(4+) state and 30 % in the Ir(0) metallic state after SW-DP (Table A.2, see Appendix A.1.3). This is in agreement with literature where the formation of surface/subsurface Ir(4+) oxide is reported in this potential window [124]–[127]. A decrease in N/O ratio of the TiON support due to SW-DP can also be concluded from EELS, IL-EDXS, and XPS analyses (Table 4.2). The EELS N/O values before and after SW-DP are within the measurement's uncertainty, which is why the change cannot be attributed to electrochemical oxidation of TiON with certainty. The results were compared to the bare TiON support TEM grid sample where the N/O ratio changed from 0.75 ± 0.13 to 0.23 ± 0.06 due to a similar degradation protocol. This is a direct confirmation of electrochemical oxidation of the TiON support. The significantly smaller N/O ratio decrease in the TiON-Ir TEM grid sample implies a potential protective effect of Ir on the TiON support during electrochemical oxidation. XPS analysis of the TiON-Ir TEM grid sample is in agreement with the EELS results (N/O ratio decreases from 0.30 to 0.19 due to SW-DP). Similarly, the N/O ratios obtained via IL-EDXS characterization also decrease (Table 4.2). The potential protective effect of Ir could be beneficially used to mitigate the TiON support degradation. A detailed understanding of this interaction might help advance this research field.

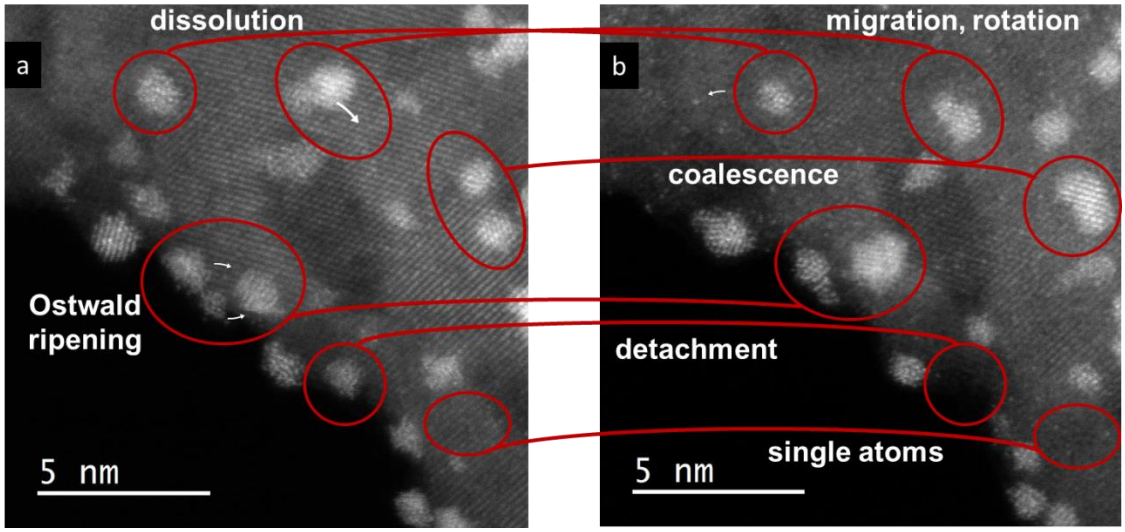

Figure 4.10: IL-HAADF-STEM images of the TiON-Ir sample (a) before and (b) after SW-DP. The images display many types of degradation processes of Ir nanoparticles in one image pair.

4.2.2 Single Ir atoms

The TiON and TiON-Ir TEM grid samples were compared in detail with electrochemical experiments coupled with IL-TEM diagnostics to better understand the potential protective effect of Ir on the TiON support.

4.2.2.1 Electrochemical characterization coupled with structural characterization

Two sequences of long-term electrochemical protocols (SW-DP and CV-DP, details can be found in Materials and Methods 3.5) were executed. As mentioned above, IL-STEM analysis shows no significant change in statistical indicators of the relevant structural characteristics after SW-DP and even after CV-DP (Table A.1, Figure A.5). On the contrary, XPS analysis shows that both electrochemical protocols changed the surface composition of the TiON support and of Ir. The amount of metallic state Ir(0) decreased from 60 % before degradation to 30 % after SW-DP to 0 % after CV-DP and the amount of Ir(4+) state increased from 40 % before degradation to 70 % after SW-DP to 100 % after CV-DP (Table A.2), which is in agreement with irreversible oxide formation [128]. The N/O ratio of the TiON support of the TiON-Ir TEM grid sample also decreases due to oxidation after the two electrochemical protocols (Table 4.2). The investigation

was upgraded with IL-EELS analysis of both the TiON-Ir and the TiON TEM grid sample with the goal to decouple the influence of Ir on the TiON support oxidation.

IL-EELS analysis of the bare TiON support TEM grid sample shows a significant decrease of the N/O ratio due to the electrochemical degradation (Figure 4.11, locations of the measurements can be seen in Figure A.8). This means that the electrochemical degradation caused an estimated 3 nm ± 0.4 nm (mean ± standard deviation) thick TiO_2 layer to form (a detailed explanation of thickness estimation can be found in Appendix A.2.1). After degradation, the N/O ratio becomes highly dependent on the TiON support thickness, which means that the thickness of the formed TiO_2 layer is somewhat constant through the sample. Based on that, it can be concluded that the TiO_2 layer is only on the surface of the TiON support and the TiON core is left intact (Figure A.11). On the contrary, IL-EELS analysis of the TiON-Ir TEM grid sample shows only a slight decrease in the N/O ratio due to SW-DP and CV-DP (Figure 4.12, locations of the measurements can be seen in Figure A.9). SW-DP caused an estimated 0.3 nm ± 0.3 nm and CV-DP caused an estimated 0.0 nm ± 0.6 nm thick TiO_2 layer to form. The difference between the thickness of the TiO_2 layer on the TiON and on the TiON-Ir sample is tenfold (10 ± 3), which shows that Ir efficiently prevents oxidation of the TiON support. There is also no clear dependence of the N/O ratio on thickness for the TiON-Ir TEM grid sample before and after both SW-DP and CV-DP (Figure 4.12).

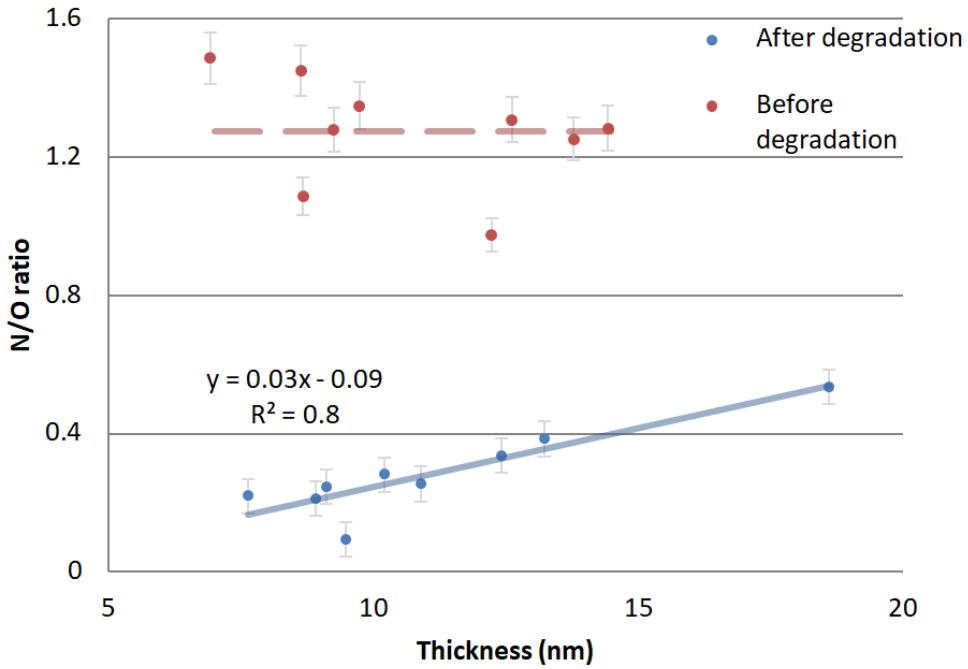

Figure 4.11: Graphs of the N/O ratio vs. thickness (nm) on the IL of TiON sample before and after degradation. Due to the low R^2 value (R^2<0.5) for the data before degradation, the average value (red dashed line) line was used instead of a linear regression line (blue full line).

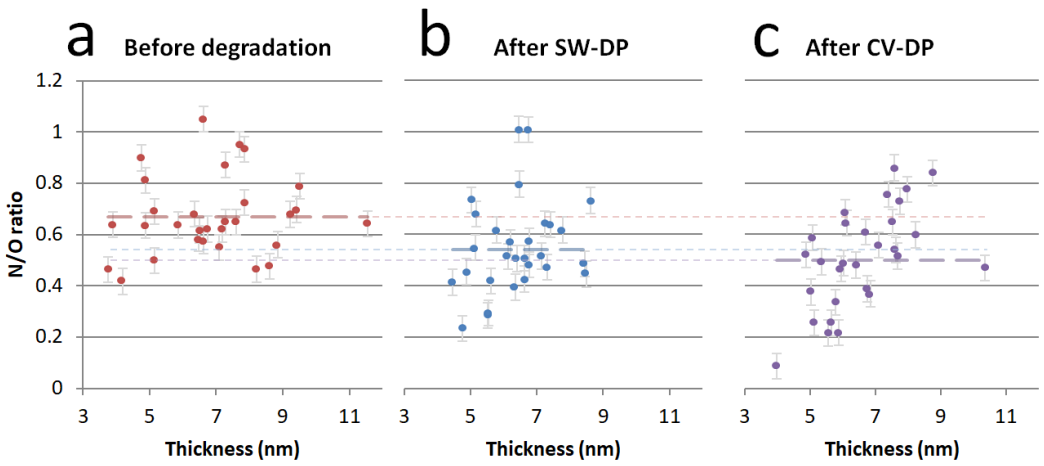

Figure 4.12: Graphs of the N/O ratio vs. thickness (nm) on the IL of TiON-Ir sample (a) before degradation, (b) after SW-DP, and (c) after CV-DP. Due to the low R^2 value (R^2<0.5), average value lines (red, blue, and purple dashed and dotted lines) were used instead of linear regression lines.

Atomically resolved IL-STEM analysis of the TiON-Ir sample was performed to understand the oxidation protection role of Ir in more detail. As mentioned above, several degradation mechanisms, due to electrochemical treatment, can be observed in one IL-STEM image pair at a high magnification (Figure 4.10) and the OER performance does not change in a meaningful way despite that (Figure 4.9a,b). Among these, the formation of Ir SAs stands out as a consequence of the electrochemical treatment (Figure 4.13). The brighter spots in the crystal lattice of TiON Figure 4.13b,c are Ir SAs (some are encircled in turquoise). The IL-STEM images of TiON-Ir in the zone axis [1 1 1] show that Ir SAs are mostly placed in Ti vacancies on the crystalline TiON support. The number density of the Ir SAs is higher after CV-DP (0.53 nm^{-2}, Figure A.10d) than after SW-DP (0.29 nm^{-2}, Figure A.10c). Also, there are more Ir SAs after CV-DP when the estimated thickness of the TiO_2 layer is lower (0.0 nm ± 0.6 nm) than after SW-DP when the estimated thickness of the TiO_2 layer is higher (0.3 nm ± 0.3 nm). This is an additional confirmation that the resistance of TiON to oxidation is induced by the presence of Ir (either Ir NPs and/or Ir SAs). The origin of Ir SAs was confirmed to be of electrochemical origin from IL-STEM images before Ir NPs deposition and before electrochemical degradation. There are no Ir SAs on the TiON support before Ir NPs deposition (Figure 4.13a, Figure A.10a), and only some (0.02 nm^{-2}) can be seen after Ir NPs deposition (Figure A.10b). Based on this, DFT calculations were made to theoretically evaluate the importance of Ir for the resistance of TiON to oxidation.

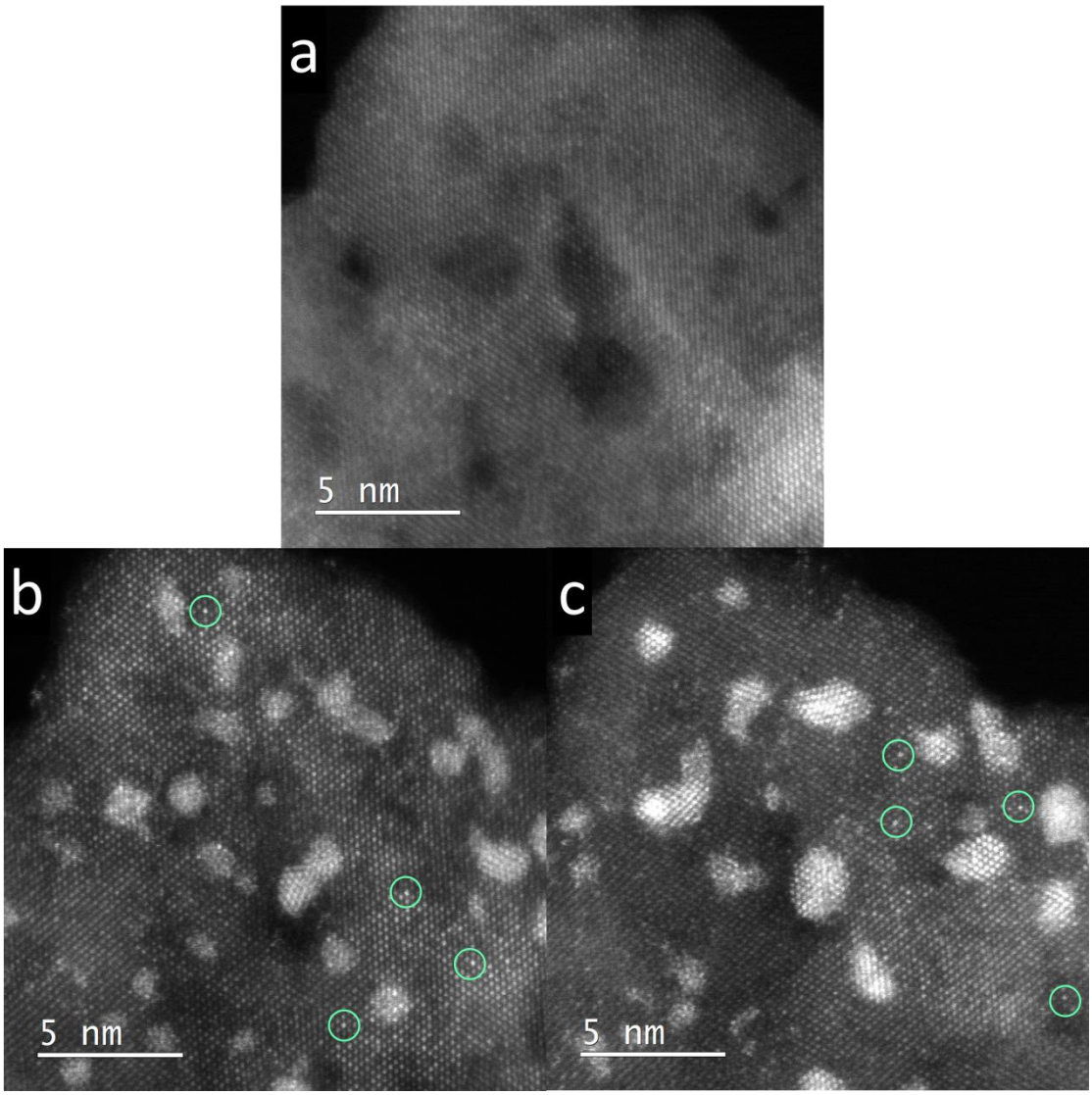

Figure 4.13: IL-HAADF-STEM images of (a) TiON, (b) TiON-Ir after SW-DP, and (c) TiON-Ir after CV-DP. An IL image of TiON-Ir before degradation was not taken. Green circles show example locations where Ti regular sites are occupied by Ir SAs.

4.2.2.2 DFT characterization of the role of Ir in stabilizing TiON

It was shown by our research group that N atoms considerably enhance the adhesion of Ir NPs on the TiON support [66]. If N atoms located below NPs are replaced with O atoms, a considerable weakening of the adhesion of Ir NPs can be observed. This is valid even if O atoms stoichiometrically replace N atoms (Figure 4.14). Meaning, if 3n O atoms replace 2n N atoms for $n \geq 1$, then the adhesion of Ir NPs is considerably weakened (n = 2 in the cases in Figure 4.14). Looking from the other perspective, it can be implied that the TiON structure is stabilized by Ir NPs because the driving force of O atoms replacing N atoms is diminished in the presence of Ir NPs. A confirmation of this is the Ir-induced N preference which was calculated by Eq. (3.2). It is considerable, the range is from −2.4 eV (for $Ir_{[1v,3]}$, the smallest considered NP) to −5.7 eV (for $Ir_{[12,10,6]}$, the largest considered NP). The number of Ir atoms in the considered NPs were 4, 7, and 10. If the Ir-induced N preference is normalized by the number of Ir atoms on the interface between the Ir NP and the TiON support, we get values from −0.5 eV and −0.6 eV per interface-Ir-atom.

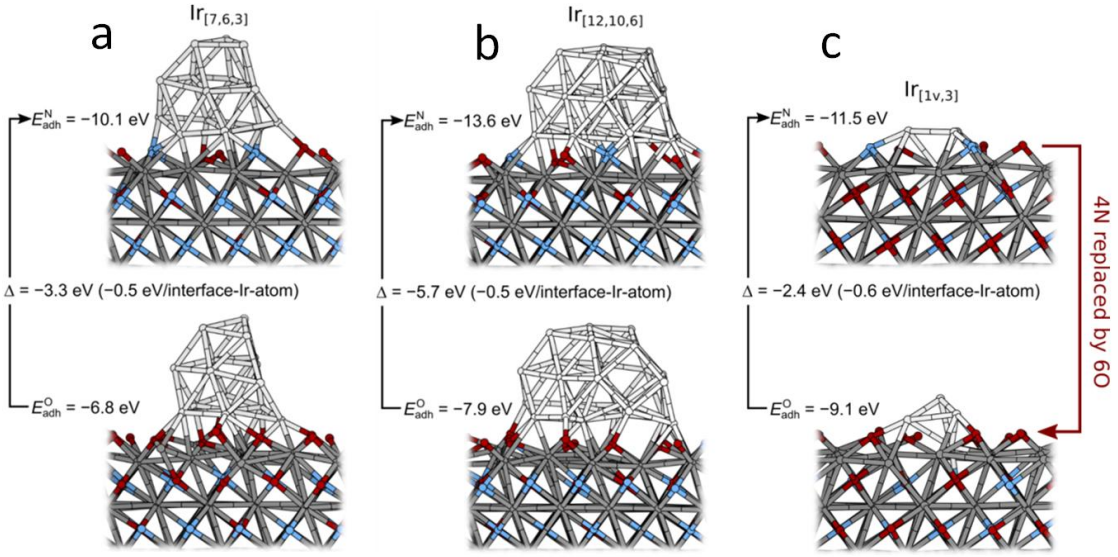

Figure 4.14: Snapshots of the Ir NPs on the TiON(111) surface of Ti-vac_O type (Figure A.12). (a) $Ir_{[7,6,3]}$, (b) $Ir_{[12,10,3]}$, and (c) $Ir_{[1v,3]}$ NPs. In the bottom row, the NPs are on TiON(111) where 4 N ions below the Ir NP were replaced by 6 O ions, and in the top row, the Ir NPs are on unaltered TiON(111). The Δ of Eq. (3.2) and adhesion energies are also shown. The Ir NPs have up to three layers and the number of Ir atoms in each layer is denoted as $Ir_{[i,j,k]}$ where *i*, *j*, and *k* represent the number of Ir atoms in the bottom, middle, and top layers. In the case of $Ir_{[1v,3]}$, one Ir atom is incorporated into a Ti surface vacancy and 3 Ir atoms are above it.

From these calculations it can also be concluded that Ir SAa can be incorporated into Ti vacancies of the TiON structure (either on the surface or in bulk). These Ir SAs also reduce the driving force for O atoms to replace N atoms and therefore stabilize the structure of TiON. The Ir-induced N preference calculated by Eq. (3.4) quantifies this (Figure 4.15). Ir SAs at many different concentrations were considered to be incorporated into Ti vacancies on the surface and in bulk of the TiON structure. As a result, the amount of stabilization induced by an Ir SA seems to be on average about 1 eV per N. This means that if one O atom replaces one N atom, which is bound to Ir, the adhesion (binding) of the Ir SA on a TiON(111) surface or in bulk is reduced by approximately 1 eV.

In summary, Ir NPs have a calculated Ir-induced N preference of approximately −0.5 eV per interface-Ir-atom and Ir SAs have a calculated Ir-induced N preference of approximately −1 eV per N atom.

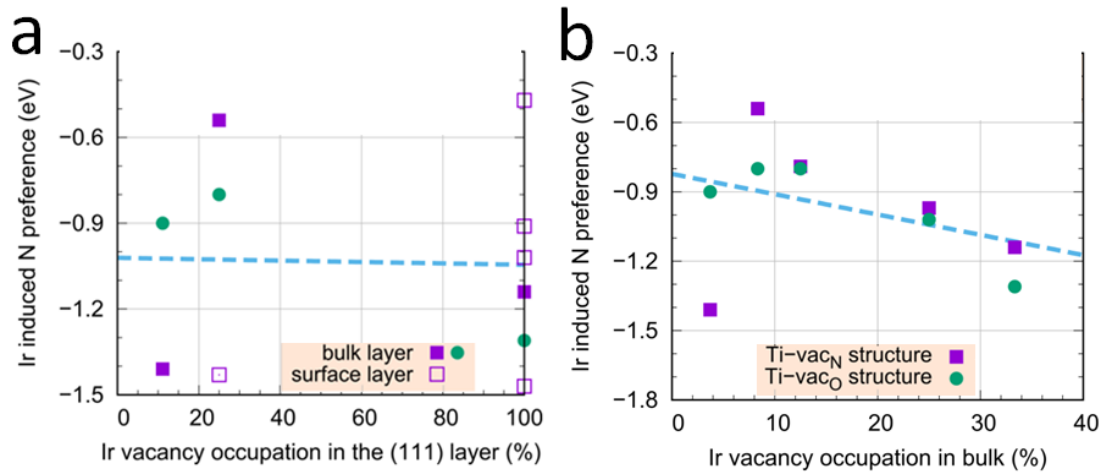

Figure 4.15: Graphs of (Ir-induced N preference) as a function of Ir SA concentration ($\Delta_{1:1}$ of Eq. (3.4)). (a) $\Delta_{1:1}$ as a function of Ir SA concentration in the (111) layer with numerous bulk (solid symbols) and surface (open symbols) TiON-Ir structures considered (green points and purple squares refer to Ti-vac_O and Ti-vac_N structures, respectively). (b) $\Delta_{1:1}$ as a function of bulk Ir SA concentration with numerous bulk TiON-Ir structures considered (both Ti-vac_N and Ti-vac_O type structures are considered, Figure A.12). A 100 % "surface" concentration denotes that all Ti-vacancies are occupied by Ir SAs in a given Ti(111) layer and a 100 % bulk concentration denotes that Ir SAs occupy all Ti-vacancies. The $\Delta_{1:1}$ average is indicated by the blue dashed lines (data points are linearly fitted by the blue lines). The 100 % (111)-layer concentration corresponds to a 33 % bulk concentration for (111)-rotated bulk structures, because Ir atoms are located in only one of the three Ti-layers (TiON(111) consists of A−B−C stacking of Ti-layers).

4.2.3 Big Ir nanoparticles

The same NanoLab platform concept was also used to investigate a TiON-Ir sample with bigger Ir nanoparticles. At first, the TiON-Ir grid was structurally characterized with STEM. STEM images of the TiON-Ir grid at low magnification after the Ir deposition can be found in Figure 4.16e-h. The nanotubular morphology of the TiON support is most visible in Figure 4.16h as the approximately 40 nm circular openings in the bottom left part of the image. Ir nanoparticles can be seen as bright spots and can reach sizes of up to 15 nm. The Ir nanoparticle size is polydisperse (Figure A.13) due to an intentionally selected temperature programme (fast heating, heating rate 100 °C min^{-1}) for the $IrBr_3$ reduction. This synthesis method also causes twin boundaries in the Ir nanoparticles to form more often (Figure 4.16a-d). This is in contrast to the previous Ir nanoparticle deposition method (slow heating, heating rate 2 °C min^{-1}, low temperature, 1 h at 400 °C) where the formed Ir nanoparticles are much smaller and more monodisperse (1 nm – 2 nm diameter) [66]. Such small Ir nanoparticles are too small to observe changes on individual crystal facets, which is why the synthesis method was changed to obtain bigger nanoparticles. A treatment at a higher temperature and a fast heating rate was chosen so that Ir nanoparticles with more defects and with a wider size distribution would form. From trial and error, it was found that the largest Ir nanoparticles form on the edge where the solution droplet dried. Therefore, only half of the grid was dipped in the $IrBr_3$ solution because the middle of the TEM grid is the optimal location for STEM imaging.

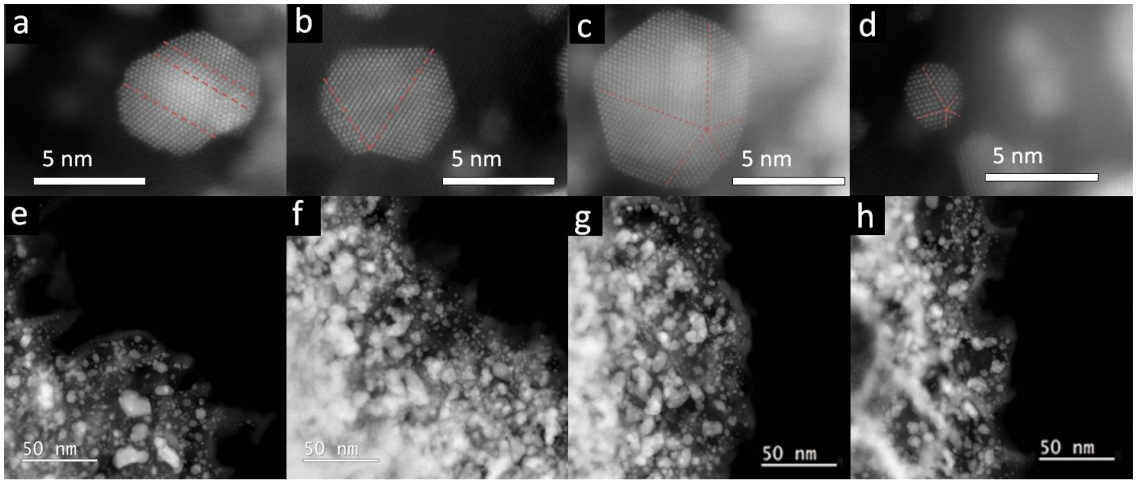

Figure 4.16: STEM-HAADF images of the TiON-Ir sample. (a-d) examples of polysynthetic and cyclic twinning (red dashed lines show twin boundaries) and (e-h) images at low magnification.

Potentiostatic activation of the TiON-Ir sample was performed after the structural analysis. With potentiostatic activation, long-term stationary protocol suitability for the use in MFE for OER studies was evaluated. Additionally, with this step, the Ir nanoparticles and the TiON support were oxidized before the electrochemical activity was evaluated. Simultaneous oxidation events such as Faradaic contributions of Ir nanoparticle and TiON support oxidation at high anodic potentials can cause misinterpretation of the measured OER current [66], [129]. In

Figure 4.17b, activity of the TiON-Ir sample before and after the polarization at 1.6 V for 30 min is shown. Because the exact surface area and mass of Ir are unknown, the current was normalized by the geometric surface area of the TEM grid that was in contact with the electrolyte which is defined by the Teflon housing opening. The measured current after potentiostatic activation was higher which was expected due to the formation of a thin Ir oxide layer with a higher intrinsic activity on the non-activated metallic Ir nanoparticles [97].

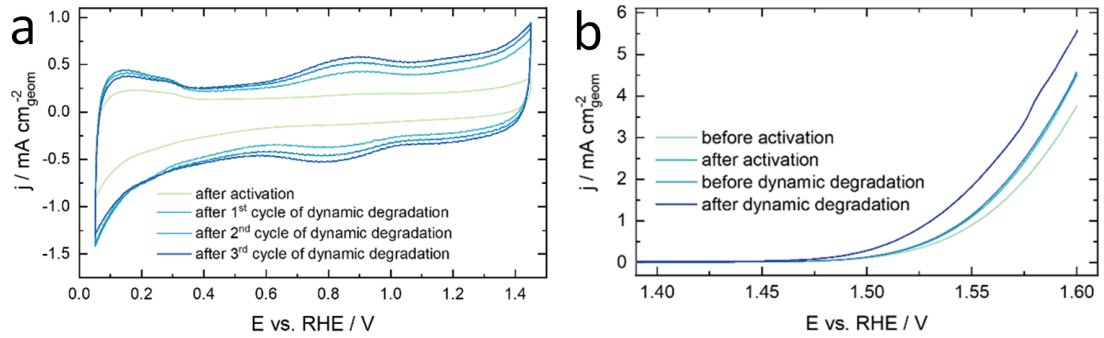

Figure 4.17: Evaluation of different activation protocols. (a) cyclic voltammogram for the evaluation of metallic Ir structural changes during electrochemical degradation and (b) polarization curves for activity evaluation before and after the dynamic degradation protocol and before and after the potentiostatic activation protocol.

During stationary experiments, the problem of bubble accumulation can occur. That is why a dynamic degradation experiment was designed which is similar to protocols used in other research [130], [131].

Cyclic voltammograms in Figure 4.17a are the first clue of structural changes on Ir nanoparticles during the degradation experiment. 20 fast CVs were recorded (0.05 V – 1.45 V) after each dynamic protocol cycle. At least some share of Ir is in a metallic state at the start of the protocol which is indicated by the H_{upd} feature between 0.05 V and 0.35 V [132] characteristic for metallic Ir. The presence of this peak can be seen throughout the experiment, meaning that Ir has a lower tendency for oxidation when supported on the ceramic material. This is in agreement with the study by Bele et al. [63] and Savinova et al. [133]. A characteristic feature for Ir^{3+} to Ir^{4+} transition (broad peak) can be seen at around 0.9 V which indicates that Ir nanoparticles are, at least to some extent, getting oxidized during the dynamic protocol. The heightened electrocatalytic activity of Ir nanoparticles after the dynamic degradation protocol is another indicator of structural changes and is in agreement with other research [134].

Atomic resolution IL-STEM images were taken of five individual Ir nanoparticles which stayed in the zone axis during the three IL-STEM imaging steps and analysed with custom-made image analysis algorithms. The goal was to gain in-depth understanding of the structural changes after the two electrochemical steps. IL-STEM images of two Ir nanoparticles (particles no. 2 and no. 5) are shown in Figure 4.18. They are shown in the as-synthesized state, after activation, and after dynamic degradation. The positions of the atomic columns are depicted in green for each step of the experiment. IL-STEM images of the remaining three nanoparticles (particles no. 1, no. 3, and no. 4) can be seen in Figure A.14.

From a brief literature overview, it can be said that in general, the structure-stability interrelations are still not very well researched. Based on Ir single-crystal work by Özer et al. [135], the surface orientation is very important for the formation of the oxide layer. They showed that Ir (111) planes are less prone to oxidation than the more open Ir (110) planes and the morphology is different depending on on which plane the oxide grows. Scohy et al. [136] came to a similar conclusion. Here, the authors studied both single crystalline and nanostructured surfaces. They found out that the original structure and chemical composition influence the growth of the oxide in the beginning on single crystalline and nanostructured surfaces, but then all of the surfaces gradually transform into a similar phase. BalaKrishnan et al. combined XPS with atom probe tomography to follow the structural transformations of the Ir probe which was needle-shaped [137]. They found out that the nature of the planes plays an important role in the formation of the oxide phase. On the closed (111) Ir planes, the oxide layer growth stopped at 1 nm – 2 nm and on the opened planes, the oxide layer grew to around 10 nm

thickness at 1.55 V after 300 s. Different crystallographic planes can therefore have different catalytic activities and stabilities. Based on that, they suggested that hydrous iridium oxide is limited only to open planes.

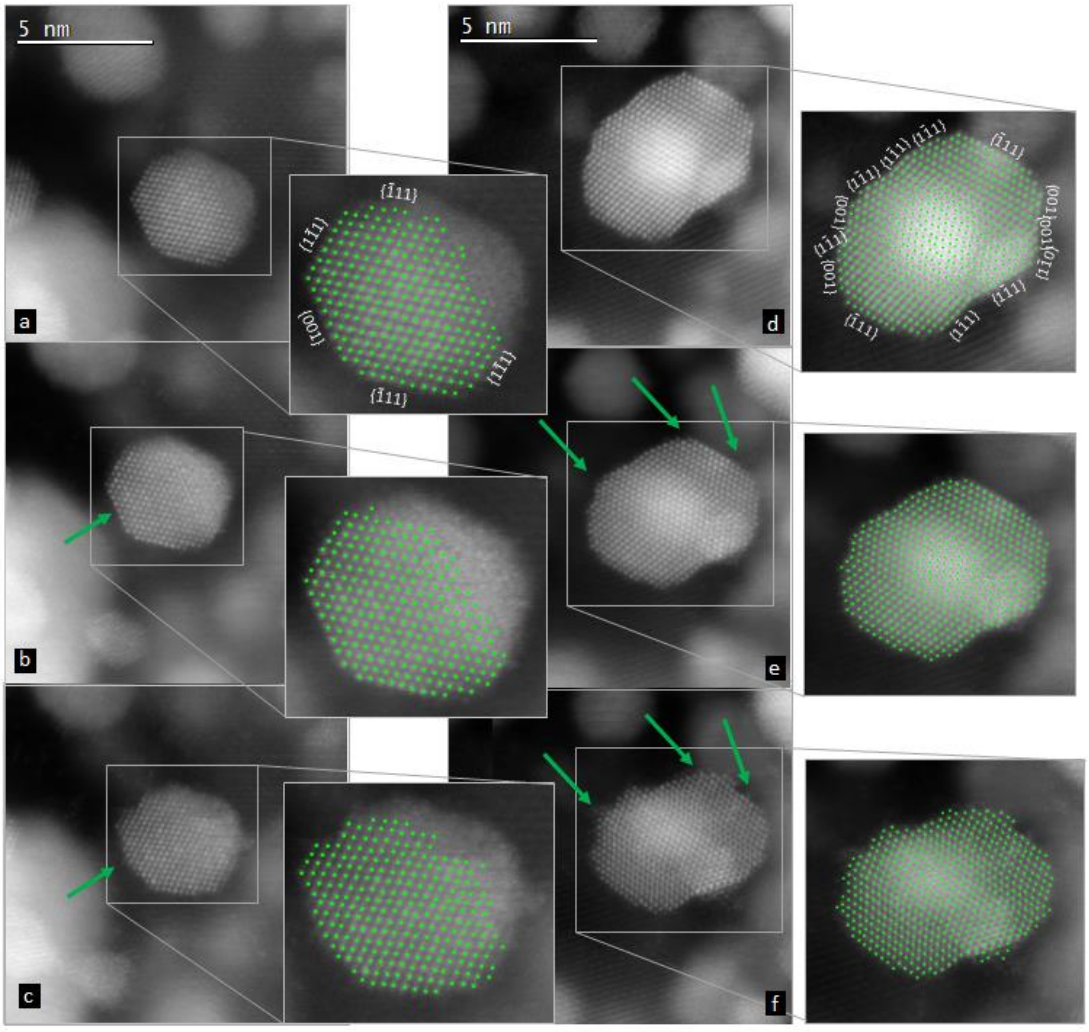

Figure 4.18: IL-STEM images of (a-c) a smaller (nanoparticle no. 2) and (d-f) a larger (nanoparticle no. 5) Ir nanoparticle. (a,d) before electrochemical treatment, (b,e) after potentiostatic activation, and (c,f) after dynamic degradation. The green dots are the positions of atomic columns. Green arrows mark sites where probably amorphous growth occurred after dynamic degradation.

None of the research from literature focused on supported Ir nanostructures which is how this investigation is different. From the five inspected Ir nanoparticles, it can be concluded that potentiostatic activation causes only minor changes. Slow oxidation is the most probable reason for this based on the CVs, but it is also possible that the Ir particles were blocked by gas bubbles to some extent. It is also possible that changes occurred in directions that were not observed because all five Ir nanoparticles were imaged in the same zone axis [110]. The changes in the five Ir nanoparticles are more obvious after dynamic degradation. The predominant degradation type, which was observed in the images, is surface roughening (loss of faceted shape). On the contrary to the research above, this research shows no dependence on surface orientation. The edges of individual facets are more prone to changes than columns in the middle of a well-defined crystal which seemed to be left intact. Some potential amorphous growths were observed mostly on {001} facets and a few also on {111} facets. Although only a few occurrences were found in total, this is in agreement with previous research where {111} planes had less

oxide layer growth [135]–[137]. For a higher certainty, more Ir nanoparticles would have to be analysed or advanced techniques used.

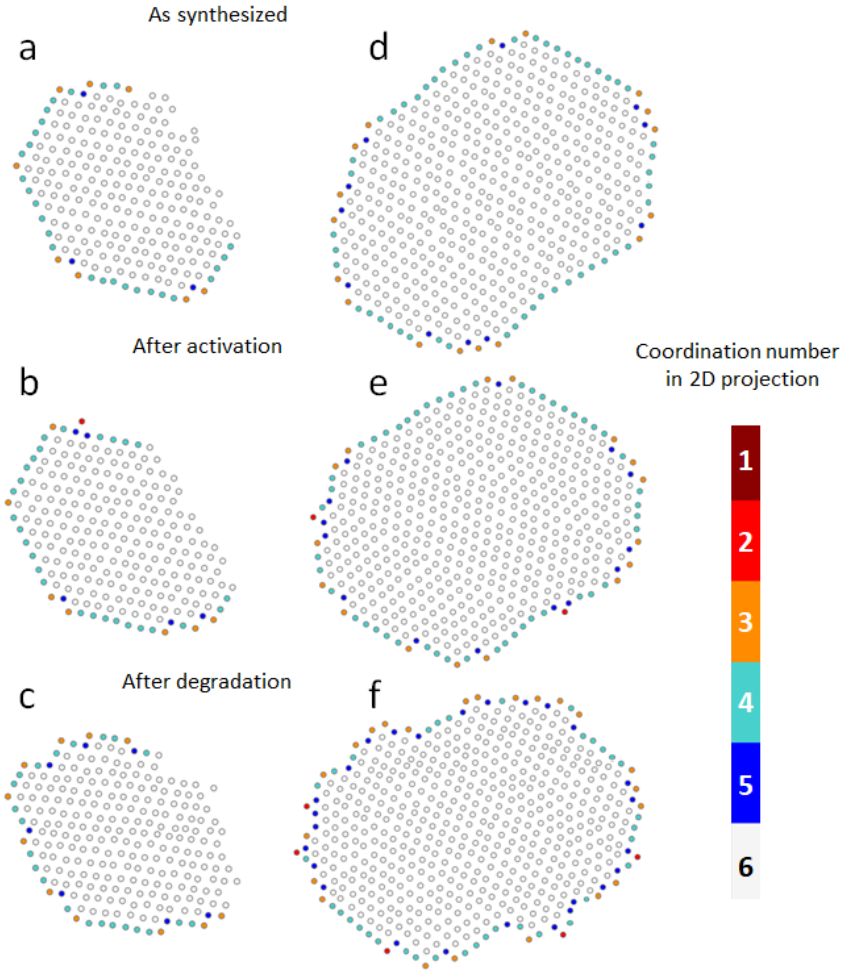

Figure 4.19: Images of the atomic columns with different numbers of nearest neighbours for two Ir nanoparticles. (a-c) smaller (nanoparticle no. 2) and (d-f) larger (nanoparticle no. 5) Ir nanoparticle. (a,d) before electrochemical treatment, (b,e) after potentiostatic activation, and (c,f) after dynamic degradation.

To quantitatively evaluate the surface roughening of Ir nanoparticles, the atomic columns were classified by the number of nearest neighbours. The atomic columns of Ir nanoparticles are colored by the number of nearest neighbours in Figure 4.19 (and in Figure A.15). Each atomic column in the Ir nanoparticle in the [110] zone axis can have 6 nearest neighbours maximum. Atomic columns with 1-5 nearest neighbours are on the surface and atomic columns with 6 nearest neighbours are in the interior. Importantly, some of the Ir nanoparticles are only partially imaged in the zone axis due to twinning (example Figure 4.18a-c). The atomic columns at the twin boundary were excluded from this quantification because the true number of nearest neighbours cannot be known. The number of atomic columns with the same number of nearest neighbours was normalized by the total number of atomic columns for each of the five nanoparticles and for each step of IL-STEM (Figure 4.20).

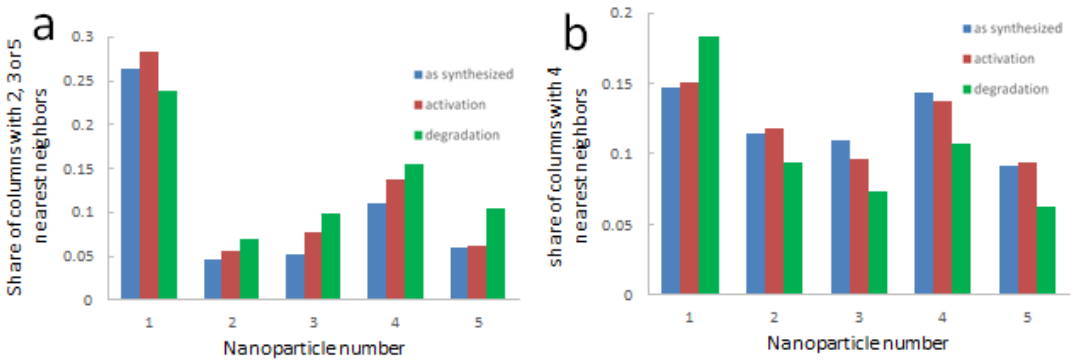

Figure 4.20: Graphs of the share of columns. (a) with 2, 3 or 5 nearest neighbours or (b) with 4 nearest neighbours.

The two nanoparticles in Figure 4.18 are labelled as “nanoparticle no. 2” and as “nanoparticle no. 5” in these graphs. The results were divided into two groups: the share of columns with 2, 3, or 5 nearest neighbours, which quantifies the change in surface roughness, and the share of columns with 4 nearest neighbours, which quantifies the change in loss of faceted shape. No atomic columns had one nearest neighbour. Based on the results, the share of defects (steps, edges, and kinks) increases and the share of facets decreases due to the dynamic degradation protocol. The smallest Ir nanoparticle (nanoparticle no. 1) did not follow this trend. This can be explained by the larger share of surface atomic columns compared to other bigger Ir nanoparticles. The smallest Ir nanoparticle was also reshaped during both electrochemical protocols (Figure A.14a-c) but the reshaping did not increase roughness. A possible explanation for this is that the high share of columns with 2, 3, or 5 nearest neighbours might not be possible to be increased even more with additional movements of the atomic columns. It can be concluded that smaller Ir nanoparticles already have maximum roughness and for Ir nanoparticles above around 3 nm the surface roughness can still be increased due to the dynamic degradation protocol. To reduce the costs of electrocatalysts in PEMWEs, smaller and more stable Ir nanoparticles are more desirable. A recent DFT study has shown that smaller Ir nanoparticles adhere more strongly to the TiON support, a sign of potentially higher stability [66]. Also, smaller Ir nanoparticles tend to dissolve less when two samples with different size distributions are compared (charge was normalized) [67].

As a side note, a possible alternative explanation to surface roughening could also be multiple simultaneous processes (for example dissolution and redeposition) instead of a single process (for example surface diffusion). If individual atoms could be counted (based on atomic column intensity) instead of atomic columns, more insight could be gained into the exact mechanism. This has proven difficult for this TiON-supported sample due to the extra signal coming from the TiON support. Electrochemical liquid cell TEM could give additional insight but atomic resolution would probably be lost.

Based on the oxide features in CVs after the dynamic degradation, the surface of Ir nanoparticles should be at least partially oxidized, but only a few small probable amorphous oxide growths can be seen in the IL -STEM images (Figure 4.18 and Figure A.14, green arrows). This is in agreement with previous research, where it was shown that a strong metal-support interaction (SMSI) stabilizes the Ir nanoparticles compared to Ir nanoparticles with no support [63], [133]. Importantly, the type of support can influence the degree of amorphization [67]. The comparison of two samples of Ir nanoparticles supported on TiON/C showed that the carbon present seemingly enhances the reshaping of Ir nanoparticles. The nature of the sample, the type of experiment, and the technical limitations of STEM imaging prevented coming to conclusions about oxide growth with certainty. The wrinkling of the TEM grid during electrochemical degradation can cause small tilts of the Ir nanoparticles out of the zone axis. In addition, the STEM electron beam and electrochemical degradation can cause local degradation of the TiON support and movements of Ir nanoparticles. The Ir nanoparticles are too small to correct the tilt as there are no Kikuchi lines visible in small nanoparticles (which are necessary to determine the correct tilting direction). This leads to atomic columns being projected in an

elongated way. Additionally, small drifts during STEM imaging are possible and all these effects could hide signs of an oxide layer. The irregular distribution of oxygen in the TiON support also prevents EDXS or EELS to be used to determine the presence of an oxide layer on Ir nanoparticles and long exposure times can cause electron beam damage. It seems that the probable oxide growth does not depend on the orientation which is not in agreement with the other research discussed above. This could be explained by the surface defects present and the nanoparticle size effects. Something similar was concluded in another research study on ORR electrocatalysts made from intermetallic Pt alloys [69].

4.3 Microstructure and Electrical Conductivity of CTiON-NCNFs

4.3.1 Micro- and nanostructure of CTiON-NCNFs

The microstructure of the CTiON-NCNF1 fabric can be observed in SEM images at different magnifications in Figure 4.21. The nanofibres are disordered and intertwined and were produced by electrospinning of a long continuous nanofibre. The average diameter of the CTiON-NCNF1s 130 nm ± 60 nm (mean ± standard deviation) and of the CTiON-NCNF2s is 220 nm ± 30 nm. Figure 4.22a shows the diameter size distribution of both CTiON-NCNF1s and CTiON-NCNF2s. The diameters of 50 nanofibres for the calculation of average diameters and diameter size distributions were measured manually from an SEM image (Figure B.1). Most CTiON-NCNF1s have diameters from 50 nm to 150 nm. Very few CTiON-NCNF1s have a diameter below 50 nm and the number of CTiON-NCNF1s with bigger diameters decreases gradually where diameters 50 nm – 100 nm are the most numerous. Single nanofibre electrical conductivity measurements and TEM analyses require a variety of diameter sizes which a higher diameter dispersion can provide. Most CTiON-NCNF2s have diameters that are from 200 nm to 250 nm with only a few nanofibres with diameters bigger than 250 nm or smaller than 150 nm. To compare the experimental results to the theoretical model, a lower diameter dispersion is more suitable (this will be discussed later on). The CTiON-NCNF1 surface seems uniform and smooth at these magnifications, which is what was also reported in research from other researchers [71]. If we look at higher magnification SEM images of CTiON-NCNF2s (Figure B.15), we can see a rough surface which can be explained by nanopores on the surface of the nanofibres.

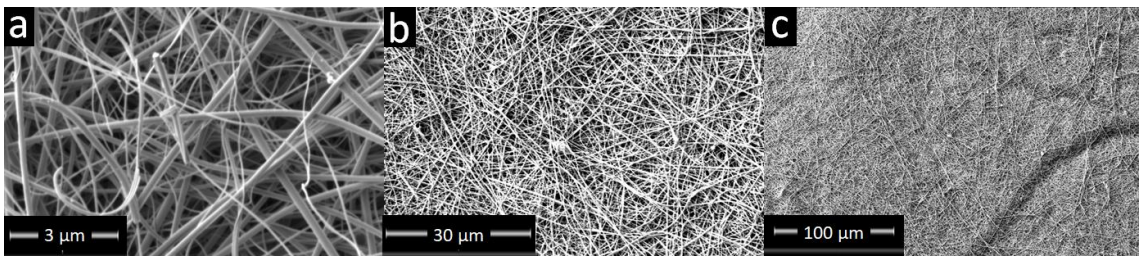

Figure 4.21: SEM images of CTiON-NCNF1 fabric.

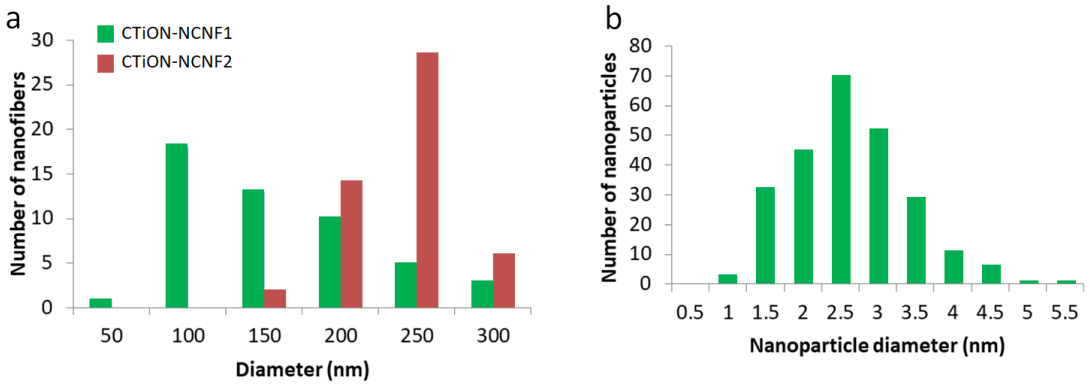

Figure 4.22: Size distribution charts of CTiON-NCNFs. (a) Diameter size distribution of 50 measured CTiON-NCNF1s and CTiON-NCNF2s and (b) particle size distribution of 250 measured nanoparticles of CTiON-NCNF1 sample. Distributions were determined from manual measurements from images in Figure B.1 and Figure B.2 in Appendix.

Looking at CTiON-NCNF1s with STEM (Figure 4.23), it becomes clear that the CTiON-NCNF1s consist of an amorphous carbon matrix in which nanosized TiON particles are embedded, which have an average size of 2.4 nm ± 0.8 nm and the particle size distribution can be observed in Figure 4.22. The measurement of 250 nanoparticles was done manually on a TEM image (Figure B.2) to obtain the average size and the particle size distribution. The diameter of most TiON nanoparticles is between 1 nm and 4 nm. In thicker CTiON-NCNF1s (diameter approximately 300 nm, Figure 4.23a,b,d,e), it can be seen that the TiON nanoparticles are embedded in a lower density matrix. In thinner CTiON-NCNF1s (diameter approximately 50 nm, Figure 4.23g,h), the matrix is less visible. This could be due to the matrix being a lower portion of the nanofibre or due to a higher overlap of TiON nanoparticles in a small diameter nanofibre. What can be seen as dark spots in Figure 4.23d,e,h are nanopores, line profiles (Figure 4.23f,i) show their presence more clearly. The nanopores have an average diameter of 6 nm ± 1 nm (Figure B.14). The intensity of the nanopores is much lower if we compare them to the rest of the CTiON-NCNF1. They are probably formed during nitridation when the organic material is decomposed and escape routes for the gases are formed. A shrinkage of the CTiON-NCNF fabric due to nitridation is estimated to be 40 % (Figure B.3).

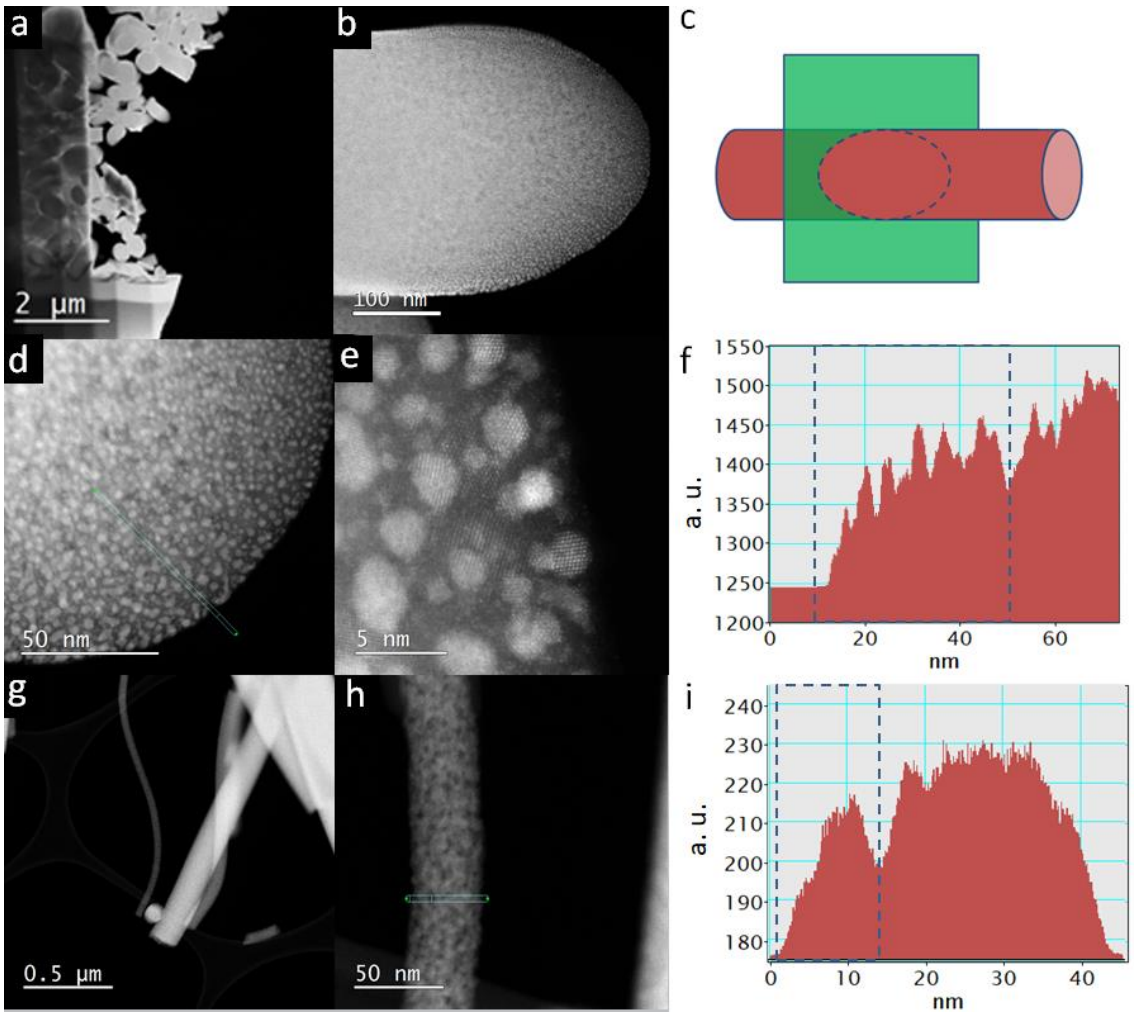

Figure 4.23: Cross-sections and images of CTiON-NCNFs. (a,b,d,e) STEM-HAADF images of lamella of cross-section of CTiON-NCNF1s, (c) scheme of how the CTiON-NCNF1 was cut, (f) line profile of the image d with an (integration width 1.5 nm, marked with green dots and turquoise

lines), (g,h) STEM-HAADF images of CTiON-NCNF1s, and (i) line profile of the image h with an (integration width 3.5 nm, marked with green dots and turquoise lines).

4.3.2 Crystal structure and chemical composition of CTiON-NCNFs

Additionally, the samples were analysed with XRD, selected area electron diffraction (SAED), SEM EDXS, STEM EDXS, EELS, EELS mapping, CHNS elemental analysis, TGA, and Raman which enabled a better characterization of the structure and composition of CTiON-NCNFs. An XRD diffractogram of CTiON-NCNF2 fabric can be observed in Figure 4.24c (red line). The diffractogram confirms the presence of the TiON/TiN face-centred cubic unit cell (FCC) nanocrystalline structure that corresponds to the 1 nm – 4 nm-sized nanoparticles of CTiON-NCNF1, which were observed in the STEM images (Figure 4.23). The Scherrer equation [138] was used to estimate the size of crystallites which gave an average result of 8 nm from the two peaks. A simulation of an XRD diffractogram was also done (Figure 4.24c, green line). The simulated nanoparticle size was 6 nm (4.1987 Å, F m −3 m, $Ti_{0.7}(N_{0.33}O_{0.67})$, the crystal structure was based on the crystal structure from Cambridge Crystallographic Data Centre (CCDC) 908784 / Inorganic Crystal Structure Database (ICSD) 426340 [139] (N and O occupancy changed to $N_{0.365}O_{0.635}$). One possible explanation for the lower nanoparticle sizes in STEM images compared to the estimated nanoparticle sizes from XRD data is that bigger TiON nanoparticles are hiding in the cores of thicker CTiON-NCNFs. The presence of randomly oriented TiON nanocrystallites or nanoparticles in CTiON-NCNF1s is confirmed by the SAED pattern in Figure 4.24b of the CTiON-NCNF1 piece (30 nm diameter) in Figure 4.24a. The formation of TiON is also suggested by the results of Raman spectroscopy (Figure B.7) (details on Raman spectroscopy of CTiON-NCNF1s can be found in Appendix B.2).

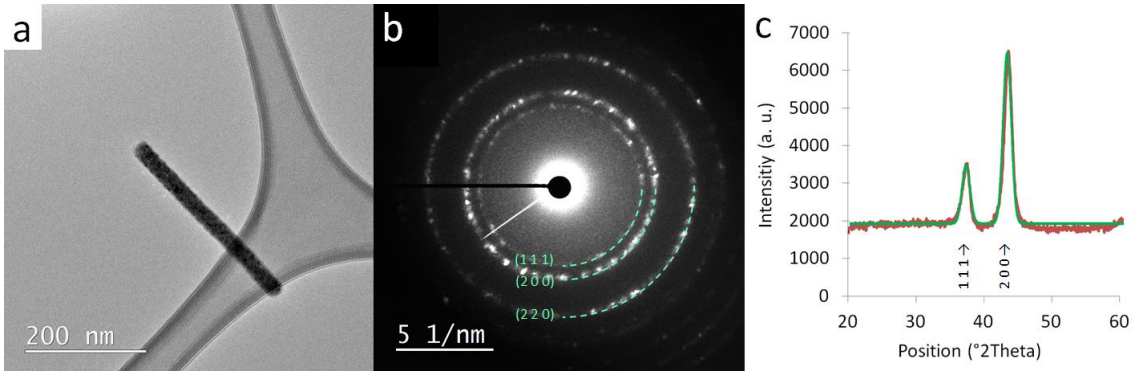

Figure 4.24: SAED pattern and diffractogram of CTiON-NCNF1. (a) TEM image of a CTiON-NCNF1 segment (30 nm diameter), (b) SAED pattern of the CTiON-NCNF1, and (c) XRD diffractogram of the CTiON-NCNF2 fabric (red) and a simulated XRD diffractogram of TiON nanoparticles (green, 6 nm, based on the CCDC 908784 / ICSD 426340, N and O occupancy changed from N330 O670 to N365 O635).

The presence of carbon at around 10 at. % or 5 wt. % can be seen from the SEM EDXS spectrum of the CTiON-NCNF1 fabric in Figure B.16d. CHNS and TGA analysis of CTiON-NCNF1 fabric (details for CHNS and TGA analysis can be found in Appendix B.1) as well as STEM EDXS spectrum of CTiON-NCNF1 in Figure 4.23 confirm the amount of carbon. The lower density matrix in which the TiON nanoparticles are embedded is probably carbon. This can be seen in the STEM image of the CTiON-NCNF1 cross-section in Figure 4.23g,h. The Raman spectroscopy results of the CTiON-NCNF1 fabric independently confirm the presence of carbon in the samples (Figure B.7).

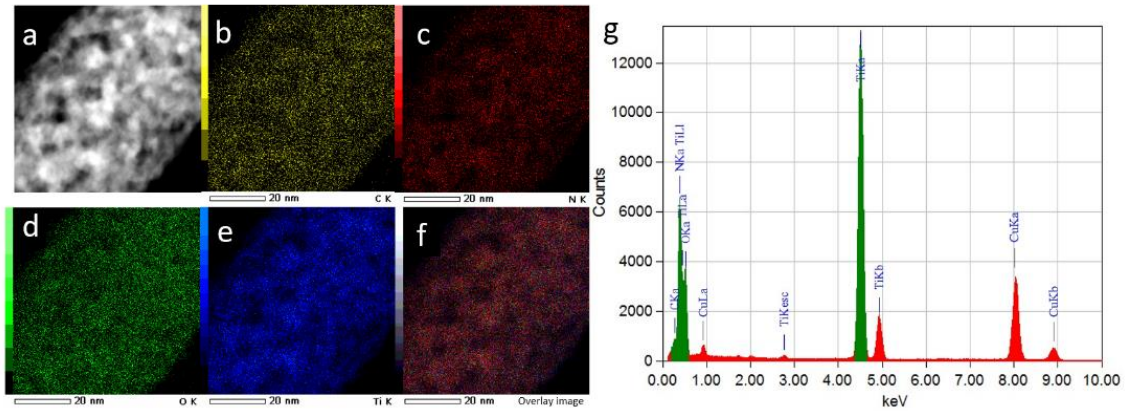

Figure 4.25: STEM EDXS analysis of TiON nanofibres. (a) STEM-HAADF image of the CTiON-NCNF1 location for STEM EDXS analysis, (b) C elemental mapping image, (c) N elemental mapping image, (d) O elemental mapping image, (e) Ti elemental mapping image, (f) overlay image of images c, d, and e, and (g) STEM EDXS spectrum of the CTiON-NCNF1.

The N/O ratio calculation from SEM EDXS data for the CTiON-NCNF1 fabric is 1.67 which is comparable to the N/O ratio of 1.65 calculated from the CHNS and TGA analysis of the CTiON-NCNF1 fabric. The average N/O ratio was also calculated from several CTiON-NCNF1s based on the STEM EDXS measurements and the N/O ratio is 1 ± 0.2. The automatic quantification of the STEM EDXS programme was compared to a simulation of the STEM EDXS spectrum (Figure B.8) and they are very similar (a detailed explanation about the STEM EDXS simulation can be found in Appendix B.3). The average N/O ratio was also calculated from EELS measurements of several CTiON-NCNF1s and the value is 0.6 ± 0.05 (for a detailed explanation of N/O ratio determination with EELS see Appendix B.4). These two methods were expected to bring different results because STEM EDXS and EELS measure the local N/O ratio of individual CTiON-NCNF1s with a diameter of approximately 50 nm or less while the CHNS and TGA and SEM EDXS analyses measure the bulk N/O ratio of a big portion of the CTiON-NCNF fabric.

SEM EDXS spectra of CTiON-NCNF1 and CTiON-NCNF2 fabric can be compared in Figure B.16c,d. Slight differences in composition of CTiON-NCNF1 and CTiON-NCNF2 fabric could not be avoided due to the goal to fabricate samples with different diameter distributions. This was required for us to additionally analyse the samples with other techniques. Table 4.3 shows the comparison of compositions of CTiON-NCNF1 and CTiON-NCNF2 fabric.

Table 4.3: Composition of samples CTiON-NCNF1 and CTiON-NCNF2. The source of composition information were SEM EDXS spectra in Figure B.16.

Sample	Atomic %		Weight %		N/O Ratio	n(C):n(Ti)	m(C):m(TiON)
CTiON-NCNF1	C	12.7	C	6.0	1.67	0.36	0.15
	Ti	33.8	Ti	63.2			
	O	20.0	O	12.5			
	N	33.4	N	18.3			
CTiON-NCNF2	C	7.6	C	3.4	1.13	0.21	0.035
	Ti	36.8	Ti	65.6			
	O	26.1	O	15.6			
	N	29.5	N	15.4			

EELS mapping that was done on an individual CTiON-NCNF1 can be seen in Figure 4.26d,e. From the mapping image, it is clear that there is a thin layer of lower N/O ratio in the thinner parts and on the surface of the CTiON-NCNF1. The line profiles in Figure 4.26c,f show this even more clearly. In Figure 4.26c, the O (green) line is inferior to the N (red) line throughout the core of the CTiON-NCNF1 and only surpasses the N line in pores and on the outermost parts (5 nm –

surface of the nanofibre) where the CTiON-NCNF1 is thinner. The N/O ratio in Figure 4.26f is similarly lower in nanopores and decreases quickly on the surface.

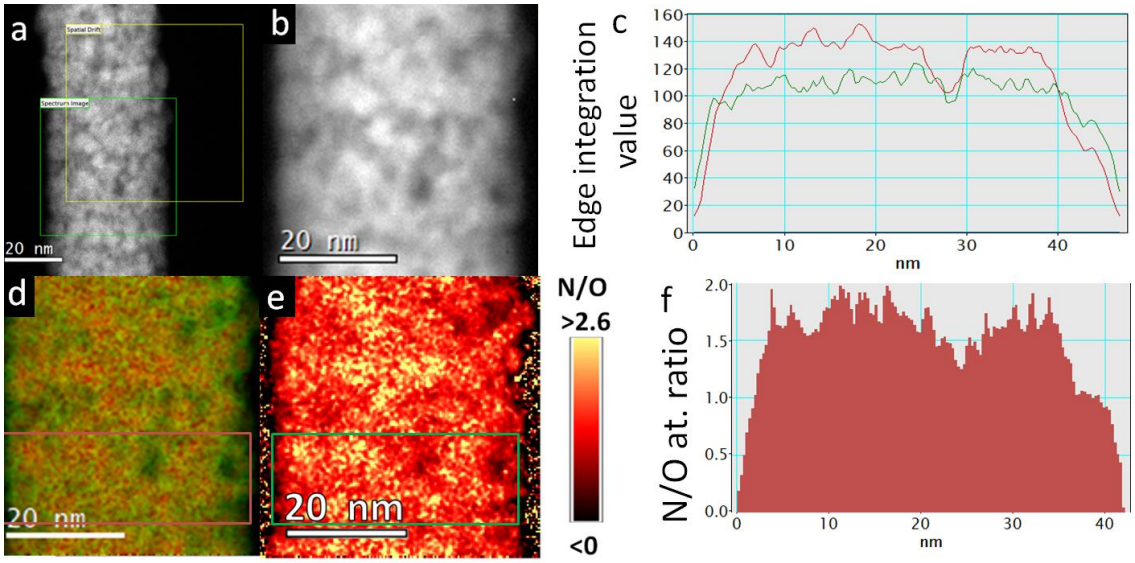

Figure 4.26: EELS mapping of a CTiON-NCNF1. (a) STEM-HAADF image of the spatial drift monitoring (in yellow) and the chosen location for EELS mapping (in green), (b) the EELS mapping mapped area (where each pixel in the image is a whole EELS spectrum), (c) a line profile of the image d (location is marked with a red square on image d) with an integrated width 15 nm, where the green line represents the O edge and the red line represents N edge integration value, (d) EELS mapping image of extracted O and N edge spectra where green represents more oxygen content and red represents more nitrogen content (the image is smoothed), (e) N/O ratio in every pixel as a colour distribution (the image is smoothed), (f) a line profile of the image e (location is marked with a green square on image e) with an integrated width of 15 nm.

Similarly, EELS mapping of the cross-section of a 300 nm thick single CTiON-NCNF1 (Figure 4.27) shows also this phenomenon. The inner parts of the CTiON-NCNF1 have a higher N/O ratio which decreases towards a thin strip of the surface (Figure 4.27d,e). This can be more clearly seen in the line profiles in Figure 4.27c,f. The N line in Figure 4.27c is lower than the O line only at the surface and the N/O ratio in Figure 4.27f is steadily decreasing from approximately 2 in the core to 0.5 towards the surface. The thickness of the cross-section of the CTiON-NCNF1 (300 nm thickness) is decreasing from the centre to the surface (left to right side of each profile). The nanofibre was cut under an angle, which guarantees that at least some area of the cross-section is thin enough to be analysed with EELS and EELS mapping. The N/O ratio quickly starts diverging (very high negative and positive values) in Figure 4.27d when approaching the inner part of the CTiON-NCNF1. The background in EELS measurements is increasing due to the increasing thickness which causes that the O and N edges are hidden in the background in the inner part of the CTiON-NCNF1 and the N/O ratio calculation makes less and less sense. The same thing can also be seen in the line profile in Figure 4.27e, where the edge integration value of both O and N is decreasing and overlapping more and more the closer we get to the core. Because of this, the line profile of the N/O ratio in Figure 4.27f was restricted to only 65 nm from the surface.

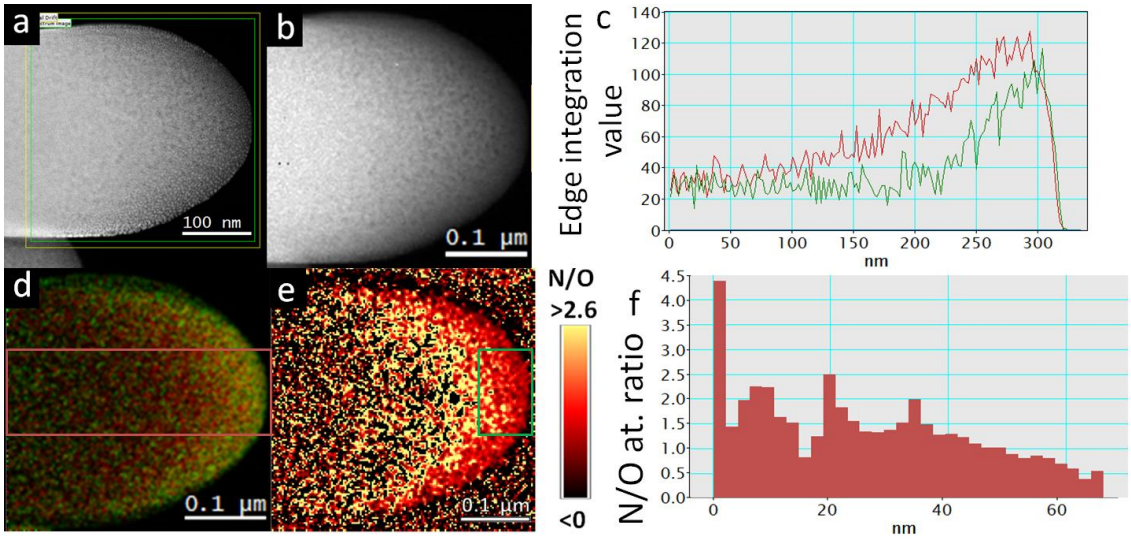

Figure 4.27: EELS mapping of a cross-section of a CTiON-NCNF1. (a) STEM-HAADF image of the spatial drift monitoring (in yellow) and the chosen location for EELS mapping (in green), (b) the EELS mapping mapped area (where each pixel in the image is a whole EELS spectrum), (c) a line profile of the image d (location is marked with a red square on image d) with an integrated width of 100 nm, where the green line represents the O edge and the red line represents N edge integration value, (d) EELS mapping image of extracted O and N edge spectra where green represents more oxygen content and red represents more nitrogen content (the image is smoothed), (e) N/O ratio in every pixel as a colour distribution (the image is smoothed), (f) a line profile of the image e (location is marked with a green square on image e) with an integrated width of 100 nm.

The surface of nano-scale TiON and TiN can already be oxidized at room temperature [76]. N atoms in TiON or TiN are exchanged for O atoms at the start and TiO_2 can also be formed in the later stages of oxidation [72]. The higher amounts of O on the surface in our study are in agreement with this and the different results of N/O ratio from EELS and SEM EDXS are also explained with this. A lower N/O ratio (relatively more oxygen) is to be expected with EELS due to the limitation of EELS that it needs to be carried out on thin regions of the sample where the surface represents a higher percentage of the analysed material in such a case. Information from the core of thicker samples can be obtained with SEM EDXS measurements where less O is present, which leads to higher N/O ratios.

4.3.3 Electrical conductivity and electrochemical measurements

Individual CTiON-NCNF1s were put on Protochips electrical chips. The nanofibre was connected with Ga ions deposited platinum with FIB-SEM to the contacts on the chip in a four-probe electric circuit configuration, as can be seen in Figure 4.28. To measure the electrical resistance of the nanofibre, the four-probe measurement was done with the Protochips Aduro™ system using electrical chips inside the TEM vacuum. The electron beam was blocked to avoid interaction with the electrical conductivity measurement. Four CTiON-NCNF1s were measured successfully in total. Their electrical resistivity was calculated based on the calculated and measured physical quantities using the following formula:

$$\rho = R\frac{A}{l} = R\frac{\pi r^2}{l}, \tag{4.1}$$

where R is resistance, ρ is resistivity, l is the nanofibre length, and r is the average nanofibre radius. The assumption is that the shape of CTiON-NCNF1s is cylindrical. Along the CTiON-NCNF1, many manual diameter measurements were made to then calculate the average nanofibre radius. The calculations and measurements are listed in Table 4.4. From the four measured CTiON-NCNF1s, an average resistivity of 1.0 mΩm ± 0.5 mΩm (average conductivity

1.2 kS/m ± 0.5 kS/m) was obtained. The average conductivity is in the range of carbon nanofibres [140]–[142], for which TiON-based nanofibres are seen as an alternative. Similar TiON nanofibres from literature can have an electrical conductivity in the same order [72] or up to approximately 30× higher [72], and in some cases, even approximately 3000× higher [76]. The higher conductivity of TiON nanofibres from literature [72], [76] can be explained by the fact that, in our case, TiON nanoparticles are immersed in a carbon matrix. Similarly, compared to our CTiON-NCNF1s, TiN nanofibres can have approximately 5× higher and bulk TiN approximately 400× higher electrical conductivity [81]. A typical current–voltage (I–V) curve can be seen in Figure 4.29 and shows that the CTiON-NCNF1s exhibit ohmic behaviour.

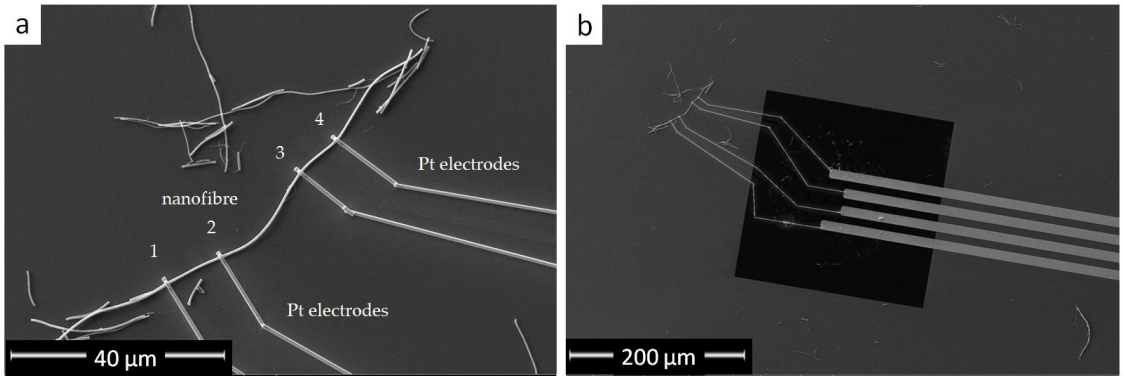

Figure 4.28: SEM image of a single CTiON-NCNF1 with four-probe contact on a Protochips electrical chip. (a) shows the arrangement of Pt contacts with the nanofibre up close and (b) shows how the Pt contacts connect the nanofibre to the chips' contacts from afar.

Table 4.4: Table of dimensions and electrical properties of single CTiON-NCNF1s.

Fibre sample No.	Nanofibre length l (µm)	Average nanofibre radius r (nm)	Resistance R (kΩ)	Conductivity (kS/m)	Resistivity Ro (mΩm)
1	35.2	230	120	1.8	0.6
2	22.3	207	100	1.7	0.6
3	18.0	230	130	0.8	1.2
4	44.5	170	872	0.6	1.8
Average				1.2 ± 0.5	1.0 ± 0.5

Additionally, sheet conductivity of CTiON-NCNF2 fabric was measured. The sheet conductivity of a typical sample was measured to be approximately 1.6 mS. Knowing that the thickness was 30 µm (Figure B.5a), bulk resistivity was calculated to be 19 mΩm (bulk conductivity 0.053 kS/m). The bulk conductivity is 4× lower than a comparable fabric from another research study [74]. The characteristic length between nanofibre contacts can be determined, which can be used as an estimate of mesh density, by comparing the resistivity of a single CTiON-NCNF1 and bulk resistivity of the CTiON-NCNF2 fabric. This can be achieved by using a theoretical model where the nanostructure of the CTiON-NCNF2 fabric sample is approximated as a mesh of resistors. The robustness of the contacts between the nanofibres can be confirmed from SEM images (Figure B.4a,b) and they are therefore not expected to present a significant portion of the total resistance. To generalize this theoretical model, it is changed from a regular cubic lattice to a random anisotropic mesh of resistors. A cubic lattice of resistors has a specific resistivity equal to $\rho_{bulk} = Rl$ in all directions, where *l* and *R* are length and resistance of each lattice segment. To obtain an estimate of the characteristic length between nanofibre contacts, both values are expressed in terms of resistivity of material ρ and nanowire cross-section A, using the following equation:

$$l = \sqrt{\frac{A\rho_{bulk}}{\rho}} \tag{4.2}$$

In the case of our samples, it is approximately 1.0 µm. This is in agreement with the characteristic length between the nanofibre contacts which can be estimated from the SEM images (1 µm – 3 µm, Figure B.5b). As a side note, the samples are truly anisotropic only in the plane of the nanofibre fabric.

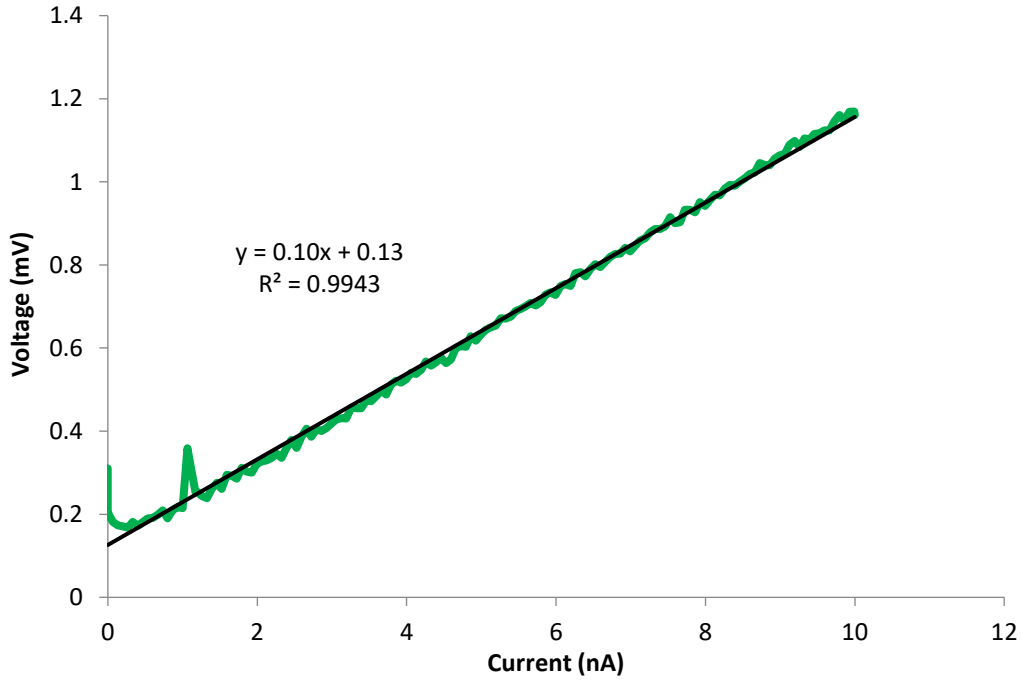

Figure 4.29: An example of an I-V curve of single CTiON-NCNF1 which exhibits ohmic-type conductivity.

To determine specific capacitance of CTiON-NCNF2 fabric, EIS and charge–discharge curves at different current densities (4 Ag^{-1} – 60 Ag^{-1}) were used, as shown in Figure 4.30. The methods used to determine specific capacitance were found in the literature [143], [144]. A higher efficiency at higher currents is indicated by coulombic efficiencies for the charge–discharge curves (93 % at 60 Ag^{-}1 and 73 % at 4 Ag^{-1}). The measured capacitance**s** from the CV(458 Fg^{-1}), charge–discharge (708 Fg^{-1}), and EIS (1300 Fg^{-1}) are equivalent if compared to the best performing Ti-based materials in the literature [145]. The high capacitance of the CTiON-NCNF2 fabric is most likely due to the combination of (a) the high electrical conductivity of CTiON-NCNF2s and (b) the high surface area which comes from its morphology. The CTiON-NCNF2 fabric seems like a promising material in the supercapacitor field.

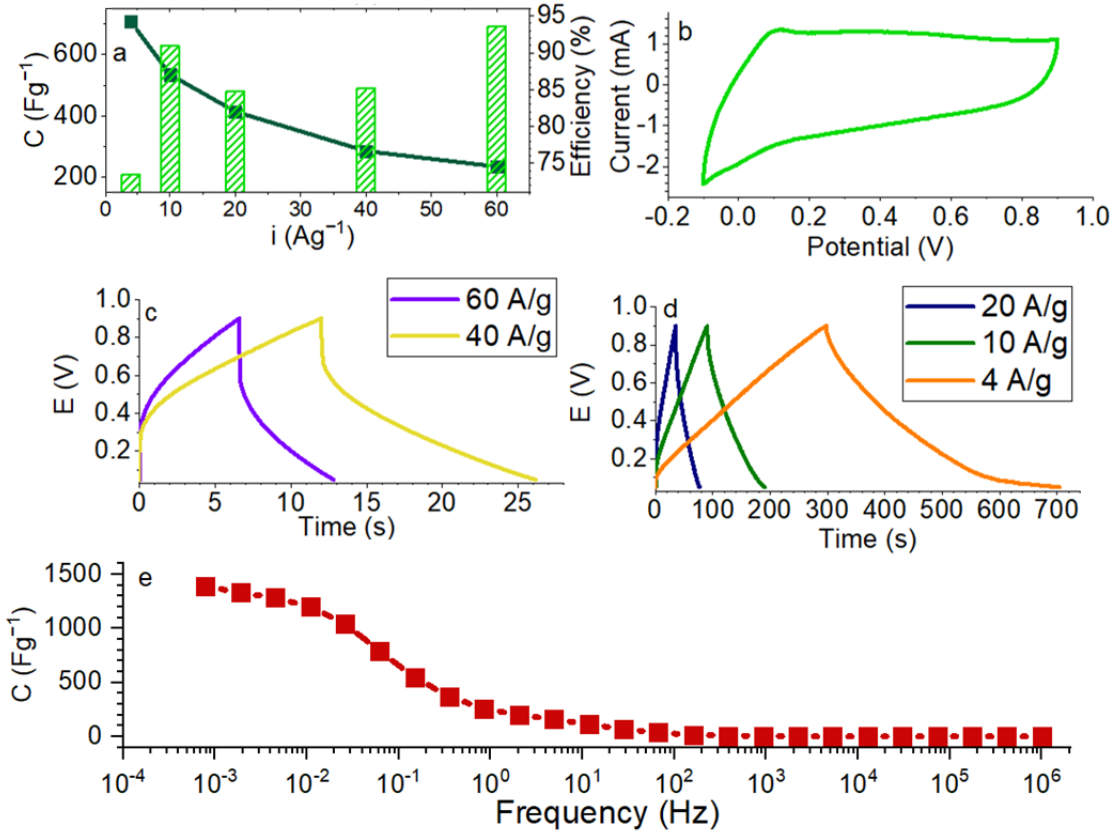

Figure 4.30: Graphs of electrochemical characterization of CTiON-NCNF2 fabric. (a) coulombic efficiency and specific capacitances from charge–discharge curves of CTiON-NCNF2 fabric for different current densities, (b) CV at a scan rate of 10 mVs^{-1}, (c) charge–discharge curves of CTiON-NCNF2 fabric at 60 Ag^{-1} and 40 Ag^{-1}, from 0.05 V to 0.9 V, (d) charge–discharge curves of CTiON-NCNF2 fabric at 20 Ag^{-1}, 10 Ag^{-1}, and 4 Ag^{-1}, from 0.05 V to 0.9 V, and (e) specific capacitance of CTiON-NCNF2 fabric which was determined with EIS.

4.3.4 Estimation of electrical conductivity of TiON nanofibres

Estimation of the electrical conductivity of CTiON-NCNF1s is also possible from the material characterization data. We can assume that the CTiON-NCNF1s are a three-phase composite material that is made from TiON nanoparticles and nanopores embedded in a C matrix. C and TiON phases are both electrically conductive and it is assumed that the nanopores have an electrical conductivity of 0 kS/m. We can determine the type of C in the C matrix based on the shape of the C edge in EELS data (Figure B.12) [146]. The C matrix consists of amorphous C because there is no white line visible at around 285 eV which is characteristic for σ bonds [146]. The electrical conductivity of amorphous C is in the range of 1.4 kS/m − 10 kS/m (0.1 mΩm − 0.7 mΩm) [147]. The electrical conductivity of TiON is highly dependent on the N/O ratio. The measured N/O ratios from EELS, STEM EDXS, TGA and CHNS, and SEM EDXS range from 0.6 to 1.7. Additionally, the electrical conductivities reported in the literature vary widely for these N/O ratios due to different synthesis methods [72], [88], [148]–[151]. This means that the electrical conductivity range for TiON nanoparticles is between 0.07 kS/m and 50 kS/m. If the electrical conductivities of the different phases vary a lot (in our case TiON nanoparticles, amorphous C matrix, and nanopores), a simple rule of mixture (ROM) cannot be used effectively. A more suitable theoretical model for this material is the effective medium theory (EMT) for a three-phase composite (a C matrix with spherical inclusions of nanopores and TiON) in 3D [152].

$$f_1 \frac{\sigma_1 - \sigma_{eff}}{\sigma_1 + 2\sigma_{eff}} + f_2 \frac{\sigma_2 - \sigma_{eff}}{\sigma_2 + 2\sigma_{eff}} + f_3 \frac{\sigma_3 - \sigma_{eff}}{\sigma_3 + 2\sigma_{eff}} = 0, \tag{4.3}$$

where σ_i is the electrical conductivity of phase i, f_i is the volume fraction of phase i, and σ_{eff} is the effective conductivity of the composite. The volume fraction was calculated to be 50 vol. % for C matrix, 40 vol. % for the TiON nanoparticles, and 10 vol. % for nanopores based on the images in Figure B.13 and Figure B.14. The assumption was made that the surface area fraction from the 2D image equals to the 3D volume fraction. By solving equation, an effective conductivity range from 0.45 kS/m to 19 kS/m is obtained for our CTiON-NCNF1s. As a side note, the measured single CTiON-NCNF1s (Table 4.4) have electrical conductivities within this range.

Chapter 5

Conclusions

A series of TiON nanopowder samples was analysed with different analytical methods such as STEM EDXS, SEM EDXS, EELS, TGA + CHNS, XPS, XRD, and Raman to determine the N/O ratio and evaluate the appropriateness of these analytical methods for N/O ratio determination in further samples.

A new experimental platform (NanoLab) was developed to offer new pathways to understanding the relation between composition and structure and electrochemical activity and stability of TiON-Ir support – electrocatalyst system on the atomic level. Anodized, calcined, and nitridated Ti TEM grids were used as a support for nano-sized Ir electrocatalyst. The TiON-Ir samples were then electrochemically treated and analysed with the MFE setup. After each synthesis step and electrochemical treatment, the samples were analysed with IL-TEM and ex-situ techniques.

NanoLab was used on TiON and TiON-Ir samples in order to compare their behaviour during OER. IL-EELS measurements showed a thick TiO_2 layer forming on the bare TiON support sample during electrochemical degradation estimated to be 3 nm thick and a much thinner TiO_2 layer on the TiON-Ir sample estimated to be 10-times thinner, 0.3 nm, showing higher stability. IL-STEM images showed the presence of single Ir atoms after electrochemical perturbation. The single Ir atoms were found in Ti vacancies on the surface of the TiON support and were therefore thought to be the reason for the increased stability. DFT calculations showed that single Ir atoms play an important role in TiON support stability as well as Ir nanoparticles.

NanoLab was also used for the analysis of bigger Ir nanoparticles supported on TiON to understand structural changes of Ir nanoparticles during OER. In combination with in-house developed algorithms for structural analysis from atomic resolution images, it was revealed that surface roughening is the predominant degradation mechanism and confirmed that the tendency of Ir nanoparticles supported on TiON to oxidize was low.

Additionally, CTiON-NCNFs were synthesized with electrospinning and nitridation as a potential support for electrocatalysts. The 50 nm – 150 nm thick nanofibres consist of an amorphous carbon matrix with approximately 2.4 nm-sized TiON nanoparticles embedded within. Their electrical conductivity was measured and they were characterized with different analytical methods. The electrical conductivity was 1.2 kS/m ± 0.5 kS/m, which is better than similar amorphous carbon nanofibres. The electrical conductivity was also estimated from characterization results and compared to experimental results. The experimental results are within the estimated range (0.45 kS/m – 19 kS/m).

Appendix A

IL-TEM of TiON and TiON-Ir

A.1 NanoLab

A.1.1 Optical microscope analysis

Figure A.1 shows the change in the TEM grid sample appearance on the macroscopic level due to the experimental steps. After anodic oxidation (Figure A.1a), the TEM grid has a metallic silver colour with a small amount of white due to the metallic Ti TEM grid and the white TiO_2. After annealing in air at 450 °C (Figure A.1b), the TEM grid has a bluish purple colour, which is typical for thin oxide films (oxygen vacancies are colour centres). After nitridation (Figure A.1c), the TEM grid has a black and gold colour which is due to the formation of TiON (TiON gold in colour in thin films and black in nanopowders due to the high electrical conductivity). The TEM grid also becomes more fragile due to N atoms diffusing into the Ti metal (breakage can be seen in Figure A.1d-f). Ir NPs deposition and both electrochemical degradations do not affect the colour of the TEM grid noticeably.

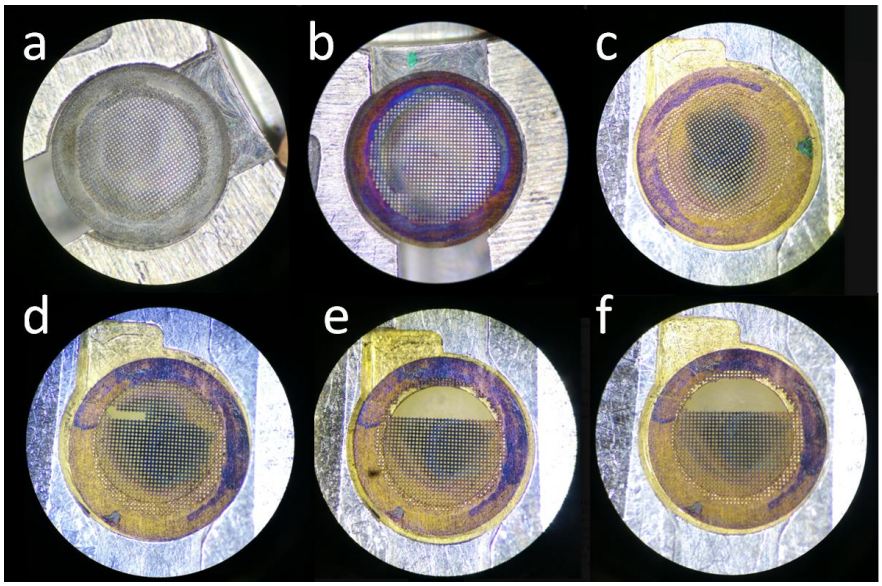

Figure A.1: Optical microscope images of the TEM grid at every characterization step: (a) anodization, (b) annealing, (c) nitridation, (d) reduction of Ir salts, (e) SW-DP, and (f) CV-DP.

A.1.2 Additional SEM and TEM analysis of the TEM grid floating electrode and detailed analysis of Ir nanoparticles

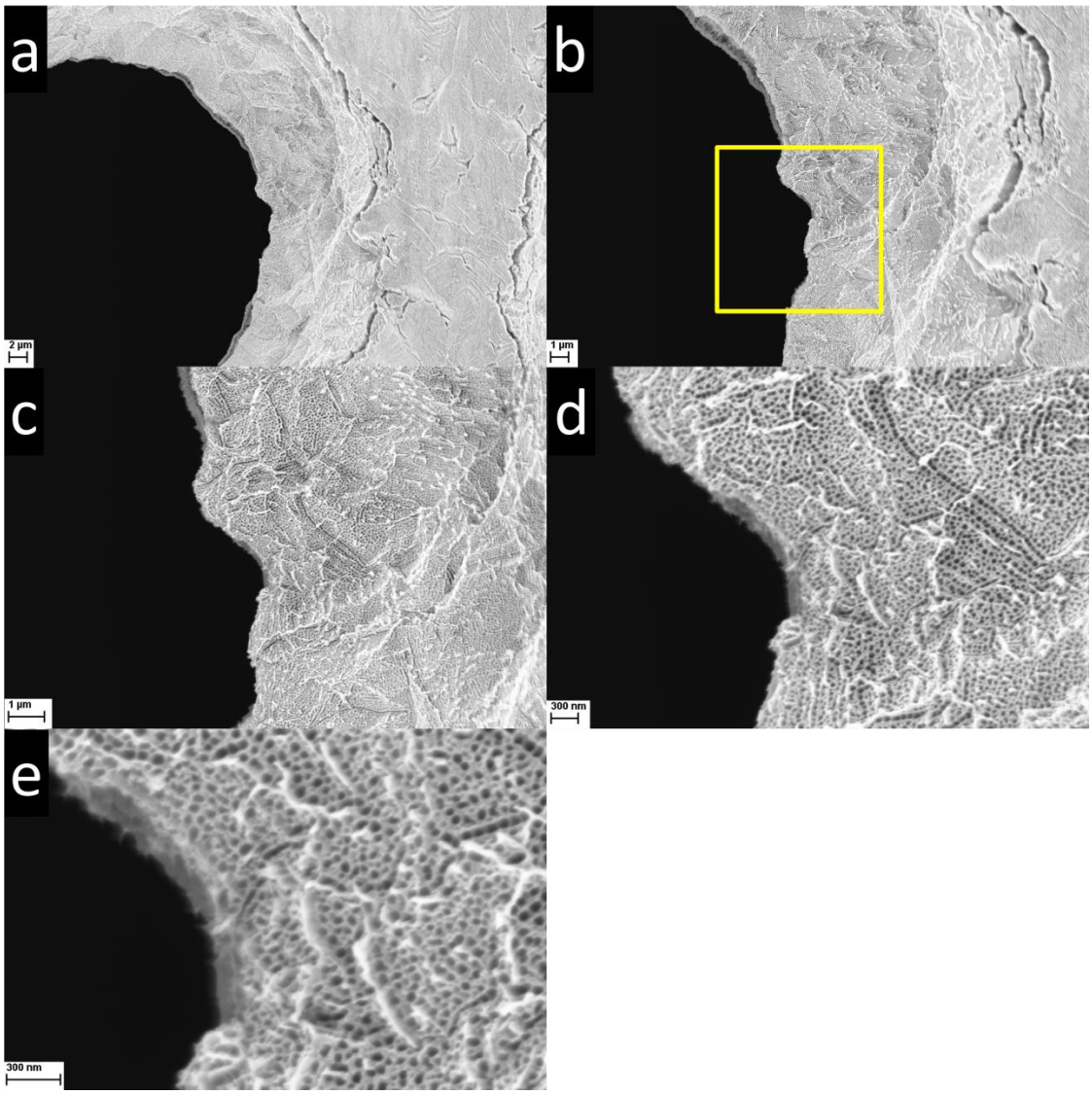

Figure A.2: SEM images of the TEM grid floating electrode sample after anodic oxidation at different magnifications. The yellow square in image b indicates the same location in SEM and TEM images (Figure A.3a).

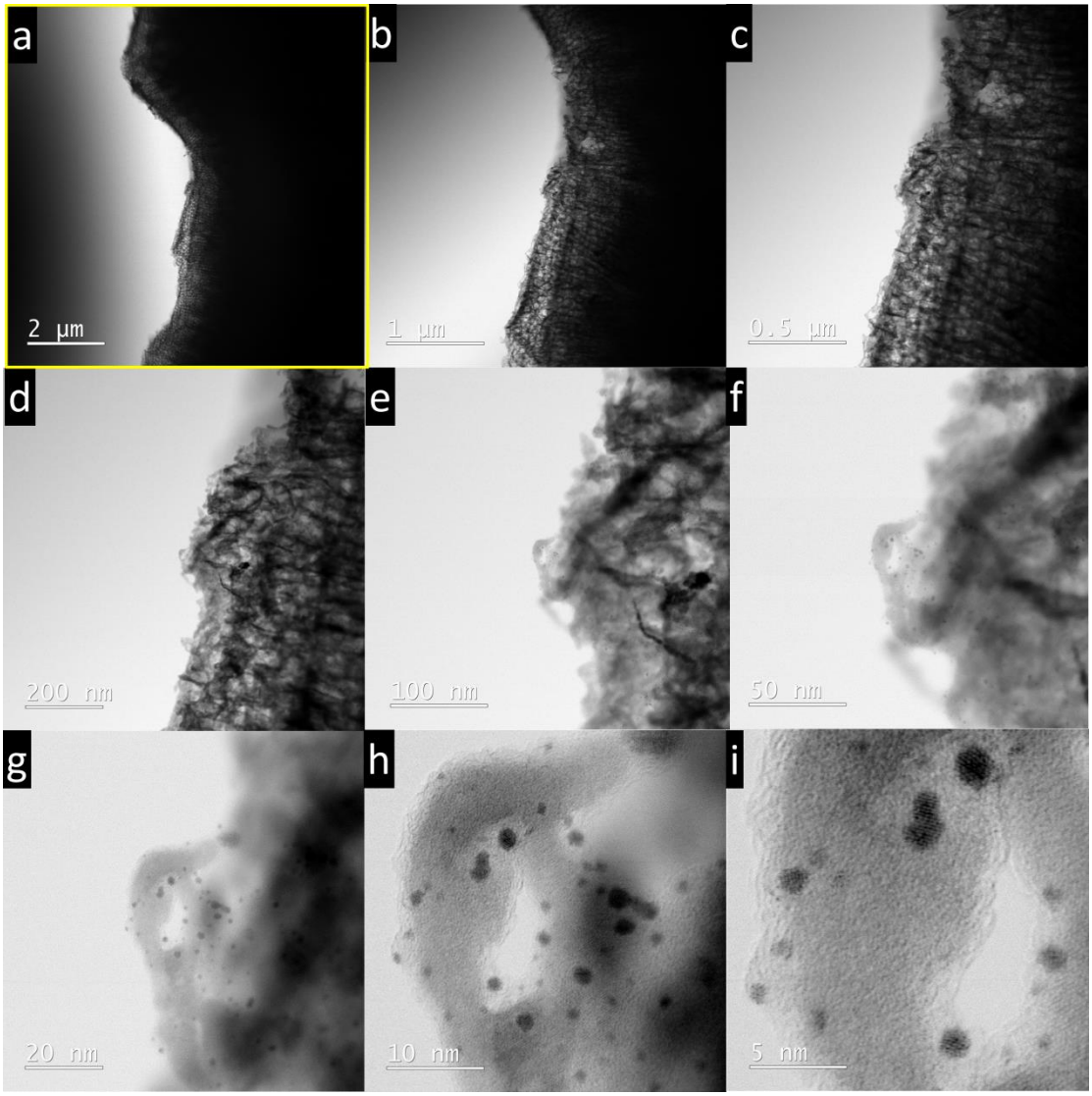

Figure A.3: BF-STEM images of the TiON-Ir TEM grid floating electrode sample at different magnifications. The yellow square in image a indicates the same location in SEM and TEM images (Figure A.2 b).

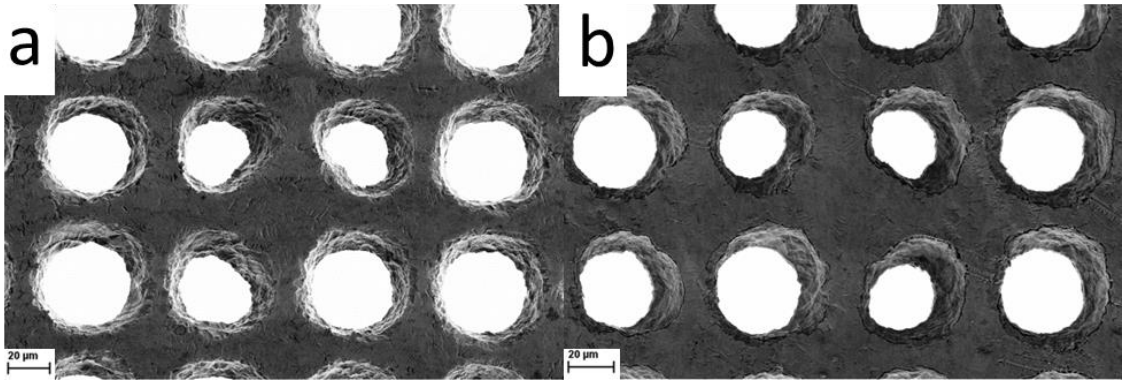

Figure A.4: SEM images of the TEM grid (a) before and (b) after anodic oxidation.

Table A.1: Table showing changes in particle size, circularity, and nearest neighbour distance for the TiON-Ir sample before and after SW-DP and after CV-DP. The information for statistics was obtained from IL-STEM-HAADF images.

TiON-Ir system statistics	TiON-Ir before degradation	TiON-Ir after SW-DP	TiON-Ir after CV-DP
Particle size (nm^2)	1.53 ± 1.43	1.53 ± 1.38	1.55 ± 1.56
Circularity	0.84 ± 0.08	0.83 ± 0.09	0.82 ± 0.09
Nearest neighbour distance (nm)	0.43 ± 0.23	0.44 ± 0.24	0.45 ± 0.24
Number of particles	1709	1698	1573

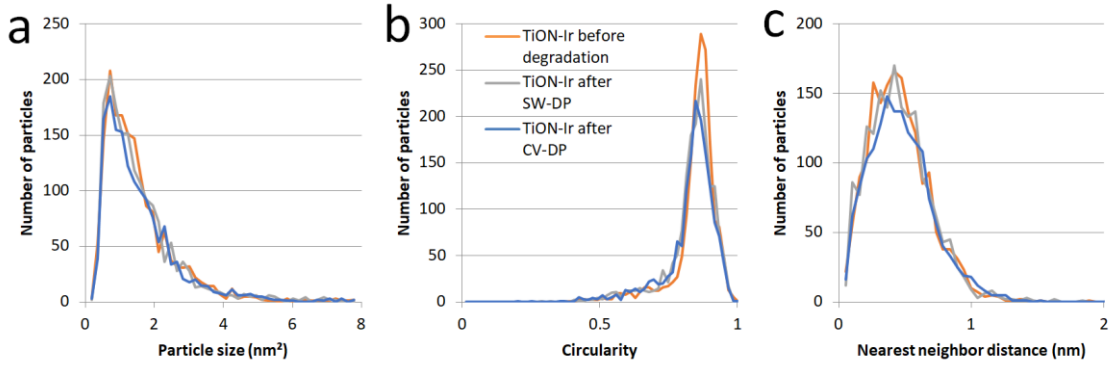

Figure A.5: Graphs of distributions of the TiON-Ir sample. (a) particle size distribution, (b) circularity, and (c) nearest neighbour distance of Ir nanoparticles before and after SW-DP and after CV-DP.

A.1.3 XPS analysis

The Ti TEM grid sample was analysed with XPS after annealing, oxidation, nitridation, Ir deposition, and electrochemical tests (SW-DP and CV-DP). Information about the oxidation states of Ir and surface composition was calculated from the XPS results. XPS spectra showed the presence of C 1s, N 1s, O 1s, Si 2p, K 2p, Ti 2p, Ti 3s, and Ir 4f peaks. Surface composition of N, O, Ti, and Ir, N/O ratio, and the share of Ir(0) and Ir(4+) after each experimental step for the TEM grid sample were obtained and shown in Table A.2. Elements C, Si, and K were detected, but they were not considered for quantification.

The surface composition of the TEM grid sample after anodization and annealing in air resembles the TiO_3 composition (Table A.2). Surface contamination may explain the excess of O. The high surface sensitivity of the XPS method can also detect surface contaminants such as O_2, N_2, and CO_2. After nitridation, N gets incorporated into the TiO_2 structure resulting in 23 at. % of N, 51 at. % of O, and 26 at. % of Ti (approximately $Ti_1N_1O_2$), which means that approximately half of the O atoms on the near surface of the TiO_2 structure got replaced with N atoms. After SW-DP and CV-DP, the concentration of O increased, and N concentration decreased. This is indicative of O atoms replacing N atoms during the catalytic reaction.

After Ir deposition, approximately 1.6 at. % of Ir are present on the surface of the TEM grid sample. This decreases to approximately 1.5 at. % after SW-DP and to approximately 1.0 at. % after CV-DP. The share of Ir(0) is decreasing and the share of Ir(4+) is increasing after each electrochemical step (Table A.2).

Table A.2: XPS surface composition in at. % for the TiON-Ir TEM grid sample, N/O ratio, and share of different Ir(0) and Ir(4+) oxidation states in total Ir. The relative error of elemental composition is estimated to be ± 10 %.

Sample stage	N (at. %)	O (at. %)	Ti (at. %)	Ir (at. %)	N/O ratio	Ir(0) of total Ir	Ir(4+) of total Ir
Anodization	2	72.7	25.3	0	0.03	0	0
Annealing	1.3	74.1	24.6	0	0.02	0	0
Nitridation	22.7	51.2	26.1	0.0	0.44	0.0	0.0
Ir deposition	17.7	59.5	21.3	1.6	0.30	0.6	0.4
SW-DP	13.1	68.8	16.6	1.5	0.19	0.3	0.7
CV-DP	14.1	67.5	17.4	1.0	0.21	0.0	1.0

A.1.4 Table of elemental composition of samples analysed with EELS and EDXS

Table A.3: Table of elemental composition of the sample at each experiment stage analysed with EELS and EDXS. EELS results are the average ± standard deviation of 20 measurements at different locations. EDXS measurements were done in two locations. The relative error of elemental composition from EDXS is estimated to be ± 10 % for N and O and ± 10 % for Ti and Ir.

Analysis method	Sample stage	N (at.%)	O (at.%)	Ti (at.%)	Ir (at.%)	N/O
EELS	nitridation	22 ± 1	34 ± 2	44 ± 1		0.67 ± 0.06
	Ir deposition	20 ± 1	38 ± 2	42 ± 1		0.53 ± 0.07
	SW-DP	18 ± 2	40 ± 4	42 ± 2		0.46 ± 0.09
	CV-DP	17 ± 2	42 ± 4	41 ± 2		0.42 ± 0.07
EDXS location 1	nitridation	15.73	1.47	82.28		10.7
	Ir deposition	1.23	0.35	96.14	0.69	3.5
	SW-DP	1.24	0.50	96.48	0.76	2.5
	CV-DP	1.07	0.59	96.42	0.82	1.8
EDXS location 2	nitridation	15.83	1.18	82.37		13.4
	Ir deposition	1.27	0.36	95.61	0.89	3.5
	SW-DP	1.17	0.53	95.99	1.04	2.2
	CV-DP	0.95	0.6	96.11	1.05	1.6

A.1.5 XRD analysis of white powder formed during reduction of Ir salts

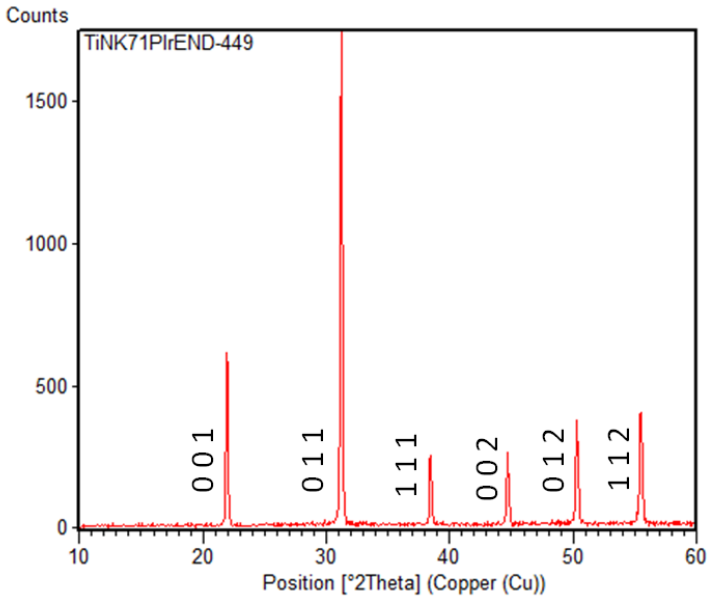

Figure A.6: XRD spectrum of NH_4Br by-product. This was obtained from a similar sample in powder form.

A.1.6 IL-EELS mapping

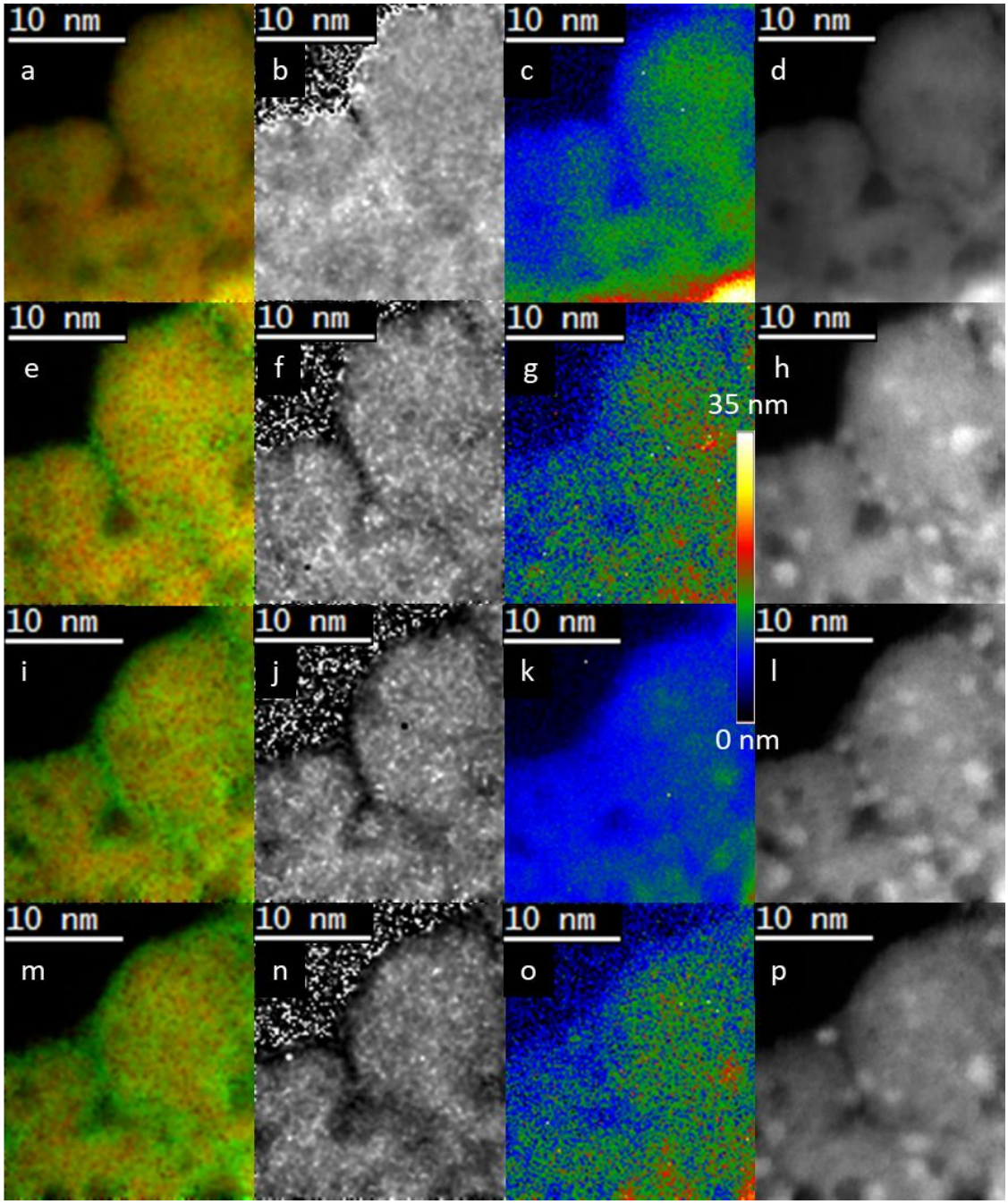

Figure A.7: IL-EELS mapping images of TEM grid sample. (a-d) nitridation, (e-h) Ir NPs deposition, (i-l) SW-DP, and (m-p) CV-DP. (a,e,i,m) colour images (red is nitrogen and green is oxygen), (b,f,j,n) N/O ratio images (brighter pixel means higher N/O ratio), (c,g,k,o) thickness calculated from EELS, and (d,h,l,p) EELS high loss maps (every pixel is the integral of the EELS spectrum in that location).

A.2 Single Ir Atoms

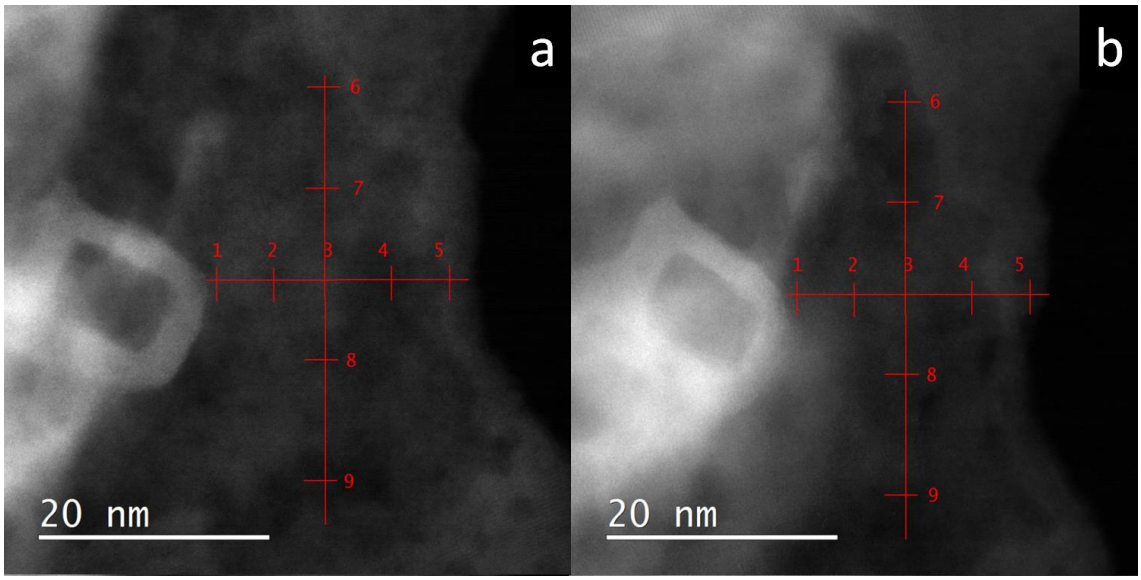

Figure A.8: IL-EELS measurement locations for the TiON sample. (a) before electrochemical degradation and (b) after electrochemical degradation. Each red cross is the location of one EELS measurement.

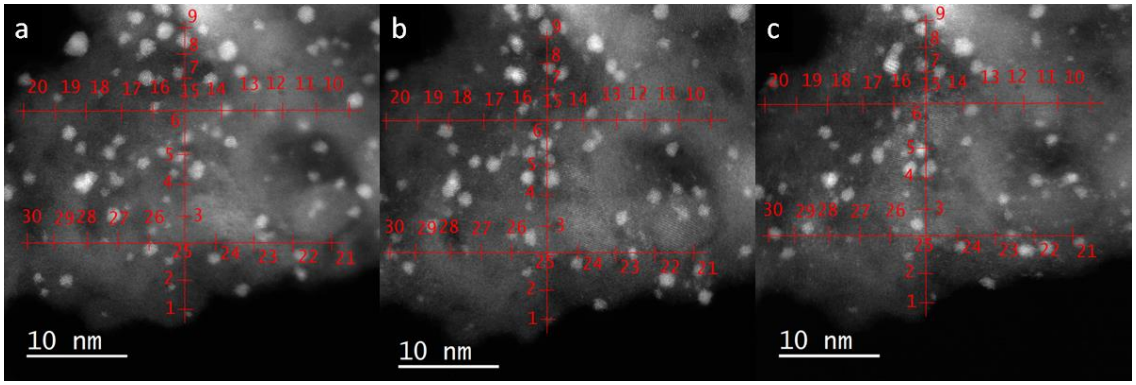

Figure A.9: IL-EELS measurement locations for the TiON-Ir sample. (a) Before electrochemical degradation, (b) after SW-DP, and (c) after CV-DP. Each red cross is the location of one EELS measurement.

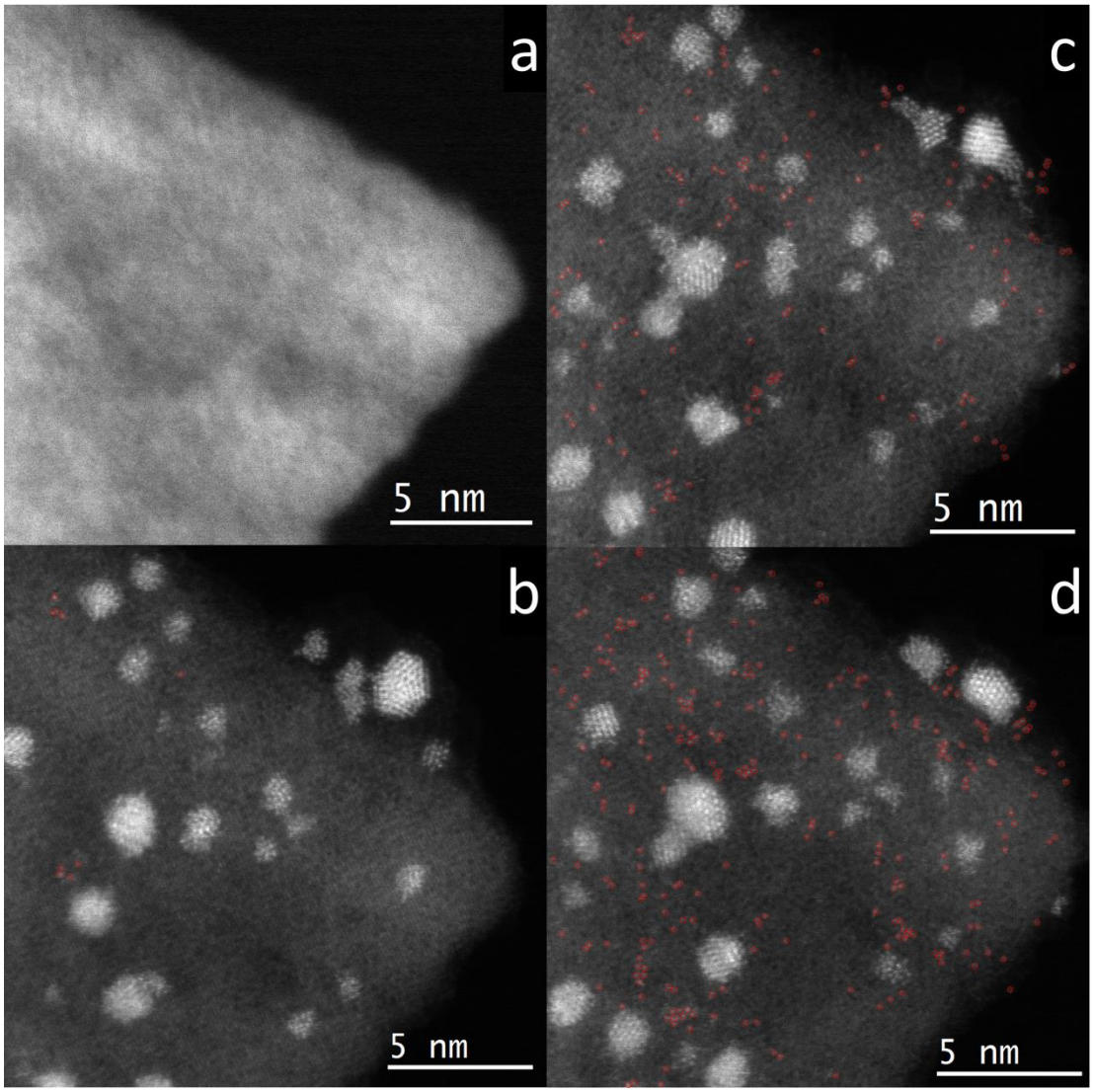

Figure A.10: STEM-HAADF images of TiON-Ir sample after (a) nitridation, (b) addition of Ir, (c) SW-DP, and (d) CV-DP. The counted Ir-SAs are circled in red.

A.2.1 Estimation of TiO_2 layer thickness after degradation of TiON and TiON-Ir

Linear regression extrapolation can be used to estimate the thickness of the formed TiO_2 layer on the bare TiON support TEM grid sample after degradation. The extrapolation of the equation (Figure 4.11 after degradation equation) to (N/O ratio)=0 results in a thickness of thk(TiO_2)=2.8 nm. Because the R^2 values are less than 0.5 (Figure 4.12b,c), this method cannot be used to estimate the thickness of the formed TiO_2 layer for the TiON-Ir TEM grid sample after SW-DP and CV-DP.

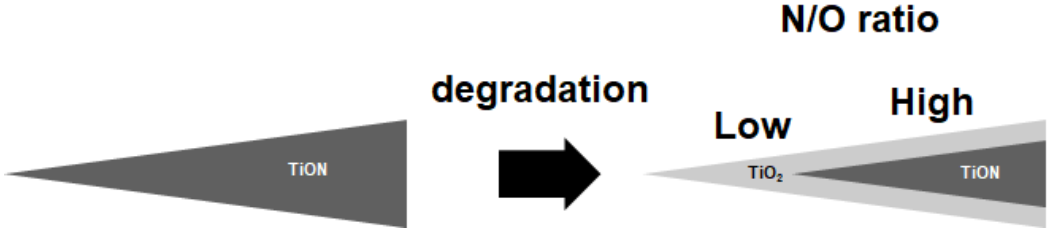

Figure A.11: Scheme of the change of the TiON support due to electrochemical degradation. For the purpose of TiO_2 layer thickness estimation, the average N/O ratio of the dark gray area after

electrochemical degradation is assumed to be the same as the average N/O ratio of the dark gray area before electrochemical degradation.

An alternative way of TiO_2 layer thickness is needed so that the thicknesses of the TiON-Ir and TiON TEM grid samples can be compared to each other. For this, it can be assumed that the two average N/O ratios of TiON and TiON core (before and after electrochemical degradation, respectively) are the same (Figure A.11). Next, the thickness of the TiO_2 layer after electrochemical degradation, which results in the same N/O ratio as in every data point in the graph in Figure 4.11 (after degradation data points), needs to be found out.

$$N/O\ ratio\ before\ degradation = (N/O)_b = \frac{n(N)_b}{n(O)_b} \tag{A.1}$$

$$N/O\ ratio\ after\ degradation = (N/O)_a = \frac{n(N)_a}{n(O)_a} \tag{A.2}$$

$$(N/O)_a = \frac{n(N)_a}{n(O)_a} = \frac{n(N)_b}{n(O)_b + n(O)_{TiO_2}} \tag{A.3}$$

$n(O)_{TiO_2}$ is expressed from Equation (A.3) to get

$$n(O)_{TiO_2} = \frac{n(N)_b - n(O)_b(N/O)_a}{(N/O)_a} \tag{A.4}$$

The molar fraction of Ti and O coming from TiO_2 in the layer after degradation is calculated

$$x(Ti+O)_{TiO_2} = \frac{n(O)_{TiO_2} + n(Ti)_{TiO_2}}{n(N)_b + n(O)_b + n(Ti)_b + n(O)_{TiO_2} + n(Ti)_{TiO_2}} \tag{A.5}$$

It can be assumed that the TiO_2 layer has the following Ti and O ratio

$$n(Ti)_{TiO_2} = \frac{1}{2} n(O)_{TiO_2} \tag{A.6}$$

$$x(Ti+O)_{TiO_2} = \frac{\frac{3}{2} n(O)_{TiO_2}}{n(N)_b + n(O)_b + n(Ti)_b + \frac{3}{2} n(O)_{TiO_2}} \tag{A.7}$$

It can be assumed that the layer thickness of TiO_2 is on both sides of the support the same. From that, the TiO_2 thickness can be calculated as

$$thk(TiO_2)_a = \frac{thk(whole)_a x(Ti+O)_{TiO_2}}{2} \tag{A.8}$$

From this, the average thickness of the TiO_2 layer for the TiON sample can be estimated to be 3.0 nm ± 0.4 nm. All data points in the graph in Figure 4.11 (after degradation data points) are used to calculate the average thickness and standard deviation. The linear regression extrapolation for TiO_2 layer thickness estimation of the bare TiON support TEM grid sample is within the standard deviation of this method (2.8 nm) which gives confidence in the usability of this method. If the same estimation method is used for the TiON-Ir TEM grid sample, an estimated average TiO_2 layer thickness of 0.3 nm ± 0.3 nm after SW-DP and 0.0 nm ± 0.6 nm

after CV-DP can be obtained. A ten times higher stability of the TiON support due to the presence of Ir can be assumed due to the ten-fold difference (10 ± 3) between the estimated TiO_2 layer thickness for TiON-Ir and TiON sample.

A.2.2 Density functional theory simulations

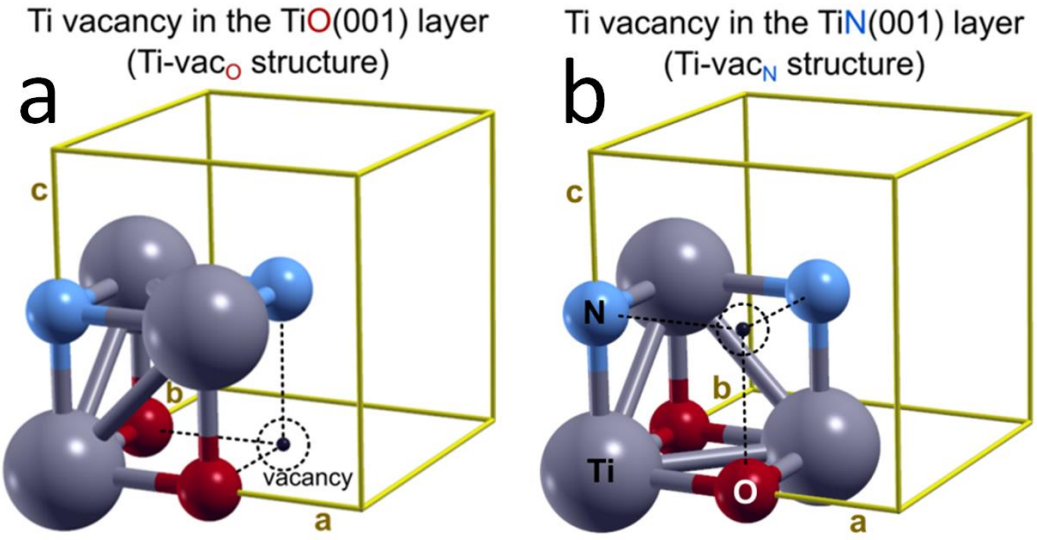

Figure A.12: TiON bulk cubic unit cells which contain 2 N ions, 2 O ions, 3 Ti ions, and 1 Ti-vacancy. The bulk structure of TiON consists of two interpenetrating fcc latices of O/N anions and Ti cations (25 % Ti positions are vacancies) which are shifted by half a Bravais lattice vector relative to each other. The location of the Ti-vacancy can be (a) in the TiO(001) or (b) in the TiN(001) layer. These two structures are named Ti-vac$_O$ and Ti-vac$_N$, respectively.

A.3 Big Ir Nanoparticles

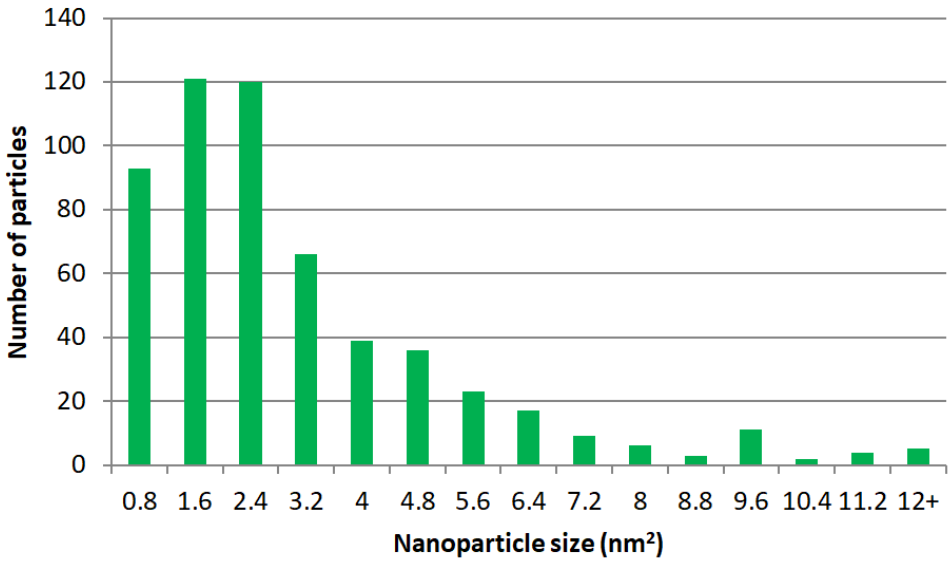

Figure A.13: Graph of particle size distribution of Ir nanoparticles. The particle size distribution was calculated from 555 nanoparticles from HAADF-STEM images.

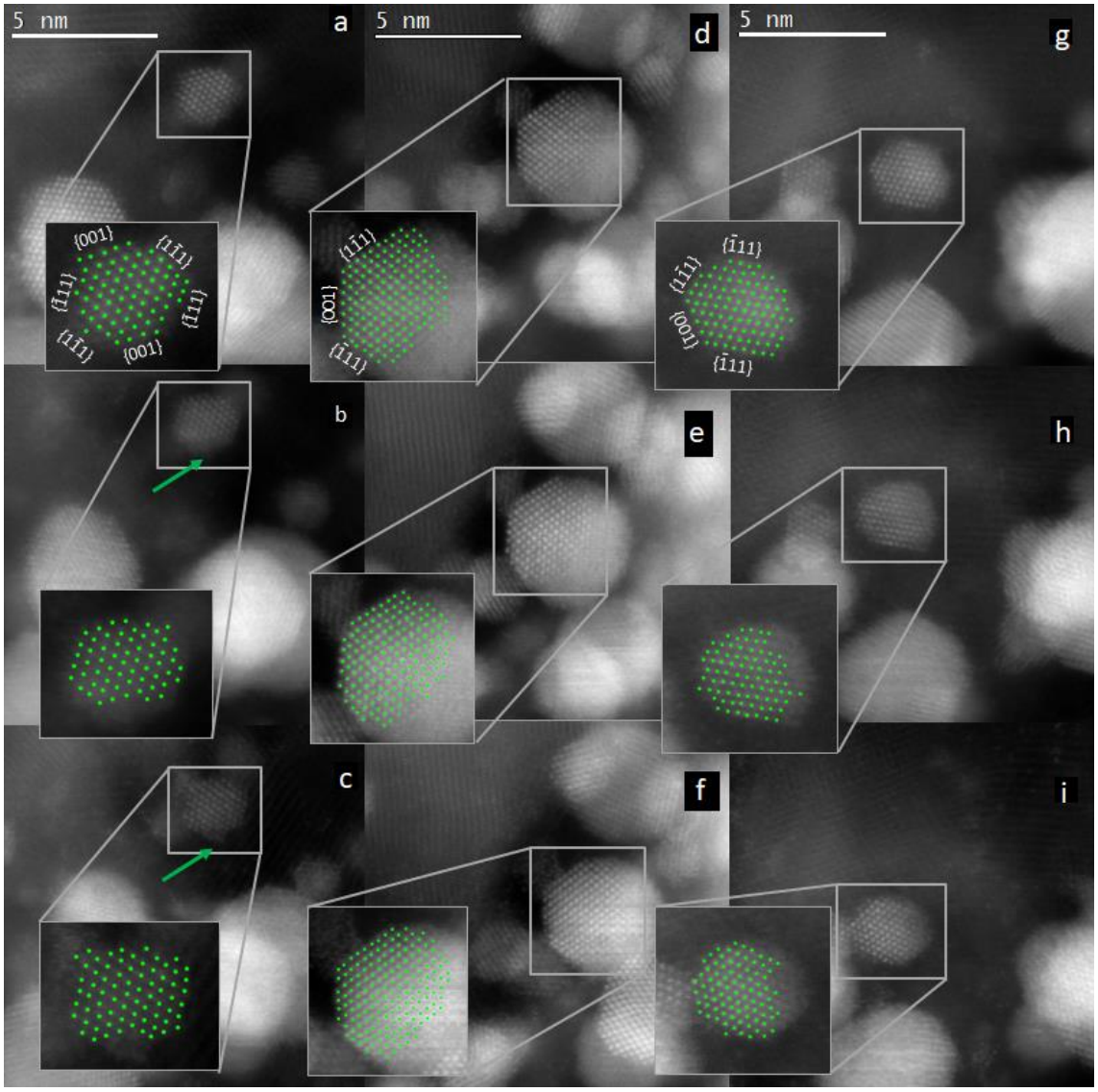

Figure A.14: IL-STEM images of Ir nanoparticles. (a-c) nanoparticle no. 1, (d-f) nanoparticle no. 3, and (g-i) nanoparticle no. 4. (a,d,g) before electrochemical treatment, (b,e,h) after potentiostatic activation, and (c,f,i) after dynamic degradation. The green dots are the positions of atomic columns. Green arrows mark sites where probably amorphous growth occurred after dynamic degradation.

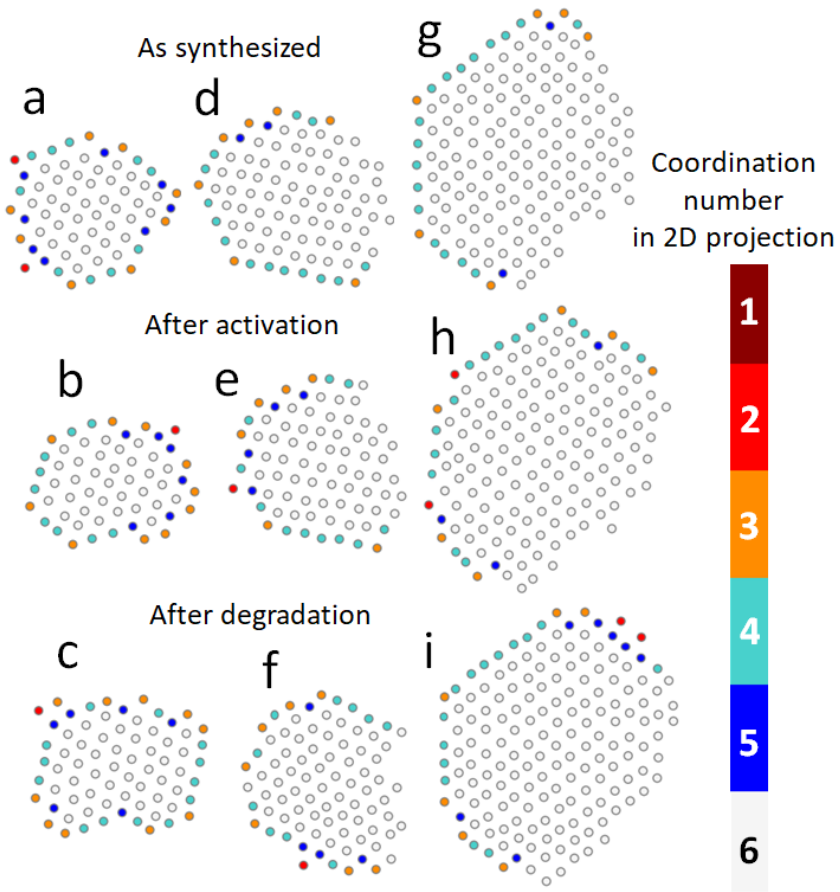

Figure A.15: Images of the atomic columns with different numbers of nearest neighbours for three Ir nanoparticles. (a-c) nanoparticle no. 1, (d-f) nanoparticle no. 4, and (g-i) nanoparticle no. 3. (a,d,g) before electrochemical treatment, (b,e,h) after potentiostatic activation, and (c,f,i) after dynamic degradation.

Appendix B

Microstructure and Electrical Conductivity of CTiON-NCNFs

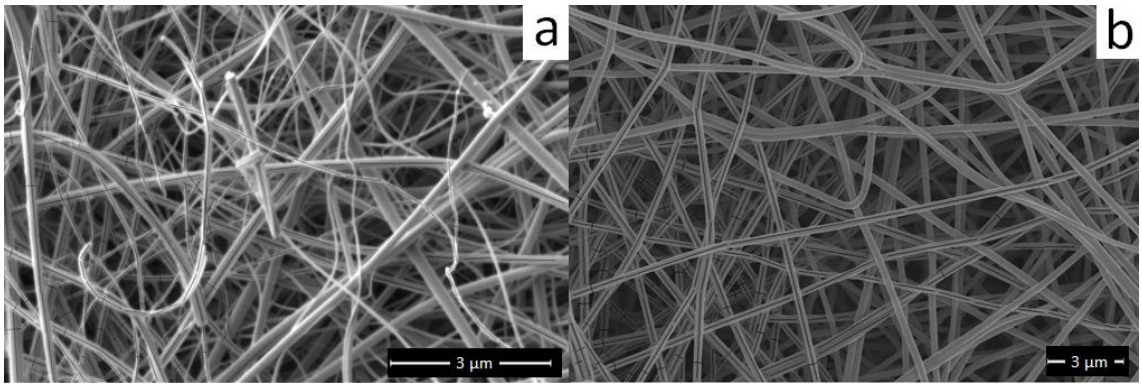

Figure B.1: SEM image of (a) CTiON-NCNF1s and (b) CTiON-NCNF2s which were used for the diameter determination. The lower left corner was the start of the measured nanofibres and the stop was at the 50th measurement.

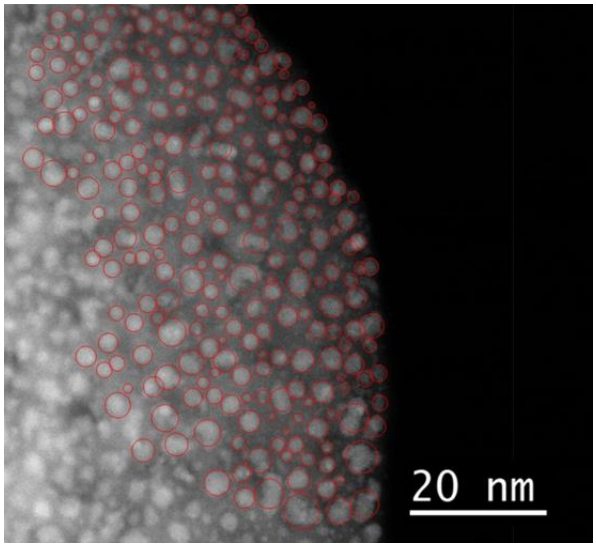

Figure B.2: STEM-HAADF image of TiON nanoparticles of CTiON-NCNF1 which were used for the diameter determination. The upper right corner was the start of the measured nanoparticles and the stop was at the 250th measurement. Circles were used as an approximation of nanoparticle shape and size.

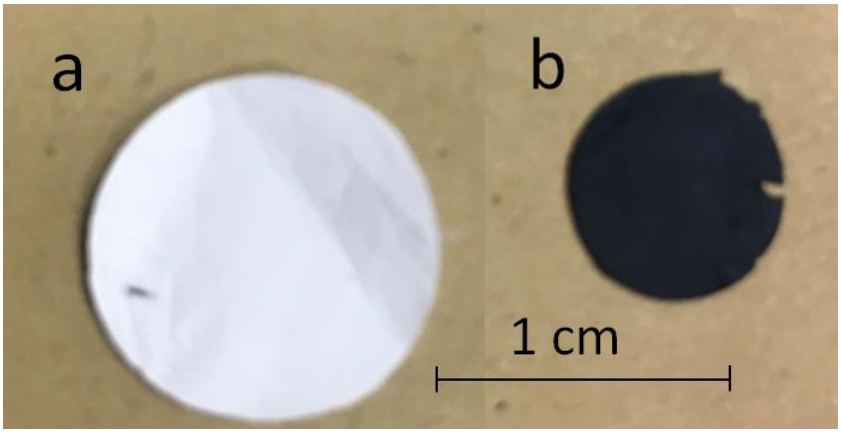

Figure B.3: Optical images of the CTiON-NCNF2 fabric sample (a) before it was nitridated and (b) after it was nitridated.

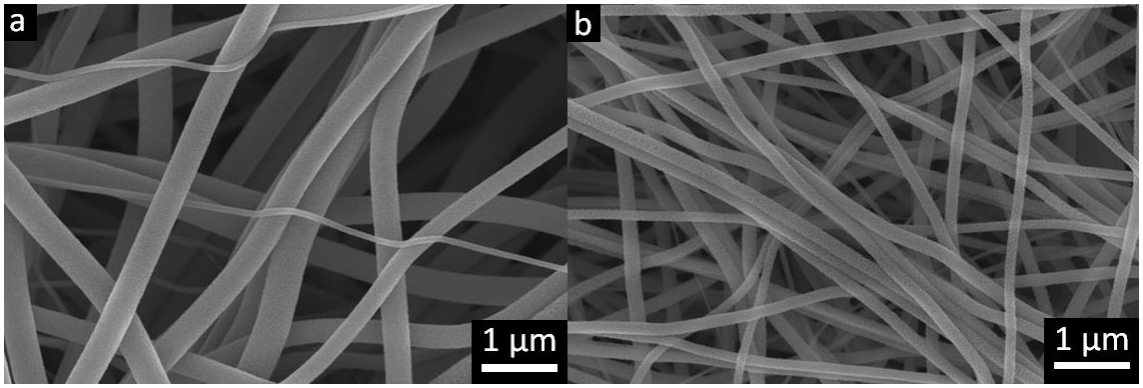

Figure B.4: SEM images of contacts between CTiON-NCNF2s (a,b).

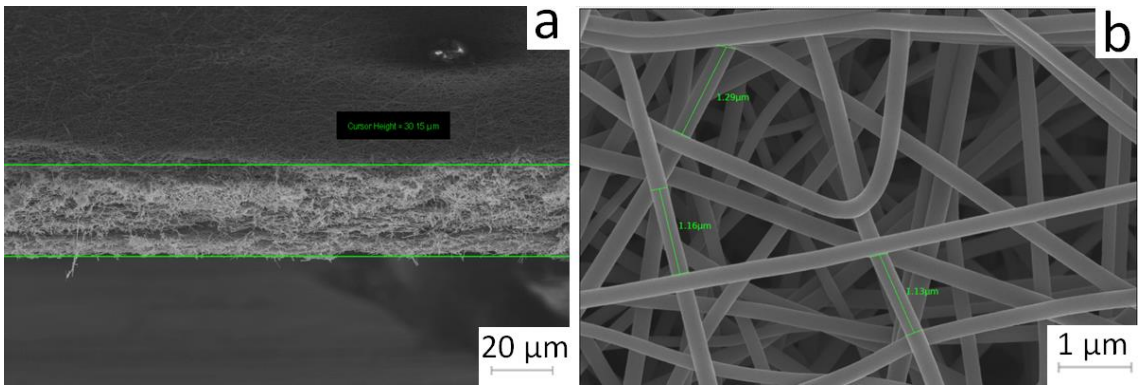

Figure B.5: SEM image of CTiON-NCNF2 fabric. (a) CTiON-NCNF2 fabric thickness and (b) examples of distances between nanofibre contacts.

B.1 CHNS and TGA Elemental Analysis

To obtain the at. % of the elements of the CTiON-NCNF1 fabric, it was analysed as bulk with CHNS and TGA analysis. CHNS analysis results give us the wt. % of H (0.9 wt. %), C (5.2 wt. %), and N (14 wt. %). The TGA curve shows a complex oxidation process of the CTiON-NCNF1 fabric (Figure B.6). Based on the assumption that only TiO_2 is left after the TGA analysis, the wt. % of Ti (70.2 wt. %) in the starting sample can be calculated from the end wt. % in Figure B.6. It can be assumed that O represents the rest of the wt % O (9.7 wt. %). We can calculate the at. % of

the elements from the wt. %. The result is 0.2 at. % H, 9.8 at. % C, 22.7 at. % N, 13.8 at. %, and O 33.3 at % Ti. From this, we get a N/O ratio of 1.65.

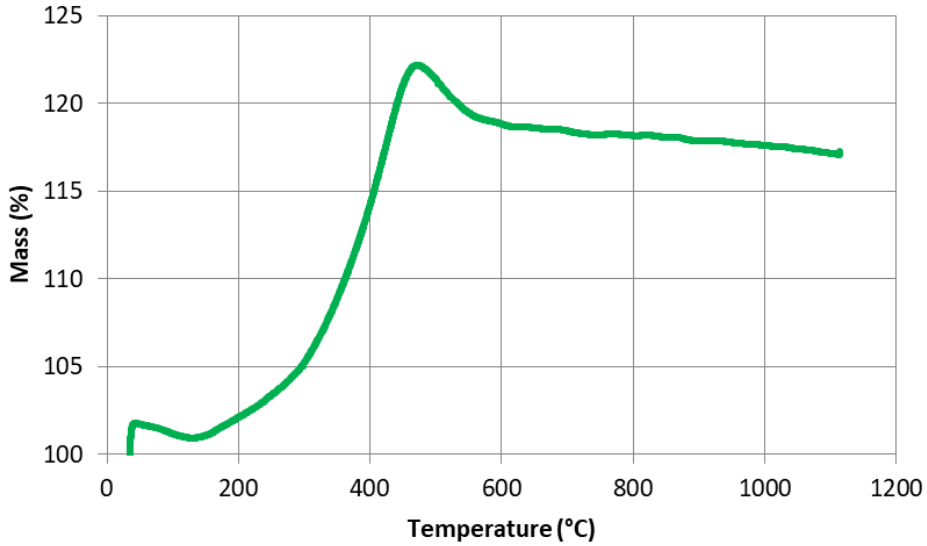

Figure B.6: TGA graph of the CTiON-NCNF1 fabric.

B.2 Raman Spectroscopy of CTiON-NCNF1s

Laser powers of 0.3 mW and 0.6 mW were used to measure the Raman spectra (Figure B.7a,b). The characteristics are equal in both spectra. The G and D bands of carbon at 1605 $cm^{-1}$and 1356 cm^{-1} are the predominant bands.

The broad overlapped bands below 800 cm^{-1} are the most interesting feature in the spectra (Figure B.7a,b) because the TiN bands appear in this spectral region. Doiron et al. found the typical TiN doublet at 260 cm^{-1} – 270 cm^{-1} and 200 cm^{-1}, and additionally, a broader band at approximately 450 cm^{-1} [153]. These bands were found in the regions 520 cm^{-1} – 610 cm^{-1} (broader band) and 180 cm^{-1} – 330 cm^{-1} (doublet) by other research groups, depending on the particle size and preparation routes [113], [154], [155]. Similarly, the bands in Figure B.7a,b with peaks at 538 cm^{-1} – 593 cm^{-1} and 222 cm^{-1} resemble the double-structured shape of TiN bands (broader band and doublet). This suggests that TiON was formed. As a side note, the existence of a small amount of amorphous TiO_2 in nanofibres cannot be excluded only based on Raman spectra.

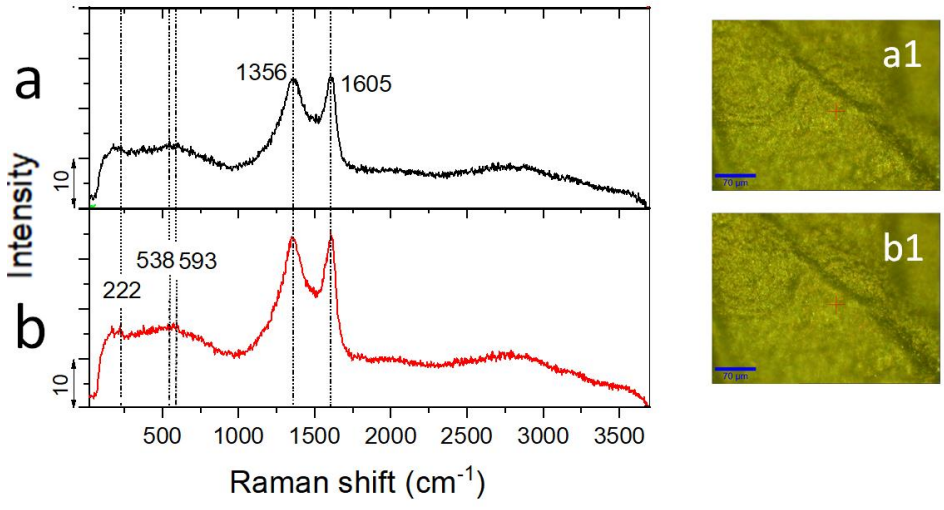

Figure B.7: Raman spectra of CTiON-NCNF1s analysed on the same position using laser powers of (a) 0.3 mW and (b) 0.6 mW. The optical images are next to the spectra (a1) initial – before spectrum a measurement and (b1) after spectrum b measurement. The measurement site is indicated by the red cross in the optical images.

B.3 Modelling of STEM EDXS Spectra of TiON/C–CNF2s

To confirm the results of quantification from the experimental STEM EDXS measurements, the STEM EDXS spectra of CTiON-NCNF1s were modelled using Monte Carlo code DTSA-II [112] (Figure B.8). This was done because the quantitative EDXS analysis of light elements can be a challenge if the geometry of the sample is not ideal (uniform and flat). The quantification results of one experimental STEM EDXS spectrum were chosen to be used as the initial input for a modelled STEM EDXS spectrum (Table B.1) and then adjusted to better fit the experimental STEM EDXS spectrum. The at. % of C was increased for better fitting of the C peak and the at. % of other elements decreased but the ratio was kept the same (Table B.1). The diameter of the measured CTiON-NCNF1 was 60 nm, that is why the material was simulated as a sphere with a density of 3.9 g cm^{-3} and a 60 nm diameter. The experimental STEM EDXS spectrum and the modelled STEM EDXS spectrum were deemed to be similar enough to trust the experimental results. The Cu Kα is due to the Cu TEM grid used as the holder of nanofibres.

Table B.1: STEM EDXS quantification results of the experimental STEM EDXS spectrum and modelled EDXS spectrum.

Element	Experimental at. %	Modelled at. %
C	8.6	12
N	20.6	19.85
O	21.3	20.5
Ti	49.5	47.65

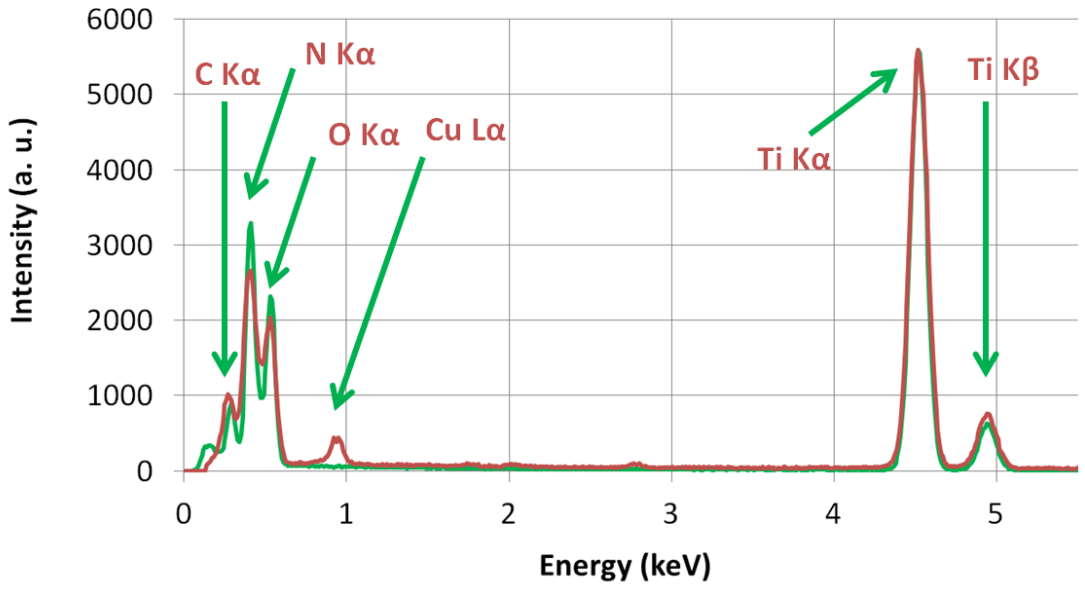

Figure B.8: A simulated STEM EDXS spectrum of a sphere consisting of C, N, O, and Ti (green line) and an STEM EDXS spectrum of a CTiON-NCNF1 (red line).

B.4 N/O Ratio Determination with EELS

A typical EELS spectrum of a CTiON-NCNF1 can be seen in Figure B.9. The signals for N (401 eV), O (532 eV), and Ti (456 eV) are separated and well resolved. Because of this, the area of the edges of all three elements can be easily quantified and their atomic percentages can be determined. The background model was subtracted from the signal before the signal was integrated for all three elements and the type of the background model was a power law type. The Gatan Digital Micrograph programme was used to calculate the integration values and express the at. % of each of the three elements. To obtain the N/O ratio, the at. % of N was divided by the at. % of O. The widths and starting points of the signals and backgrounds can be seen in Table B.2 and in Figure B.10. Four thin CTiON-NCNF1s (30 nm – 75 nm diameter) were selected to determine the average N/O ratio. In total, 10 locations were measured on the nanofibres as an area EELS signal measurement (Figure B.11). For EELS mapping, the same conditions were applied.

Table B.2: Table of widths and starting points of the signals and backgrounds for the determination of at. % of elements N, O, and Ti.

	Background		Signal	
Element	Offset (eV)	Width (eV)	Offset (eV)	Width (eV)
N	-43.1	35.0	-0.1	25.0
O	-28.1	35.0	-0.1	25.0
Ti	-23.1	20	-0.1	25.0

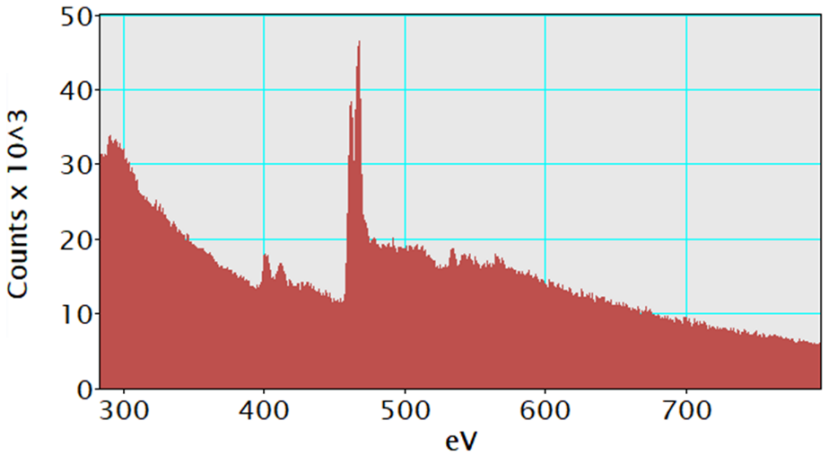

Figure B.9: Representative EELS spectrum of a CTiON-NCNF1.

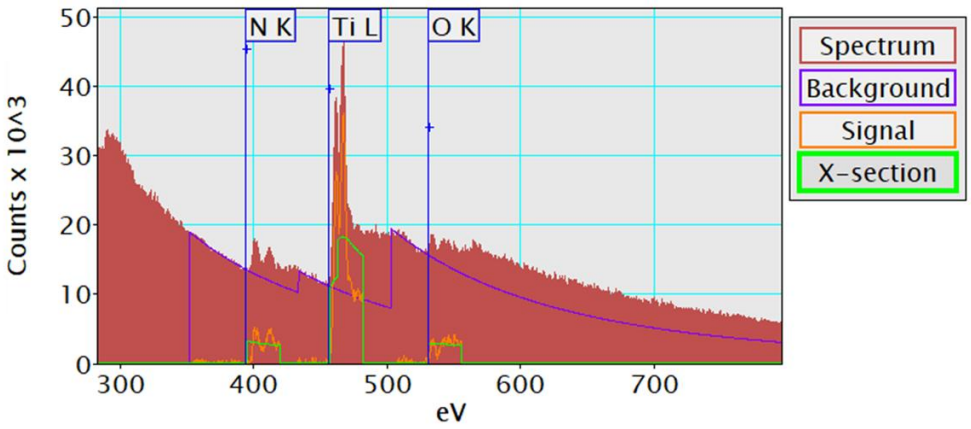

Figure B.10: Representative EELS spectrum of a CTiON-NCNF1 with labelled starting points of signal integration (green), ranges and starting points of background determination for background subtraction (purple), and the signal after background subtraction (orange).

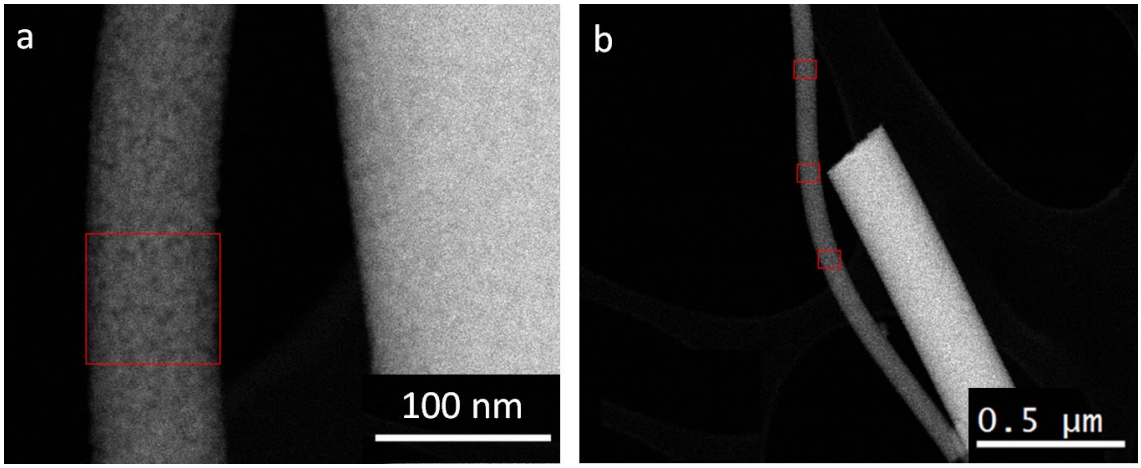

Figure B.11: STEM-HAADF images of CTiON-NCNF1s (a,b) with examples of EELS analysis area size (red square) and measurement locations.

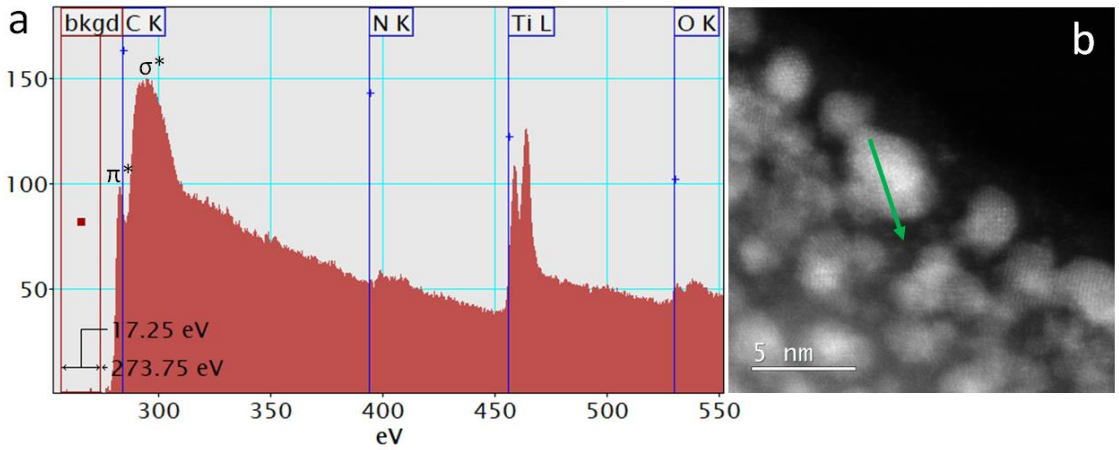

Figure B.12: EELS spectrum of the carbon matrix of the CTiON-NCNF1 (a) with background subtracted and (b) the location on the STEM-HAADF image where the EELS spectrum was taken (green arrow).

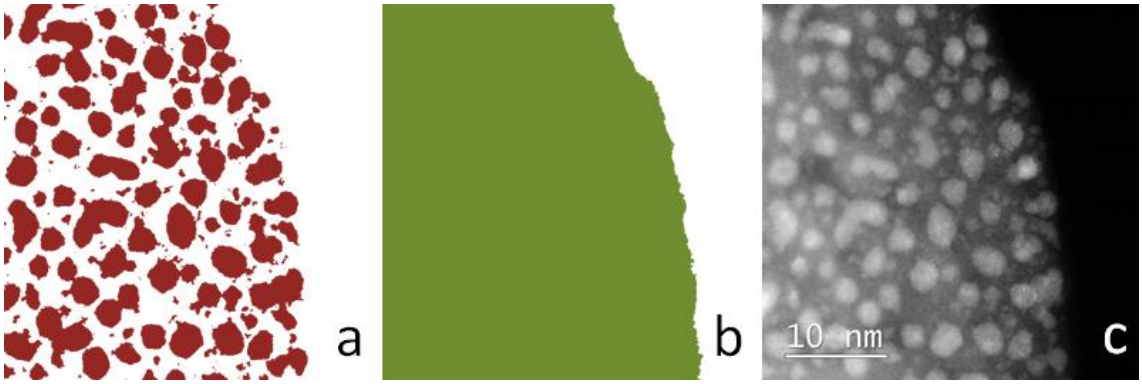

Figure B.13: STEM–HAADF images of the two-phase nanocomposite CTiON-NCNF1 which consists of the C matrix and TiON nanoparticles. (a) the outline of the TiON nanoparticles made with three steps: Gaussian blur, rolling ball background subtraction, and thresholding. (b) the outline of the CTiON-NCNF1 area was made with two steps: Gaussian blur and thresholding. (c) the original image. To estimate the nanopore volume fraction, a separate image was used.

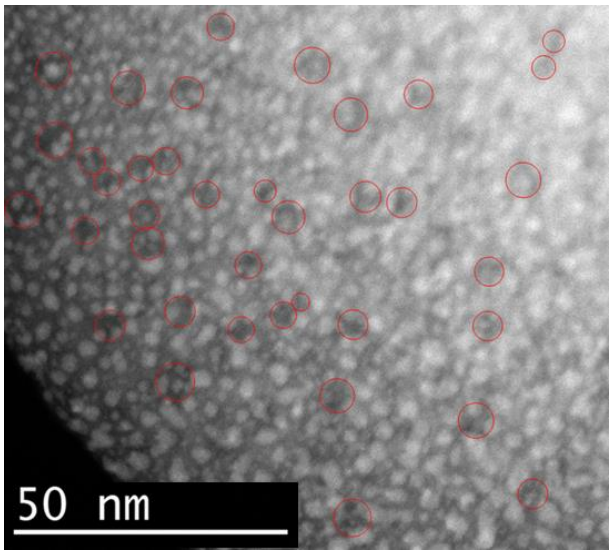

Figure B.14: STEM-HAADF image of a nanocomposite CTiON-NCNF1. To roughly estimate the location and size of the nanopores, the nanopores were encircled in.

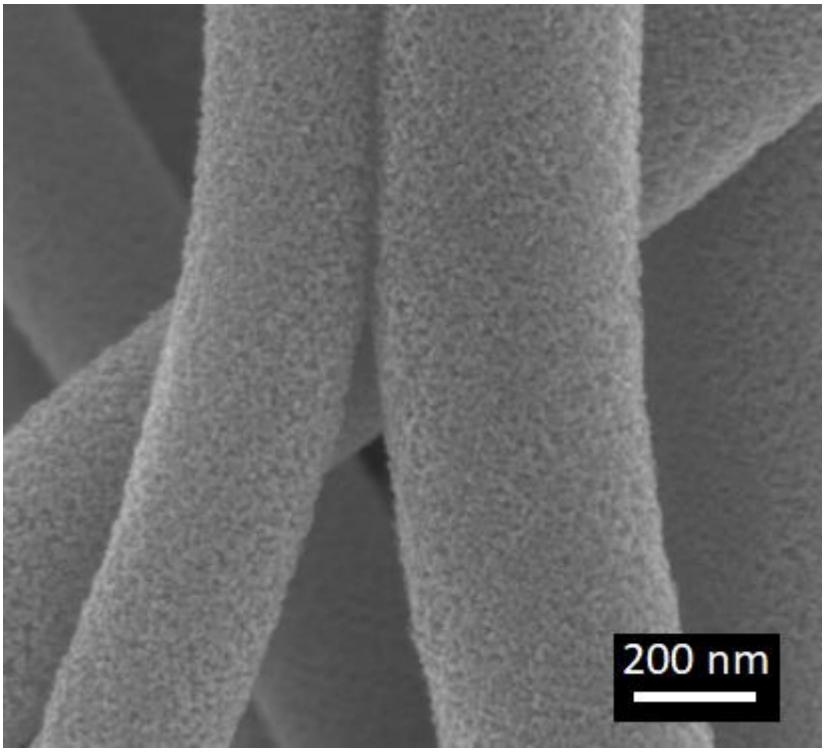

Figure B.15: SEM image of CTiON-NCNF2s at high magnification.

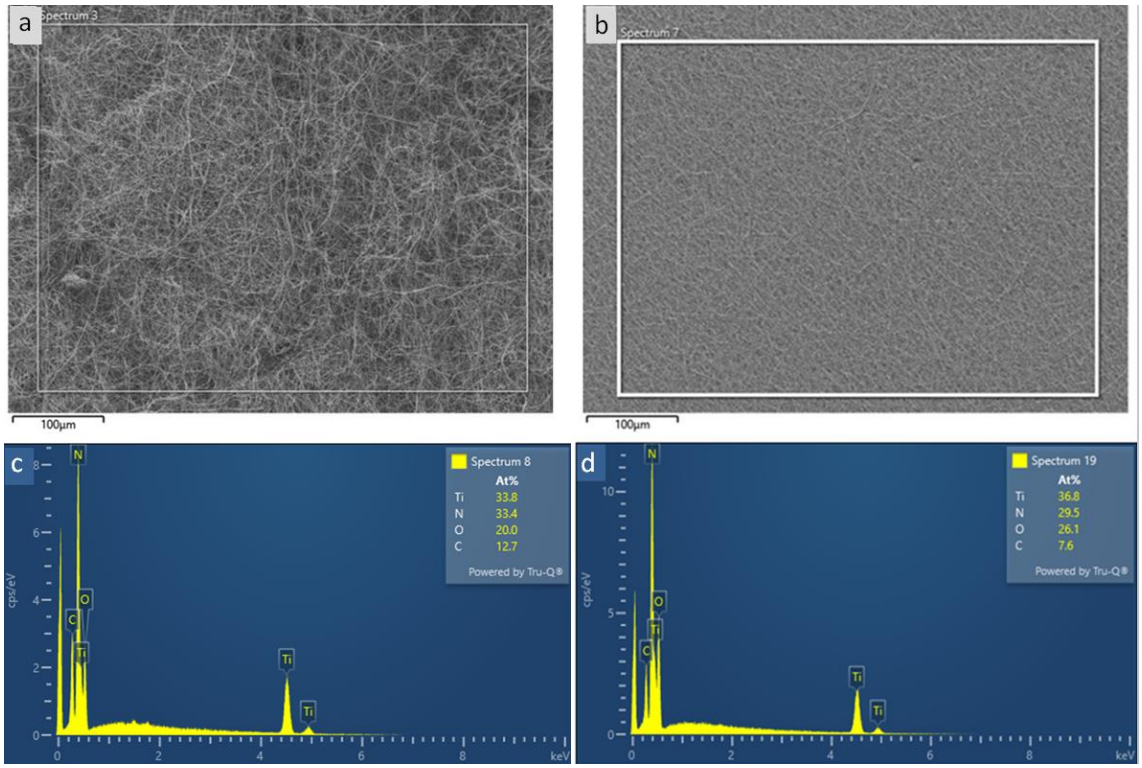

Figure B.16: SEM EDXS analysis of CTiON-NCNF1 and CTiON-NCNF2 fabric. a) SEM image of the location on CTiON-NCNF1 fabric where SEM EDXS analysis was made, b) SEM image of the location on CTiON-NCNF2 fabric where SEM EDXS analysis was made, c) SEM EDXS analysis of CTiON-NCNF1 with at. % composition, and d) SEM EDXS analysis of CTiON-NCNF2 with at. % composition.

References

[1] "Coal consumption affecting climate," *The Rodney and Otamatea Times, Waitemata and Kaipara Gazette*, Warkworth, p. 7, 1912.

[2] S. Arrhenius, "On the Influence of Carbonic Acid in the Air upon the Temperature of the Ground," *Philos. Mag. J. Sci.*, vol. 41, no. 5, pp. 237–276, 1896.

[3] R. K. Pachauri and L. A. Meyer, "IPCC, 2014: Climate Change 2014: Synthesis Report. Contribution of Working Groups I, II and III to the Fifth Assessment Report of the Intergovernmental Panel on Climate Change," Geneva, Switzerland, 2014.

[4] S. Shiva Kumar and V. Himabindu, "Hydrogen production by PEM water electrolysis – A review," *Mater. Sci. Energy Technol.*, vol. 2, no. 3, pp. 442–454, Dec. 2019.

[5] S. Zhang, X. Z. Yuan, J. N. C. Hin, H. Wang, K. A. Friedrich, and M. Schulze, "A review of platinum-based catalyst layer degradation in proton exchange membrane fuel cells," *J. Power Sources*, vol. 194, no. 2, pp. 588–600, 2009.

[6] L. Braic *et al.*, "Titanium Oxynitride Thin Films with Tunable Double Epsilon-Near-Zero Behavior for Nanophotonic Applications," *ACS Appl. Mater. Interfaces*, vol. 9, no. 35, pp. 29857–29862, 2017.

[7] S. K. Rawal, A. K. Chawla, V. Chawla, R. Jayaganthan, and R. Chandra, "Effect of ambient gas on structural and optical properties of titanium oxynitride films," *Appl. Surf. Sci.*, vol. 256, no. 13, pp. 4129–4135, 2010.

[8] E. Zoulias, E. Varkaraki, N. Lymberopoulos, C. N. Christodoulou, and G. N. Karagiorgis, "A Review on Water Electrolysis," *Tcjst*, vol. 4, no. 2, pp. 41–71, 2004.

[9] M. Carmo, D. L. Fritz, J. Mergel, and D. Stolten, "A comprehensive review on PEM water electrolysis," *Int. J. Hydrogen Energy*, vol. 38, no. 12, pp. 4901–4934, Apr. 2013.

[10] L. K. Kurihara, G. M. Chow, and P. E. Schoen, "Nanocrystalline metallic powders and films produced by the polyol method," *Nanostructured Mater.*, vol. 5, no. 6, pp. 607–613, Aug. 1995.

[11] G. Demazeau, "Solvothermal processes: a route to the stabilization of new materials," *J. Mater. Chem.*, vol. 9, no. 1, pp. 15–18, Jan. 1999.

[12] R. Adams and R. L. Shriner, "Platinum oxide as a catalyst in the reduction of organic compounds. III. Preparation and properties of the oxide of platinum obtained by the fusion of chloroplatinic acid with sodium nitrate," *J. Am. Chem. Soc.*, vol. 45, no. 9, pp. 2171–2179, Sep. 1923.

[13] P. A. Morris Hotsenpiller, G. A. Wilson, A. Roshko, J. B. Rothman, and G. S. Rohrer, "Heteroepitaxial growth of TiO2 films by ion-beam sputter deposition," vol. 166, pp. 779–785, 1996.

[14] I. M. Ismail, B. Abdallah, M. Abou-Kharroub, and O. Mrad, "XPS and RBS investigation of TiNxOy films prepared by vacuum arc discharge," *Nucl. Instruments Methods Phys. Res. Sect. B Beam Interact. with Mater. Atoms*, vol. 271, pp. 102–106, 2012.

[15] M. H. Kazemeini, A. A. Berezin, and N. Fukuhara, "Formation of thin TiNxOy films by using a hollow cathode reactive DC sputtering system," *Thin Solid Films*, vol. 372, no. 1, pp. 70–77, 2000.

[16] P. K. Barhai, N. Kumari, I. Banerjee, S. K. Pabi, and S. K. Mahapatra, "Study of the effect

of plasma current density on the formation of titanium nitride and titanium oxynitride thin films prepared by reactive DC magnetron sputtering," *Vacuum*, vol. 84, no. 7, pp. 896–901, 2010.

[17] L. Yan *et al.*, "Titanium Oxynitride Nanoparticles Anchored on Carbon Nanotubes as Energy Storage Materials," *ACS Appl. Mater. Interfaces*, vol. 7, no. 43, pp. 24212–24217, 2015.

[18] M. Drygaś, C. Czosnek, R. T. Paine, and J. F. Janik, "Two-stage aerosol synthesis of titanium nitride TiN and titanium oxynitride TiOxNy nanopowders of spherical particle morphology," *Chem. Mater.*, vol. 18, no. 13, pp. 3122–3129, 2006.

[19] M. J. Jung, K. H. Nam, Y. M. Chung, J. H. Boo, and J. G. Han, "The physiochemical properties of TiOxNy films with controlled oxygen partial pressure," *Surf. Coatings Technol.*, vol. 171, no. 1–3, pp. 71–74, 2003.

[20] J. Guillot, J. M. Chappé, O. Heintz, N. Martin, L. Imhoff, and J. Takadoum, "Phase mixture in MOCVD and reactive sputtering TiOxNy thin films revealed and quantified by XPS factorial analysis," *Acta Mater.*, vol. 54, no. 11, pp. 3067–3074, 2006.

[21] F. Fabreguette *et al.*, "Temperature and substrate influence on the structure of TiNxOy thin films grown by low pressure metal organic chemical vapour deposition," *Surf. Coatings Technol.*, vol. 125, no. 1–3, pp. 396–399, 2000.

[22] B. F. Fabreguette *et al.*, "Correlation Between the Electrical Properties and Morphology of Low-Pressure MOCVD Titanium Oxynitride Thin Films Grown at Various Temperatures," *Chem. Vap. Depos.*, vol. 6, no. 3, pp. 109–114, 2000.

[23] G. Hyett, M. A. Green, and I. P. Parkin, "The use of combinatorial chemical vapor deposition in the synthesis of Ti3-δO4N with 0.06 - δ - 0.25: A titanium oxynitride phase isostructural to anosovite," *J. Am. Chem. Soc.*, vol. 129, no. 50, pp. 15541–15548, 2007.

[24] P. Simon *et al.*, "X-ray absorption investigation of titanium oxynitride nanoparticles obtained from laser pyrolysis," *Chem. Phys.*, vol. 418, pp. 47–56, 2013.

[25] P. Simon *et al.*, "N-doped titanium monoxide nanoparticles with TiO rock-salt structure, low energy band gap, and visible light activity," *Chem. Mater.*, vol. 22, no. 12, pp. 3704–3711, 2010.

[26] B. Subramanian, C. V. Muraleedharan, R. Ananthakumar, and M. Jayachandran, "A comparative study of titanium nitride (TiN), titanium oxy nitride (TiON) and titanium aluminum nitride (TiAlN), as surface coatings for bio implants," *Surf. Coatings Technol.*, vol. 205, no. 21–22, pp. 5014–5020, 2011.

[27] M. Braic *et al.*, "Preparation and characterization of titanium oxy-nitride thin films," *Appl. Surf. Sci.*, vol. 253, no. 19, pp. 8210–8214, 2007.

[28] K. A. Soliman *et al.*, "Silver Nanoparticles-Decorated Titanium Oxynitride Nanotube Arrays for Enhanced Solar Fuel Generation," *Sci. Rep.*, vol. 7, no. 1, pp. 1–8, 2017.

[29] M. Chisaka, A. Ishihara, K. I. Ota, and H. Muramoto, "Synthesis of carbon-supported titanium oxynitride nanoparticles as cathode catalyst for polymer electrolyte fuel cells," *Electrochim. Acta*, vol. 113, pp. 735–740, 2013.

[30] A. Seifitokaldani, K. Oishi, M. Perrier, and O. Savadogo, "Electrochemical and physicochemical properties of titanium Oxy-nitride electrocatalyst prepared by sol-gel methods for the oxygen reduction reaction purposes," *J. Solid State Electrochem.*, vol. 19, no. 10, pp. 3097–3109, 2015.

[31] J. Graciani, J. Fdez Sanz, T. Asaki, K. Nakamura, and J. A. Rodriguez, "Interaction of oxygen with TiN (001): N↔O exchange and oxidation process," *J. Chem. Phys.*, vol. 126, no. 24, pp. 1–9, 2007.

[32] M. Batzill, E. H. Morales, and U. Diebold, "Influence of nitrogen doping on the defect formation and surface properties of TiO2 rutile and anatase," *Phys. Rev. Lett.*, vol. 96, no. 2, pp. 1–4, 2006.

[33] M. V. Diamanti, M. Ormellese, and M. P. Pedeferri, "Application-wise nanostructuring of

anodic films on titanium: a review," *http://dx.doi.org/10.1080/17458080.2014.999261*, vol. 10, no. 17, pp. 1285–1308, Nov. 2015.

[34] W. E. Teo and S. Ramakrishna, "A review on electrospinning design and nanofibre assemblies," *Nanotechnology*, vol. 17, no. 14, p. R89, Jun. 2006.

[35] "Beyond the diffraction limit," *Nat. Photonics 2009 37*, vol. 3, no. 7, pp. 361–361, Jul. 2009.

[36] R. Courtland, "The microscope revolution that's sweeping through materials science," *Nature*, vol. 563, no. 7732, pp. 462–464, Nov. 2018.

[37] D. B. Williams and C. B. Carter, "Transmission electron microscopy: A textbook for materials science," *Transm. Electron Microsc. A Textb. Mater. Sci.*, pp. 1–760, 2009.

[38] A. Ul-Hamid, "A Beginners' Guide to Scanning Electron Microscopy," *A Beginners' Guid. to Scanning Electron Microsc.*, 2018.

[39] N. Hodnik and S. Cherevko, "Spot the difference at the nanoscale: identical location electron microscopy in electrocatalysis," *Curr. Opin. Electrochem.*, vol. 15, pp. 73–82, Jun. 2019.

[40] K. J. J. J. Mayrhofer *et al.*, "Fuel cell catalyst degradation on the nanoscale," *Electrochem. commun.*, vol. 10, pp. 1144–1147, Aug. 2008.

[41] P. Jovanovič *et al.*, "Methodology for Investigating Electrochemical Gas Evolution Reactions: Floating Electrode as a Means for Effective Gas Bubble Removal," *Anal. Chem.*, vol. 91, no. 16, pp. 10353–10356, Aug. 2019.

[42] T. W. van Deelen, C. Hernández Mejía, and K. P. de Jong, "Control of metal-support interactions in heterogeneous catalysts to enhance activity and selectivity," *Nature Catalysis*, vol. 2, no. 11. Nature Publishing Group, pp. 955–970, Nov-2019.

[43] J. M. Macak *et al.*, "TiO2 nanotubes: Self-organized electrochemical formation, properties and applications," *Curr. Opin. Solid State Mater. Sci.*, vol. 11, no. 1, pp. 3–18, 2007.

[44] P. Wang, Y. H. Ng, and R. Amal, "Embedment of anodized p-type Cu2O thin films with CuO nanowires for improvement in photoelectrochemical stability," *Nanoscale*, vol. 5, no. 7, pp. 2952–2958, 2013.

[45] C.-Y. Lee, K. Lee, and P. Schmuki, "Anodic Formation of Self-Organized Cobalt Oxide Nanoporous Layers," *Angew. Chemie Int. Ed.*, vol. 52, no. 7, pp. 2077–2081, Feb. 2013.

[46] S. J. Kim and J. Choi, "Self-assembled arrays of ZnO stripes by anodization," *Electrochem. commun.*, vol. 10, no. 1, pp. 175–179, 2008.

[47] M. Yang, N. K. Shrestha, and P. Schmuki, "Thick porous tungsten trioxide films by anodization of tungsten in fluoride containing phosphoric acid electrolyte," *Electrochem. commun.*, vol. 11, no. 10, pp. 1908–1911, 2009.

[48] K. Gulati, A. Santos, D. Findlay, and D. Losic, "Optimizing anodization conditions for the growth of titania nanotubes on curved surfaces," *J. Phys. Chem. C*, vol. 119, no. 28, pp. 16033–16045, Jul. 2015.

[49] Z. Liu, V. (Ravi) Subramania, and M. Misra, "Vertically Oriented TiO2 Nanotube Arrays Grown on Ti Meshes for Flexible Dye-Sensitized Solar Cells," *J. Phys. Chem. C*, vol. 113, no. 31, pp. 14028–14033, Aug. 2009.

[50] L. Suhadolnik, D. Lašič Jurković, B. Likozar, M. Bele, S. Drev, and M. Čeh, "Structured titanium oxynitride (TiOxNy) nanotube arrays for a continuous electrocatalytic phenol-degradation process: Synthesis, characterization, mechanisms and the chemical reaction micro-kinetics," *Appl. Catal. B Environ.*, vol. 257, p. 117894, Nov. 2019.

[51] Ž. Marinko, L. Suhadolnik, Z. Samardžija, J. Kovač, and M. Čeh, "The Influence of a Surface Treatment of Metallic Titanium on the Photocatalytic Properties of TiO2 Nanotubes Grown by Anodic Oxidation," *Catalysts* , vol. 10, no. 7. 2020.

[52] D. Lebedev and C. Copéret, "Small, narrowly distributed iridium nanoparticles supported on indium tin oxide for efficient anodic water oxidation," *ACS Appl. Energy Mater.*, vol.

2, no. 1, pp. 196–200, Jan. 2019.
[53] J. Zhang *et al.*, “Iridium nanoparticles anchored on 3D graphite foam as a bifunctional electrocatalyst for excellent overall water splitting in acidic solution,” *Nano Energy*, vol. 40, pp. 27–33, 2017.
[54] Y. N. Regmi *et al.*, “Supported Oxygen Evolution Catalysts by Design: Toward Lower Precious Metal Loading and Improved Conductivity in Proton Exchange Membrane Water Electrolyzers,” *ACS Catal.*, vol. 10, no. 21, pp. 13125–13135, Nov. 2020.
[55] H. Ohno *et al.*, “Remarkable Mass Activities for the Oxygen Evolution Reaction at Iridium Oxide Nanocatalysts Dispersed on Tin Oxides for Polymer Electrolyte Membrane Water Electrolysis,” *J. Electrochem. Soc.*, vol. 164, no. 9, pp. F944–F947, 2017.
[56] E. Oakton *et al.*, “IrO2-TiO2: A High-Surface-Area, Active, and Stable Electrocatalyst for the Oxygen Evolution Reaction,” *ACS Catal.*, vol. 7, no. 4, pp. 2346–2352, 2017.
[57] C. Van Pham *et al.*, “IrO2 coated TiO2 core-shell microparticles advance performance of low loading proton exchange membrane water electrolyzers,” *Appl. Catal. B Environ.*, vol. 269, no. February, p. 118762, Jul. 2020.
[58] K. Zhang, W. Mai, J. Li, H. Wang, G. Li, and W. Hu, “Highly scattered Ir oxides on TiN as an efficient oxygen evolution reaction electrocatalyst in acidic media,” *J. Mater. Sci.*, vol. 55, no. 8, pp. 3507–3520, 2020.
[59] H. S. Oh *et al.*, “Electrochemical Catalyst-Support Effects and Their Stabilizing Role for IrOx Nanoparticle Catalysts during the Oxygen Evolution Reaction,” *J. Am. Chem. Soc.*, vol. 138, no. 38, pp. 12552–12563, Sep. 2016.
[60] H. S. Oh, H. N. Nong, and P. Strasser, “Preparation of mesoporous Sb-, F-, and in-doped SnO2bulk powder with high surface area for use as catalyst supports in electrolytic cells,” *Adv. Funct. Mater.*, vol. 25, no. 7, pp. 1074–1081, 2015.
[61] L. Wang *et al.*, “Improving the activity and stability of Ir catalysts for PEM electrolyzer anodes by SnO2:Sb aerogel supports: does V addition play an active role in electrocatalysis?,” *J. Mater. Chem. A*, vol. 5, no. 7, pp. 3172–3178, Feb. 2017.
[62] H. N. Nong *et al.*, “Oxide-supported IrNiO(x) core-shell particles as efficient, cost-effective, and stable catalysts for electrochemical water splitting.,” *Angew. Chem. Int. Ed. Engl.*, vol. 54, no. 10, pp. 2975–9, Mar. 2015.
[63] M. Bele *et al.*, “Towards Stable and Conductive Titanium Oxynitride High-Surface-Area Support for Iridium Nanoparticles as Oxygen Evolution Reaction Electrocatalyst,” *ChemCatChem*, vol. 11, no. 20, pp. 5038–5044, Oct. 2019.
[64] L. Moriau *et al.*, “Effect of the Morphology of the High-Surface-Area Support on the Performance of the Oxygen-Evolution Reaction for Iridium Nanoparticles,” *ACS Catal.*, vol. 11, no. 2, pp. 670–681, Jan. 2021.
[65] L. Moriau *et al.*, “Enhancing Iridium Nanoparticles ’ Oxygen Evolution Reaction Activity and Stability by Adjusting the Coverage of Titanium Oxynitride Flakes on Reduced Graphene Oxide Nanoribbons ’ Support,” vol. 2100900, 2021.
[66] M. Bele *et al.*, “Increasing the Oxygen-Evolution Reaction Performance of Nanotubular Titanium Oxynitride-Supported Ir Nanoparticles by a Strong Metal-Support Interaction,” *ACS Catal.*, vol. 10, no. 22, pp. 13688–13700, Nov. 2020.
[67] A. Lončar *et al.*, “Sacrificial Cu Layer Mediated the Formation of an Active and Stable Supported Iridium Oxygen Evolution Reaction Electrocatalyst,” *ACS Catal.*, vol. 11, no. 20, pp. 12510–12519, Oct. 2021.
[68] L. J. Moriau *et al.*, “Resolving the nanoparticles’ structure-property relationships at the atomic level: a study of Pt-based electrocatalysts,” *iScience*, vol. 24, no. 2, p. 102102, Feb. 2021.
[69] A. Hrnjic *et al.*, “Observing, tracking and analysing electrochemically induced atomic-scale structural changes of an individual Pt-Co nanoparticle as a fuel cell electrocatalyst by combining modified floating electrode and identical location electron microscopy,”

Electrochim. Acta, vol. 388, p. 138513, Aug. 2021.

[70] V. Thavasi, G. Singh, and S. Ramakrishna, "Electrospun nanofibres in energy and environmental applications," *Energy Environ. Sci.*, vol. 1, no. 2, pp. 205–221, Jul. 2008.

[71] J. G. Kim *et al.*, "Structurally and electronically designed TiO2Nx nanofibres for lithium rechargeable batteries," *ACS Appl. Mater. Interfaces*, vol. 5, no. 3, pp. 691–696, Feb. 2013.

[72] T. T. Chen *et al.*, "Porous titanium oxynitride sheets as electrochemical electrodes for energy storage," *Nanoscale*, vol. 6, no. 10, pp. 5106–5109, Apr. 2014.

[73] Y. Ze *et al.*, "Electrical Conductivity Studies on Individual Conjugated Polymer Nanowires: Two-Probe and Four-Probe Results," 2010.

[74] C. L. Lee, C. Kim, and I. D. Kim, "Ultrasmall titanium oxide/titanium oxynitride composite nanoparticle-embedded carbon nanofibre mats as high-capacity and free-standing electrodes for lithium sulfur batteries," *RSC Adv.*, vol. 7, no. 71, pp. 44804–44808, Sep. 2017.

[75] S. Sharma and B. G. Pollet, "Support materials for PEMFC and DMFC electrocatalysts - A review," *J. Power Sources*, vol. 208, no. January, pp. 96–119, 2012.

[76] J. Dong *et al.*, "Pseudocapacitive titanium oxynitride mesoporous nanowires with iso-oriented nanocrystals for ultrahigh-rate sodium ion hybrid capacitors," *J. Mater. Chem. A*, vol. 5, no. 22, pp. 10827–10835, Jun. 2017.

[77] A. Kaur and R. P. Chauhan, "Modifications induced by silicon and nickel ion beams in the electrical conductivity of zinc nanowires," *J. Mater. Sci. Mater. Electron.*, vol. 24, no. 11, pp. 4302–4310, Nov. 2013.

[78] M. A. Othman, N. F. Amat, B. H. Ahmad, and J. Rajan, "Electrical Conductivity Characteristic of TiO2 Nanowires From Hydrothermal Method," *J. Phys. Conf. Ser.*, vol. 495, no. 1, p. 012027, Apr. 2014.

[79] A. A. Haroun and A. M. Youssef, "Synthesis and electrical conductivity evaluation of novel hybrid poly (methyl methacrylate)/titanium dioxide nanowires," *Synth. Met.*, vol. 161, no. 19–20, pp. 2063–2069, Oct. 2011.

[80] H. Li, W. Pan, W. Zhang, S. Huang, and H. Wu, "TiN Nanofibres: A New Material with High Conductivity and Transmittance for Transparent Conductive Electrodes," *Adv. Funct. Mater.*, vol. 23, no. 2, pp. 209–214, Jan. 2013.

[81] P. Chen, H. Li, S. Hu, T. Zhou, Y. Yan, and W. Pan, "Copper-coated TiN nanofibres with high electrical conductivity: a new advance in conductive one-dimensional nanostructures," *J. Mater. Chem. C*, vol. 3, no. 28, pp. 7272–7276, Jul. 2015.

[82] G. Zhou, T. Xiong, S. Jiang, S. Jian, Z. Zhou, and H. Hou, "Flexible titanium carbide–carbon nanofibres with high modulus and high conductivity by electrospinning," *Mater. Lett.*, vol. 165, pp. 91–94, Feb. 2016.

[83] T. K. Chin, M. W. Liao, and T. P. Perng, "Enabling higher electrochemical activity of Pt nanoparticles uniformly coated on cubic titanium oxynitride by vertical forced-flow atomic layer deposition," *J. Power Sources*, vol. 434, p. 226716, Sep. 2019.

[84] E. J. Lee, L. Lee, M. A. Abbas, and J. H. Bang, "The influence of surface area, porous structure, and surface state on the supercapacitor performance of titanium oxynitride: implications for a nanostructuring strategy," *Phys. Chem. Chem. Phys.*, vol. 19, no. 31, pp. 21140–21151, Aug. 2017.

[85] E. Enríquez, A. Mariscal, R. Serna, and J. F. Fernández, "Transparent high conductive Titanium oxynitride nanofilms obtained by nucleation control for sustainable optolectronics," *Appl. Surf. Sci.*, vol. 574, p. 151631, Feb. 2022.

[86] N. Reddy Mucha *et al.*, "High-Performance Titanium Oxynitride Thin Films for Electrocatalytic Water Oxidation," *ACS Appl. Energy Mater.*, vol. 3, no. 9, pp. 8366–8374, Sep. 2020.

[87] H. Do, Y. H. Wu, V. T. Dai, C. Y. Peng, T. C. Yen, and L. Chang, "Structure and property of

epitaxial titanium oxynitride grown on MgO(001) substrate by pulsed laser deposition," *Surf. Coatings Technol.*, vol. 214, pp. 91–96, Jan. 2013.

[88] J. Shashikant Samdani, T.-H. Kang, B.-J. Lee, Y. Hee Jang, J.-S. Yu, and S. Shanmugam, "Heterostructured Titanium Oxynitride-Manganese Cobalt Oxide Nanorods as High-Performance Electrode Materials for Supercapacitor Devices," *ACS Appl. Mater. Interfaces*, vol. 12, no. 49, pp. 54524–54536, Dec. 2020.

[89] J. H. Han and J. H. Bang, "A hollow titanium oxynitride nanorod array as an electrode substrate prepared by the hot ammonia-induced Kirkendall effect," *J. Mater. Chem. A*, vol. 2, no. 27, pp. 10568–10576, Jun. 2014.

[90] Weixing Niu, Yani Guan, Yuhong Luo, Guihua Liu, and Jingde Li, "A macroporous titanium oxynitride-supported bifunctional oxygen electrocatalyst for zinc–air batteries," *Catal. Sci. Technol.*, 2021.

[91] Y. Noh *et al.*, "Heat Treatment–Controlled Morphology Modification of Electrospun Titanium Oxynitride Nanowires for Capacitive Energy Storage and Electrocatalytic Reactions," *Energy Technol.*, vol. 8, no. 6, p. 2000184, Jun. 2020.

[92] J. Horkstra, L. J. Van der Pauw, and N. V. Philips, "Measurement of the Resistivity Constants of Anistotropic Conductors by means of Plane-Parallel Discs of Arbitrary Shape," *J. Electron. Control*, vol. 7, no. 2, 2007.

[93] L. J. Van der Pauw, "A method of measuring specific resistivity and Hall effect of discs of arbitrary shape," *Philips Research Reports*, vol. 13. pp. 1–9, 1958.

[94] A. Hrnjić *et al.*, "Modified Floating Electrode Apparatus for Advanced Characterization of Oxygen Reduction Reaction Electrocatalysts," *J. Electrochem. Soc.*, vol. 167, no. 16, p. 166501, Dec. 2020.

[95] C. Gebauer *et al.*, "Performance of titanium oxynitrides in the electrocatalytic oxygen evolution reaction," *Nano Energy*, vol. 29, pp. 136–148, 2016.

[96] H. A. El-Sayed, A. Weiß, L. F. Olbrich, G. P. Putro, and H. A. Gasteiger, "OER Catalyst Stability Investigation Using RDE Technique: A Stability Measure or an Artifact?," *J. Electrochem. Soc.*, vol. 166, no. 8, pp. F458–F464, 2019.

[97] S. Cherevko, S. Geiger, O. Kasian, A. Mingers, and K. J. J. Mayrhofer, "Oxygen evolution activity and stability of iridium in acidic media. Part 1. - Metallic iridium," *J. Electroanal. Chem.*, vol. 773, pp. 69–78, 2016.

[98] S. Cherevko, S. Geiger, O. Kasian, A. Mingers, and K. J. J. Mayrhofer, "Oxygen evolution activity and stability of iridium in acidic media. Part 2. - Electrochemically grown hydrous iridium oxide," *J. Electroanal. Chem.*, vol. 774, pp. 102–110, 2016.

[99] P. Jovanovič *et al.*, "Electrochemical Dissolution of Iridium and Iridium Oxide Particles in Acidic Media: Transmission Electron Microscopy, Electrochemical Flow Cell Coupled to Inductively Coupled Plasma Mass Spectrometry, and X-ray Absorption Spectroscopy Study," *J. Am. Chem. Soc.*, vol. 139, no. 36, pp. 12837–12846, 2017.

[100] J. F. Moulder, W. F. Stickle, W. M. Sobol, and K. D. Bomben, *Handbook of X-ray Photoelectron Spectroscopy*. Physical Electronics Inc., 1992.

[101] P. Giannozzi *et al.*, "Advanced capabilities for materials modelling with Quantum ESPRESSO," *J. Phys. Condens. Matter*, vol. 29, no. 46, p. 465901, Oct. 2017.

[102] V. I. Anisimov, J. Zaanen, and O. K. Andersen, "Band theory and Mott insulators: Hubbard *U* instead of Stoner *I*," *Phys. Rev. B*, vol. 44, no. 3, p. 943, Jul. 1991.

[103] M. Cococcioni and S. De Gironcoli, "Linear response approach to the calculation of the effective interaction parameters in the LDA+U method," *Phys. Rev. B - Condens. Matter Mater. Phys.*, vol. 71, no. 3, p. 035105, Jan. 2005.

[104] J. P. Perdew, K. Burke, and M. Ernzerhof, "Generalized Gradient Approximation Made Simple," *Phys. Rev. Lett.*, vol. 77, no. 18, p. 3865, Oct. 1996.

[105] P. E. Blöchl, "Projector augmented-wave method," *Phys. Rev. B*, vol. 50, no. 24, p. 17953, Dec. 1994.

[106] A. Dal Corso, “Pseudopotentials periodic table: From H to Pu,” *Comput. Mater. Sci.*, vol. 95, pp. 337–350, Dec. 2014.
[107] A. Dal Corso, “No Title,” *Pslibrary (https://dalcorso.github.io/pslibrary/).* .
[108] “No Title,” *We used PAW potentials from pslibrary, in particular: H.pbe-kjpaw_psl.1.0.0.UPF, N.pbe-n-kjpaw_psl.1.0.0.UPF, O.pbe-n-kjpaw_psl.1.0.0.UPF, Ti.pbe-spn-kjpaw_psl.1.0.0.UPF, Ir.pbe-n-kjpaw_psl.1.0.0.UPF.* .
[109] I. Timrov, N. Marzari, and M. Cococcioni, “Hubbard parameters from density-functional perturbation theory,” *Phys. Rev. B*, vol. 98, no. 8, p. 085127, Aug. 2018.
[110] M. Methfessel and A. T. Paxton, “High-precision sampling for Brillouin-zone integration in metals,” *Phys. Rev. B*, vol. 40, no. 6, p. 3616, Aug. 1989.
[111] J. Schindelin *et al.*, “Fiji: an open-source platform for biological-image analysis,” *Nat. Methods 2012 97*, vol. 9, no. 7, pp. 676–682, Jun. 2012.
[112] N. W. M. Ritchie, J. Davis, and D. E. Newbury, “DTSA-II: A new tool for simulating and quantifying EDS spectra - Application to difficult overlaps,” *Microsc. Microanal.*, vol. 14, no. SUPPL. 2, pp. 1176–1177, Aug. 2008.
[113] Z. H. Ding, B. Yao, L. X. Qiu, and T. Q. Lv, “Raman scattering investigation of nanocrystalline δ-TiNx synthesized by solid-state reaction,” *J. Alloys Compd.*, vol. 421, no. 1–2, pp. 247–251, Sep. 2006.
[114] T. Ohsaka, F. Izumi, and Y. Fujiki, “Raman spectrum of anatase, TiO2,” *J. Raman Spectrosc.*, vol. 7, no. 6, pp. 321–324, Dec. 1978.
[115] L. Suhadolnik, M. Bele, and Ž. Marinko, “An apparatus for anodic oxidation of very small metal grids,” EP21163572.7, 2021.
[116] G. Koderman Podboršek *et al.*, “Atomically-resolved structural changes of ceramic supported nanoparticulate oxygen evolution reaction Ir catalyst,” *Electrochim. Acta*, p. 140800, Jul. 2022.
[117] S. Trasatti, *Electrocatalysis in the anodic evolution of oxygen and chlorine*, vol. 29, no. 11. Pergamon, 1984, pp. 1503–1512.
[118] L. A. Da Silva, V. A. Alves, M. A. P. Da Silva, S. Trasatti, and J. F. C. Boodts, “Oxygen evolution in acid solution on IrO2 + TiO2 ceramic films. A study by impedance, voltammetry and SEM,” *Electrochim. Acta*, vol. 42, no. 2, pp. 271–281, 1997.
[119] C. Wei, S. Sun, D. Mandler, X. Wang, S. Z. Qiao, and Z. J. Xu, “Approaches for measuring the surface areas of metal oxide electrocatalysts for determining their intrinsic electrocatalytic activity,” *Chem. Soc. Rev.*, vol. 48, no. 9, pp. 2518–2534, 2019.
[120] S. Watzele *et al.*, “Determination of Electroactive Surface Area of Ni-, Co-, Fe-, and Ir-Based Oxide Electrocatalysts,” *ACS Catal.*, vol. 9, no. 10, pp. 9222–9230, Oct. 2019.
[121] A. T. Marshall and R. G. Haverkamp, “Electrocatalytic activity of IrO2-RuO2 supported on Sb-doped SnO2 nanoparticles,” *Electrochim. Acta*, vol. 55, no. 6, pp. 1978–1984, 2010.
[122] H. S. Oh, H. N. Nong, T. Reier, M. Gliech, and P. Strasser, “Oxide-supported Ir nanodendrites with high activity and durability for the oxygen evolution reaction in acid PEM water electrolyzers,” *Chem. Sci.*, vol. 6, no. 6, pp. 3321–3328, Jun. 2015.
[123] G. Liu, J. Xu, Y. Wang, and X. Wang, “An oxygen evolution catalyst on an antimony doped tin oxide nanowire structured support for proton exchange membrane liquid water electrolysis,” *J. Mater. Chem. A*, vol. 3, no. 41, pp. 20791–20800, 2015.
[124] P. G. Pickup and V. I. Birss, “A model for anodic hydrous oxide growth at iridium,” *J. Electroanal. Chem.*, vol. 220, no. 1, pp. 83–100, 1987.
[125] D. Michell, D. A. J. Rand, and R. Woods, “Analysis of the anodic oxygen layer on iridium by X-ray emission, electron diffraction and electron microscopy,” *J. Electroanal. Chem. Interfacial Electrochem.*, vol. 84, no. 1, pp. 117–126, Nov. 1977.
[126] J. M. Otten and W. Visscher, “The anodic behaviour of iridium,” *J. Electroanal. Chem. Interfacial Electrochem.*, vol. 55, no. 1, pp. 13–21, Aug. 1974.
[127] D. A. J. Rand and R. Woods, “Cyclic voltammetric studies on iridium electrodes in

sulphuric acid solutions," *J. Electroanal. Chem. Interfacial Electrochem.*, vol. 55, no. 3, pp. 375–381, 1974.
[128] R. Kötz, "Anodic Iridium Oxide Films," *J. Electrochem. Soc.*, vol. 131, no. 1, p. 72, 1984.
[129] Y. R. Zheng *et al.*, "Monitoring oxygen production on mass-selected iridium–tantalum oxide electrocatalysts," *Nat. Energy*, 2021.
[130] A. Weiß, A. Siebel, M. Bernt, T.-H. Shen, V. Tileli, and H. A. Gasteiger, "Impact of Intermittent Operation on Lifetime and Performance of a PEM Water Electrolyzer," *J. Electrochem. Soc.*, vol. 166, no. 8, pp. F487–F497, 2019.
[131] S. Czioska *et al.*, "Increased Ir–Ir Interaction in Iridium Oxide during the Oxygen Evolution Reaction at High Potentials Probed by Operando Spectroscopy," *ACS Catal.*, vol. 11, no. 15, pp. 10043–10057, Aug. 2021.
[132] R. Woods, "Hydrogen adsorption on platinum, iridium and rhodium electrodes at reduced temperatures and the determination of real surface area," *J. Electroanal. Chem.*, vol. 49, no. 2, pp. 217–226, Jan. 1974.
[133] V. A. Saveleva *et al.*, "Insight into the Mechanisms of High Activity and Stability of Iridium Supported on Antimony-Doped Tin Oxide Aerogel for Anodes of Proton Exchange Membrane Water Electrolyzers," *ACS Catal.*, vol. 10, no. 4, pp. 2508–2516, Feb. 2020.
[134] T. Li *et al.*, "Atomic-scale insights into surface species of electrocatalysts in three dimensions," *Nat. Catal.*, vol. 1, no. 4, pp. 300–305, Apr. 2018.
[135] E. Özer, C. Spöri, T. Reier, and P. Strasser, "Iridium(1 1 1), Iridium(1 1 0), and Ruthenium(0 0 0 1) Single Crystals as Model Catalysts for the Oxygen Evolution Reaction: Insights into the Electrochemical Oxide Formation and Electrocatalytic Activity," *ChemCatChem*, vol. 9, no. 4, pp. 597–603, 2017.
[136] M. Scohy *et al.*, "Probing Surface Oxide Formation and Dissolution on/of Ir Single Crystals via X-ray Photoelectron Spectroscopy and Inductively Coupled Plasma Mass Spectrometry," *ACS Catal.*, vol. 9, no. 11, pp. 9859–9869, Nov. 2019.
[137] A. BalaKrishnan *et al.*, "Direct Detection of Surface Species Formed on Iridium Electrocatalysts during the Oxygen Evolution Reaction," *Angew. Chemie*, vol. 133, no. 39, pp. 21566–21573, Sep. 2021.
[138] A. L. Patterson, "The Scherrer Formula for X-Ray Particle Size Determination," *Phys. Rev.*, vol. 56, no. 10, p. 978, Nov. 1939.
[139] S. G. Seo *et al.*, "Preparation and visible-light photocatalysis of hollow rock-salt TiO1−xNx nanoparticles," *J. Mater. Chem. A*, vol. 1, no. 11, pp. 3639–3644, Feb. 2013.
[140] J. S. Im, S. J. Kim, P. H. Kang, and Y. S. Lee, "The improved electrical conductivity of carbon nanofibres by fluorinated MWCNTs," *J. Ind. Eng. Chem.*, vol. 15, no. 5, pp. 699–702, Sep. 2009.
[141] J. J. Ge *et al.*, "Assembly of well-aligned multiwalled carbon nanotubes in confined polyacrylonitrile environments: Electrospun composite nanofibre sheets," *J. Am. Chem. Soc.*, vol. 126, no. 48, pp. 15754–15761, Dec. 2004.
[142] C. S. Sharma, H. Katepalli, A. Sharma, and M. Madou, "Fabrication and electrical conductivity of suspended carbon nanofibre arrays," *Carbon N. Y.*, vol. 49, no. 5, pp. 1727–1732, Apr. 2011.
[143] H. Jiang, L. Yang, C. Li, C. Yan, P. S. Lee, and J. Ma, "High–rate electrochemical capacitors from highly graphitic carbon–tipped manganese oxide/mesoporous carbon/manganese oxide hybrid nanowires," *Energy Environ. Sci.*, vol. 4, no. 5, pp. 1813–1819, Apr. 2011.
[144] O. Almora, C. Aranda, E. Mas-Marzá, and G. Garcia-Belmonte, "On Mott-Schottky analysis interpretation of capacitance measurements in organometal perovskite solar cells," *Appl. Phys. Lett.*, vol. 109, no. 17, p. 173903, Oct. 2016.
[145] S. Ghosh, S. M. Jeong, and S. R. Polaki, "A review on metal nitrides/oxynitrides as an emerging supercapacitor electrode beyond oxide," *Korean J. Chem. Eng. 2018 357*, vol. 35, no. 7, pp. 1389–1408, Jun. 2018.

[146] J. Wen *et al.*, “TEM Study of Amorphous Carbon with Fully sp3-Bonded Structure,” *Microsc. Microanal*, vol. 23, no. 1, p. 2017, 2022.

[147] Y. Sun, C. Wang, L. Pan, X. Fu, P. Yin, and H. Zou, “Electrical conductivity of single polycrystalline-amorphous carbon nanocoils,” *Carbon N. Y.*, vol. 98, pp. 285–290, Mar. 2016.

[148] J. M. Chappé, N. Martin, J. Lintymer, F. Sthal, G. Terwagne, and J. Takadoum, “Titanium oxynitride thin films sputter deposited by the reactive gas pulsing process,” *Appl. Surf. Sci.*, vol. 253, no. 12, pp. 5312–5316, Apr. 2007.

[149] J. M. Chappé *et al.*, “Influence of substrate temperature on titanium oxynitride thin films prepared by reactive sputtering,” *Appl. Surf. Sci.*, vol. 225, no. 1–4, pp. 29–38, Mar. 2004.

[150] H. Wu, D. Lin, R. Zhang, and W. Pan, “) (a) Formalas, A. U.S. Patent 1,975,504, 1934. (b) Reneker, D. H.; Chun, I. Nanotechnology,” *J. Appl. Polym. Sci*, vol. 12, no. 10, p. 41, 2000.

[151] F. Fabreguette *et al.*, “Correlation Between the Electrical Properties and Morphology of Low-Pressure MOCVD Titanium Oxynitride Thin Films Grown at Various Temperatures,” *Chem. Vap. Depos.*, vol. 6, no. 3, pp. 109–114, 2000.

[152] D. A. G. Bruggeman, “Berechnung verschiedener physikalischer Konstanten von heterogenen Substanzen. I. Dielektrizitätskonstanten und Leitfähigkeiten der Mischkörper aus isotropen Substanzen,” *Ann. Phys.*, vol. 416, no. 7, pp. 636–664, 1935.

[153] B. Doiron *et al.*, “Plasmon-Enhanced Electron Harvesting in Robust Titanium Nitride Nanostructures,” *J. Phys. Chem. C*, vol. 123, no. 30, pp. 18521–18527, Aug. 2019.

[154] W. Spengler and R. Kaiser, “First and second order Raman scattering in transition metal compounds,” *Solid State Commun.*, vol. 18, no. 7, pp. 881–884, Jan. 1976.

[155] M. Bernard, A. Deneuville, O. Thomas, P. Gergaud, P. Sandstrom, and J. Birch, “Raman spectra of TiN/AlN superlattices,” *Thin Solid Films*, vol. 380, no. 1–2, pp. 252–255, Dec. 2000.

Bibliography

Journal Articles Related to the Thesis

G. Koderman Podboršek et al., “Iridium Stabilizes Ceramic Titanium Oxynitride Support for Oxygen Evolution Reaction”. Article to be published.

M. Bele et al., ““Nano Lab” Platform for State-of-the-art Nanoscale Understanding and Development of Electrocatalysts,”. Article to be published.

G. Koderman Podboršek et al., “Atomically-resolved structural changes of ceramic supported nanoparticulate oxygen evolution reaction Ir catalyst,” Electrochim. Acta, p. 140800, Jul. 2022.

G. Koderman Podboršek et al., “Microstructure and Electrical Conductivity of Electrospun Titanium Oxynitride Carbon Composite Nanofibres,” Nanomater. 2022, Vol. 12, Page 2177, vol. 12, no. 13, p. 2177, Jun. 2022.

Journal Articles Related to the Thesis Research Field

L. Moriau et al., “Effect of the Morphology of the High-Surface-Area Support on the Performance of the Oxygen-Evolution Reaction for Iridium Nanoparticles,” ACS Catal., vol. 11, no. 2, pp. 670–681, Jan. 2021.

L. Moriau et al., “Enhancing Iridium Nanoparticles’ Oxygen Evolution Reaction Activity and Stability by Adjusting the Coverage of Titanium Oxynitride Flakes on Reduced Graphene Oxide Nanoribbons’ Support,” Adv. Mater. Interfaces, vol. 8, no. 17, p. 2100900, Sep. 2021.

M. Bele et al., “Increasing the Oxygen-Evolution Reaction Performance of Nanotubular Titanium Oxynitride-Supported Ir Nanoparticles by a Strong Metal-Support Interaction,” ACS Catal., vol. 10, no. 22, pp. 13688–13700, Nov. 2020.

P. Jovanovič et al., “Methodology for Investigating Electrochemical Gas Evolution Reactions: Floating Electrode as a Means for Effective Gas Bubble Removal,” Anal. Chem., vol. 91, no. 16, pp. 10353–10356, Aug. 2019.

M. Bele et al., “Towards Stable and Conductive Titanium Oxynitride High-Surface-Area Support for Iridium Nanoparticles as Oxygen Evolution Reaction Electrocatalyst,” ChemCatChem, vol. 11, no. 20, pp. 5038–5044, Oct. 2019.

Other Journal Articles

D. Pavc et al., “Understanding self-assembly at molecular level enables controlled design of DNA G-wires of different properties,” Nat. Commun. 2022 131, vol. 13, no. 1, pp. 1–11, Feb. 2022.

Biography

2017 – 2022 (5 years)
Doctor of Science in Nanosciences and Nanotechnologies (ISCED 8)
Jožef Stefan International Postgraduate School, Jamova 39, 1000 Ljubljana, Slovenia
▪ Grade point average: 9.83/10.00
▪ Research work: At the National Institute of Chemistry, Hajdrihova 19, 1000 Ljubljana, Slovenia, Department of Materials Chemistry – D10, mentor: Prof. Goran Dražić, Ph. D.
▪ PhD thesis title: Electron microscopy of titanium oxynitride supported iridium based electrocatalysts

2014 – 2017 (3 years)
Master of Science in Chemistry (ISCED 7)
University of Ljubljana, Faculty of Chemistry and Chemical Technology (UL-FKKT), Večna pot 113, 1000 Ljubljana, Slovenia
▪ Grade point average: 9.50/10.00
▪ Research work: At the Chair of Inorganic Chemistry, mentor: Asst. Prof. Irena Kozjek Škofic, Ph. D.
▪ Master's thesis title: The effect of silicon or iron doping on the photocatalytic activity of titanium dioxide thin films

2010 – 2014 (4 years)
Bachelor of Science in Chemistry (ISCED 6)
University of Ljubljana, Faculty of Chemistry and Chemical Technology (UL-FKKT), Aškerčeva 5, 1000 Ljubljana, Slovenia
▪ Grade point average: 9.18/10.00
▪ Bachelor's thesis: For the Centre of Excellence for Low-Carbon Technologies (CO NOT) at the Chair of Inorganic Chemistry, mentor: Asst. Prof. Irena Kozjek Škofic, Ph. D.
▪ Bachelor's thesis title: Preparation of conductive platinum films